FORMATION OF STARS AND STELLAR CLUSTERS IN GALACTIC ENVIRONMENT
SIMULATIONS AND ANALYSIS OF STAR FORMING REGIONS IN GALACTIC SPIRAL ARM

Romas Smilgys

A Thesis Submitted for the Degree of PhD
at the
University of St Andrews

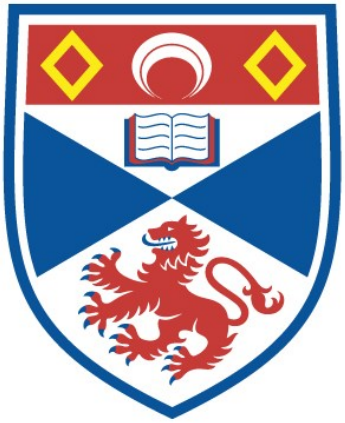

2018

Formation of stars and stellar clusters in Galactic environment

Simulations and analysis of star forming regions in Galactic spiral arm

by

Romas Smilgys

Submitted for the degree of Doctor of Philosophy in Astrophysics

19th March 2018

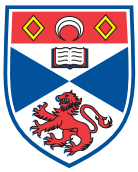

University
of
St Andrews

Declaration

I, Romas Smilgys, hereby certify that this thesis, which is approximately 50,000 words in length, has been written by me, that it is the record of work carried out by me and that it has not been submitted in any previous application for a higher degree.

Date Signature of candidate

I was admitted as a research student in September 2013 and as a candidate for the degree of PhD in September 2013; the higher study for which this is a record was carried out in the University of St Andrews between 2013 and 2017.

Date Signature of candidate

I hereby certify that the candidate has fulfilled the conditions of the Resolution and Regulations appropriate for the degree of PhD in the University of St Andrews and that the candidate is qualified to submit this thesis in application for that degree.

Date Signature of supervisor

Copyright Agreement

In submitting this thesis to the University of St Andrews we understand that we are giving permission for it to be made available for use in accordance with the regulations of the University Library for the time being in force, subject to any copyright vested in the work not being affected thereby. We also understand that the title and the abstract will be published, and that a copy of the work may be made and supplied to any bona fide library or research worker, that my thesis will be electronically accessible for personal or research use unless exempt by award of an embargo as requested below, and that the library has the right to migrate my thesis into new electronic forms as required to ensure continued access to the thesis. We have obtained any third-party copyright permissions that may be required in order to allow such access and migration, or have requested the appropriate embargo below.

The following is an agreed request by candidate and supervisor regarding the electronic publication of this thesis: Access to Printed copy and electronic publication of thesis through the University of St Andrews.

Date Signature of candidate

Date Signature of supervisor

Abstract

Star and stellar cluster formation in spiral galaxies is one of the biggest questions of astrophysics. In this thesis, I study how star formation, and the formation of stellar clusters, proceeds using SPH simulations. These simulations model a region of 400 pc and 10^7 solar masses. Star formation is modelled through the use of sink particles which represent small groups of stars. Star formation occurs in high density regions, created by galactic spiral arm passage. The spiral shock compresses the gas and generates high density regions. Once these regions attain sufficiently high density, self-gravity becomes dominant and drives collapse and star formation. The regions fragment hierarchically, forming local small groups of stars. These fall together to form clusters, which grow through subsequent mergers and large scale gas infall. As the individual star formation occurs over large distances before forming a stellar cluster, this process can result in significant age spreads of 1-2 Myrs. One protocluster is found to fail to merge due to the large scale tidal forces from the nearby regions, and instead expands forming a dispersed population of young stars such as an OB association.

Acknowledgements

I want to thank mostly my supervisor Prof. Ian Bonnell for all these years of useful discussions and enthusiasm. I also acknowledge DiRAC computing facilities for available computing time. I would like to thank our star formation group members Ian Bonnell, Diego Falceta Goncalves, William Lucas, Felippe Gerardo Ramon Fox, Kristin Lund and Claudia Cyganowski for organising useful star formation group meetings and discussions. I thank Rowan Smith for useful discussion about clusters. I thank my yearly examiners Dr. Claudia Cyganowski, Dr. Kenny Wood and Prof. Keith Horne for interesting questions and directions of my research. I also would like to acknowledge my final examiners Dr. Claudia Cyganowski and Prof. Simon Goodwin for useful suggestions in correcting this thesis. I received particular assistance in the writing of this work in respect of matters of grammar, style, vocabulary, spelling or punctuation. The assistance was provided by Isaac Nowell. I want to acknowledge the ERC grant from which my PhD was funded as well as the opportunity to participate in various star formation conferences around the world.

Contents

List of Figures

List of Tables

1 Introduction

1.1 Milky Way

The Milky Way - the bright river in the dark sky. It has attracted much wonder since ancient times. "What is it?" was the key question until the invention of the first telescopes. Over time it became clear that this river is the combined diffuse illumination formed by billions of stars. Only when we found many other galaxies did it become clear that the Milky Way is our own spiral galaxy, which we observe from within. Our unique view from inside the Galaxy brings about many fundamental challenges for galactic astronomy which we are unable to resolve even today. The 3-dimensional map, Galaxy dynamics, star formation in high density clouds, spiral arms, stellar clusters and many more things besides remain secrets to today's astronomy. Due to the difficulty of mapping the Milky Way disc, astronomers also obtain knowledge from observations of other spiral galaxies which are in a face-on view. Further development of telescopes and instrumentation have progressed observations while increasing computing power has allowed us to run numerical simulations. While observations bring direct

measurements, simulations bring a deeper understanding of the physical processes which can't be seen by observations. Both contribute to our knowledge and understanding of galactic processes, and are essential to progressing Milky Way astronomy.

The Milky Way is a spiral galaxy, which contains a stellar disc (with spiral arms), the bulge and the halo (i.e. Binney & Tremaine 2008). Each of these components has its own stellar populations. The bulge and halo contain old stars, while the disc, in addition to old stars, contains many young objects. This includes young stars, molecular clouds and open clusters.

1.2 Galactic disc and its stellar populations

The Milky Way disc is the place where star formation processes are actively ongoing today. While the mass of the disc is dominated by old stars, young stars, stellar clusters, and OB associations are also present. The Sun also belongs to the Milky Way disc. Interstellar gas and dust are also present in the disc. The entire disc of the Milky Way is rotating and the rotation curve (the radial profile of the rotational velocity) has been measured several times (Clemens 1985; Brand & Blitz 1993; Russeil et al. 2017). The rotation curve is not Keplerian or that of a solid body. The best solution is that the rotation curve is driven by the presence of a dark matter halo (Sofue et al. 2009; Sofue 2012).

1.3 Spiral arms and shock

Stars and gas in the Milky Way disc are not distributed uniformly. There are spiral arms present in the disc. Spiral arms appear as overdensities of stars and gas. As we see the Milky Way from inside the disc, it is difficult to see the spiral arm pattern. Because of this, astronomers targeted other spiral galaxies which, when face on, display a visible spiral arm structure. However, the Milky Way's spiral arm structure began to be mapped from 21 cm HI observations (Simonson 1976). Most recent observations include YSOs (young stellar objects) for mapping spiral arms (Urquhart et al. 2014). Currently, it is thought that the Milky Way has two major spiral arms (the Scutum-Centaurus and Perseus arms) and at least two secondary arms (the Sagittarius and Norma arms) (Churchwell et al. 2009; Dame 2013, see Figure 1.1). The Norma arm in the first and second Galactic quadrants is known as the Outer arm. Dame & Thaddeus (2011) used CO mapping and found the continuation of Scutum-Centaurus arm beyond the Outer arm in the first quadrant. The lower density regions between spiral arms are usually called

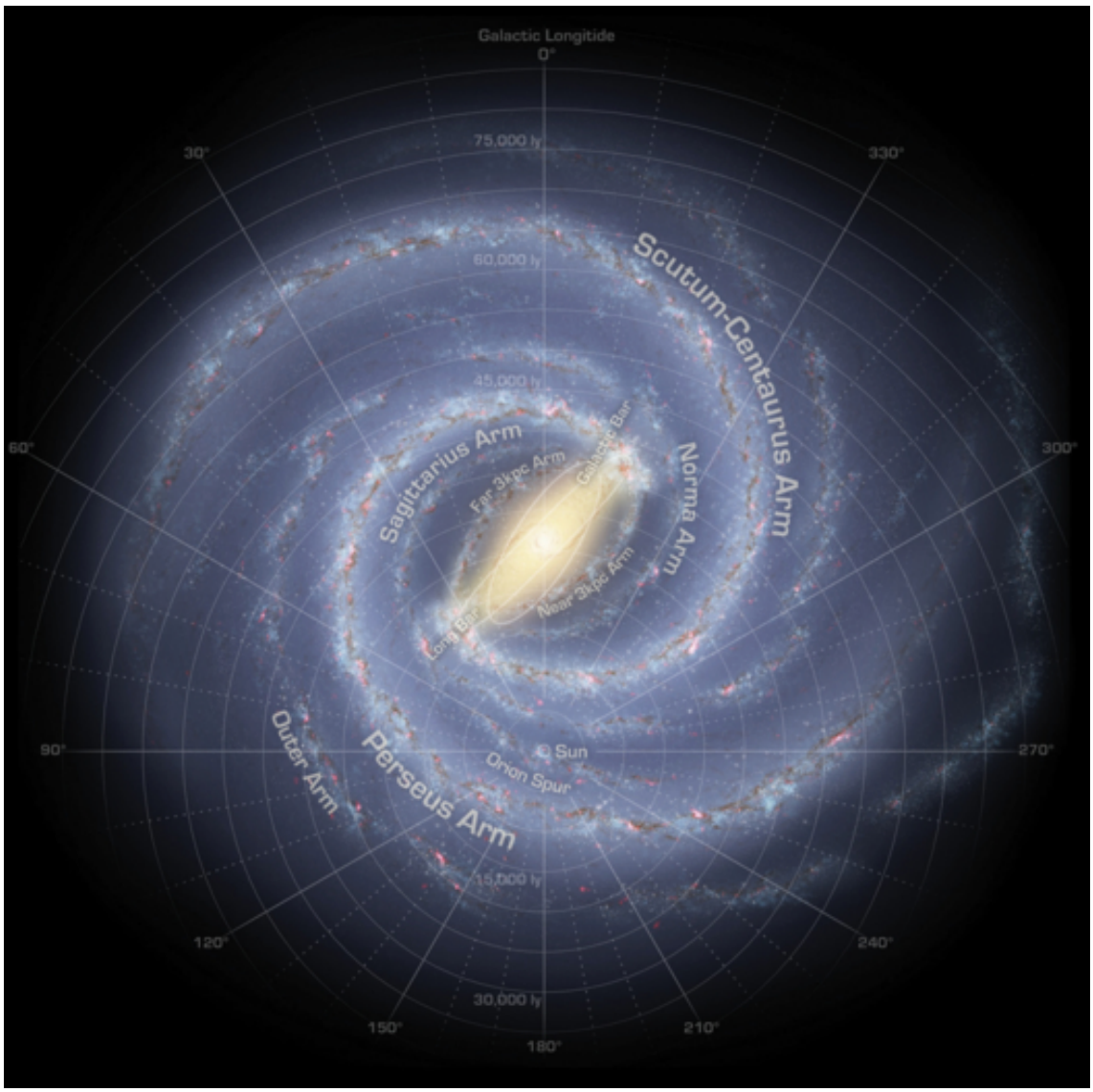

Figure 1.1: A sketch showing the view of the currently known spiral arm structure of the Milky Way, taken from Churchwell et al. (2009). Mapping the Milky Way spiral arms is a difficult task, as the Sun is inside the Galactic plane and the lines of sight through the spiral arms overlay one another. As such these maps can only be drawn by finding the distribution of gas such as HI, and star forming regions (clusters and OB associations), as young massive stars contribute significantly to the total brightness of the spiral arms.

inter-arm regions.

The interstellar medium (ISM) gas contributes by 13 % mass fraction to the total mass of gas and stars in the disc (Kalberla & Kerp 2009). The ISM gas also tends to be higher density in spiral arms - gas assembles into molecular clouds here (i.e. Dobbs et al. 2006; Bonnell et al. 2013). The Milky Way disc rotates at 200 - 240 km/s (Clemens 1985; Majewski 2008; Reid et al. 2014) at the Sun's distance. The spiral arm pattern rotates slower than the disc in the inner part of the galaxy, and faster in the outer part of the galaxy. The corotation radius is defined as the distance from the centre where the spiral pattern and disc rotational velocity are the same. Azimuthal velocity gradients of up to several 10 km/s can arise due to different rotation velocities between the spiral pattern and the disc (Tilanus & Allen 1990; Shetty et al. 2007; Bonnell et al. 2013). In gas, these velocity gradients can be sharp and create a shock, which is usually called a spiral shock. This spiral shock compresses low density HI gas into higher density regions, which start to cool and form molecular H_2. These regions become molecular clouds (Bonnell et al. 2013).

Density wave theory in spiral arms (Lin & Shu 1964) is commonly invoked in order to explain the spiral pattern. There are multiple observations of streaming motions mostly from HI in other galaxies (Tilanus & Allen 1990; Shetty et al. 2007), which could explain deviations from the rotation curve as the presence of spiral density waves. There are also some indications of streaming motions in the Milky Way's spiral arms (Sitnik 2003; Fresneau et al. 2005).

Recent smoothed particle hydrodynamic (SPH) simulations of galaxies (Dobbs et al. 2006, 2012; Dobbs & Pringle 2013; Bonnell et al. 2013; Dobbs & Baba 2014) have included a spiral potential in order to investigate the evolution of the ISM on Galactic scales, spiral shocks, and the creation of molecular clouds. The spiral potential in these simulations has a time independent shape and rotates in the galactic disc with the same angular velocity at all galactocentric radii. Inside the corotation radius material rotates faster than the spiral pattern and enters the spiral arm from the opposite direction to the disc rotation. Gas coming from the inter-arm region shocks with higher density gas in spiral arms due to a velocity difference of 20 - 40 km/s. This creates a layer of high density material which forms molecular clouds.

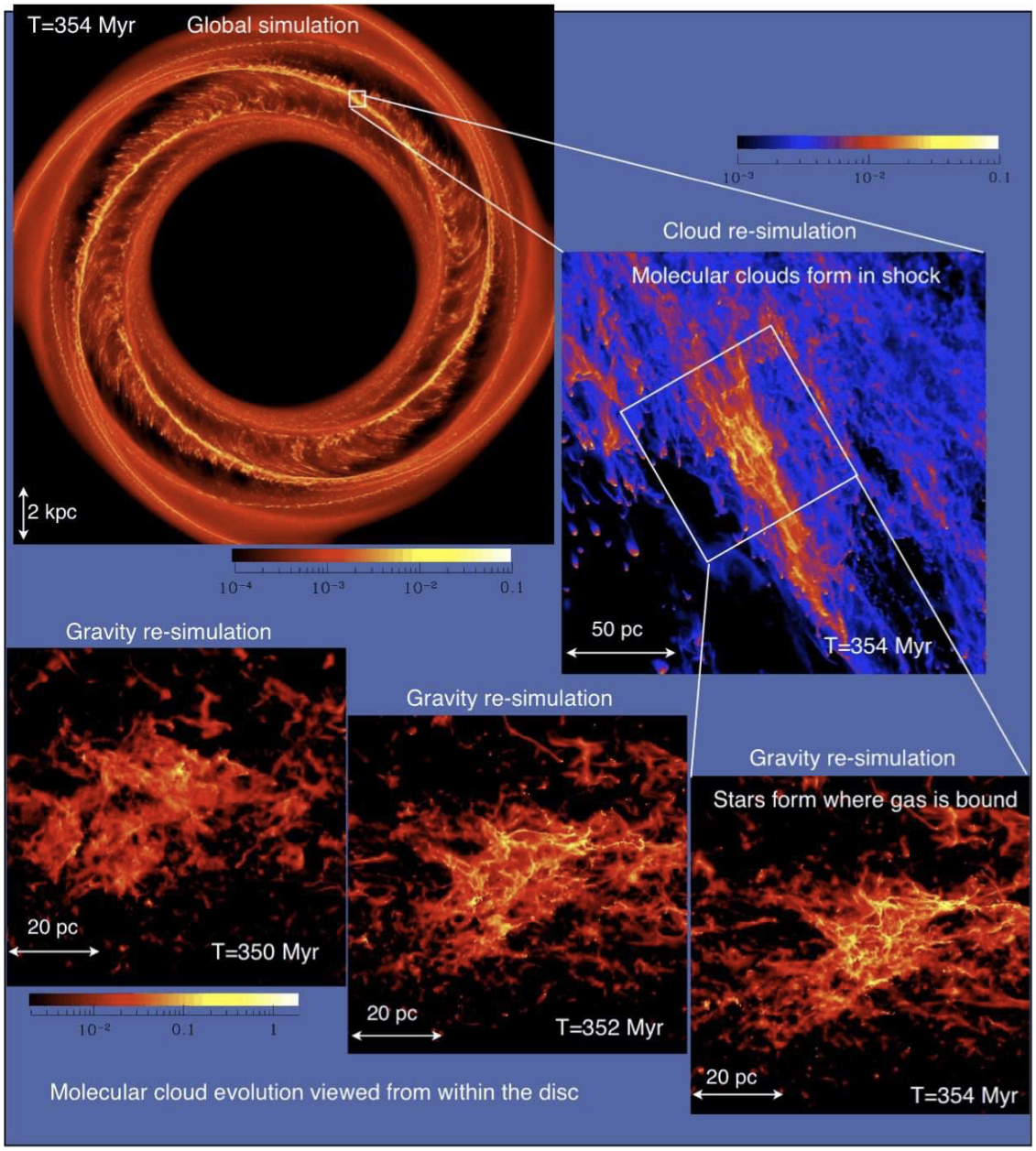

Figure 1.2: This image has been taken from Bonnell et al. (2013) and shows a set of nested simulations allowing consistent and successive levels of resolution from large galactic to small cluster scales. The large scale simulations were able to resolve the dynamics and structure of galactic spiral arms. Then a small subset of one part of a spiral arm was taken and each particle subdivided into smaller ones. This technique allows initial conditions to be inherited from the larger scale simulation, rather than generating idealised initial conditions. The subdivision may be performed on several levels, i.e. the first level may be over a segment of a spiral arm, and the second for a small portion of that segment, resolving the molecular cloud and cluster scales and allowing the inclusion of self-gravity. The small scale simulations in this case have both the large scale shock and the self-gravity of the collapsing regions.

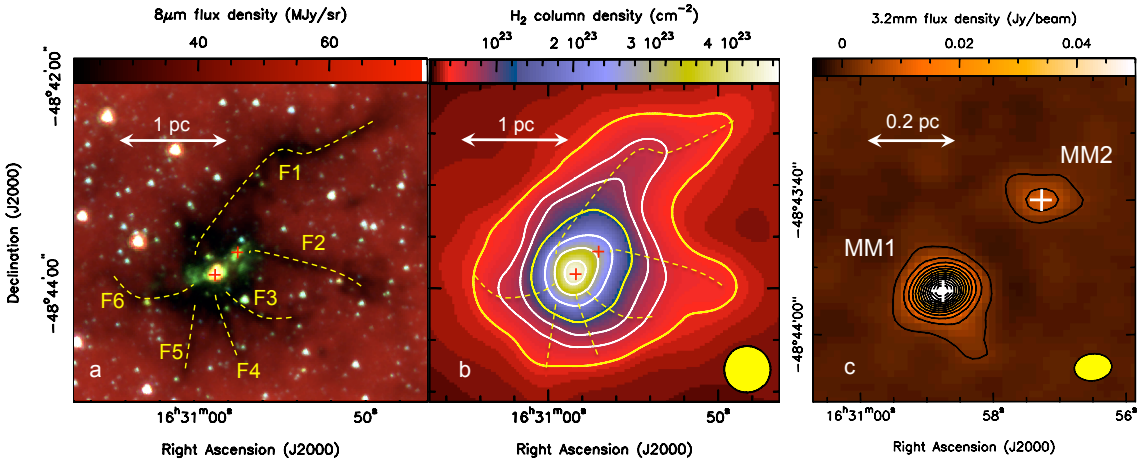

Figure 1.3: This image from Peretto et al. (2013) shows resolved filamentary structure feeding a cluster forming clump. Regions like this are usually embedded in the highest density regions of molecular clouds, making observations difficult. The early stages of star and cluster formation are as a result still poorly understood. These images were obtained by using observations from Spitzer and ALMA.

1.4 Molecular clouds

Molecular clouds are one of the most central topics in astrophysics and especially star formation. During the molecular cloud phase of the ISM, regions come about in which star formation occurs and gravity overcomes turbulent motions to start forming clumps, cores and protostars (Williams et al. 2000). However, the molecular cloud phase is still not well understood, as there are multiple physical processes in action which lead to completely different scenarios depending on which processes are most dominant (i.e. Stahler & Palla 2005).

Our understanding of star formation is based on the idea that stars form from gravitationally collapsing clouds (i.e. Stahler & Palla 2005). However, it is challenging to observe this process and reproduce it in simulations. Firstly, molecular clouds have irregular shapes and non-uniform density. This produces higher density regions which collapse more quickly than lower density regions. As a result, the cloud develops a hierarchical density structure (i.e. left-panel in Figure 1.3). The densest parts of the cloud form clumps ($\sim$ 1 pc sizes; middle-panel in Figure 1.3) which are precursors of young stellar clusters (Williams et al. 2000). Structures on even smaller scales are pre-stellar cores ($\sim$ 0.1 - 0.2 pc sizes; right-panel in Figure 1.3), which form individual protostars (Williams et al. 2000). The whole hierarchical structure of the cloud depends on the equilibrium of forces and gravitational binding. Certain regions are bound to collapse. The collapse occurs on smaller scales (clumps and cores), while the whole cloud can be unbound and not collapsing.

Cloud chemistry is one of the most important channels providing information about cloud structure. Different molecular tracers can be used to map regions of different densities. For example, Rathborne et al. (2015) obtain the mass distribution and virial ratio radial profile for G0.253+0.016 (known as the Brick) by using multiple molecules tracers. The radial profile shows that the virial ratio is below 1 on around the 2 pc scale. The most abundant molecule in molecular clouds is H_2, although it has no strong emission lines and can't be traced easily. The next most abundant molecule, which is more easily traced, is CO. As H_2 is much more abundant than CO it is essential to measure the mass of H_2 in order to estimate cloud masses. There have been many attempts to evaluate CO to H_2 conversion factors (Maloney & Black 1988; Narayanan et al. 2012; Bolatto et al. 2013). Some simulations suggest that this conversion factor could be dependent on the particular region's evolutionary stage (Clark et al. 2012b). In the highest density regions dust continuum emission is used to observe the region at the core scales (Peretto et al. 2013; Figure1.3 right-panel).

In order to correctly run SPH simulations of molecular clouds, it is necessary to take into account the cooling function which depends on the chemistry of the cloud. The cooling function describes radiative energy losses from the gas. One of the commonly used cooling functions in SPH simulations was developed by Koyama & Inutsuka (2000, 2002) and later corrected by Vázquez-Semadeni et al. (2007). However, this cooling function is an approximation of the most important coolants at lower densities including Lyman-alpha, CII and OI. This function also assumes that gas is optically thin, while at high densities (>10 cm^{-3}), gas is replaced by sink particles (i.e. Bonnell et al. 2013 simulations). More recently, development of the cooling function has taken non-equilibrium chemistry into account (Glover & Mac Low 2007a,b). The use of this function has shown that cloud masses and the properties of gas do not show many differences when choosing a cooling function but the cloud morphology and large-scale velocity distribution appear to be affected (Micic et al. 2013).

Magnetic fields are another key factor which affect cloud collapse and evolution. The only direct method of measuring the magnetic field in the ISM is the Zeeman effect (Crutcher et al. 2010; Li et al. 2015). However, the Zeeman effect only gives measurements for the strength of magnetic fields along the line of sight. Dust polarisation is used in order to estimate the magnetic field direction in the plane of the sky (Hiltner 1949; Heiles et al. 1993; Crutcher 2012). Observations from Planck and BLASTPol (Pascale et al. 2012; Planck Collaboration et al. 2011; Soler et al. 2016) were used to obtain detailed maps of polarisation in the Milky

Way's ISM on larger scales. Simulations are used to produce magnetic fields in 3D. Some simulations, such as Soler et al. (2013) and Soler & Hennebelle (2017) directly target dust polarised emission. Others are designed to examine physical parameters and the evolution of the ISM across multiple scales - from Galactic to molecular cloud, to protostars (Price et al. 2009; Bate et al. 2017; Lewis & Bate 2017). The main effect of the magnetic field is that clouds could be in a state of magnetic freezing, slowing down their collapse (Elmegreen 1979; Shu et al. 1987; Kamaya & Nishi 2000). This occurs if ions are present in the cloud as well as neutral atoms. These ions are dragged by magnetic field lines. As neutral atoms collide with the ions, they too are dragged. If this magnetic drag opposed the velocity of the flow (i.e. the collapse of a self-gravitating cloud), then the flow may be slowed. In the case of a spherical clump, collapse creates a velocity field directed towards the clump centre while the magnetic field opposes this. As a result, the collapse time can become several times longer than the free fall time of the clump due to the effect of the magnetic field. Due to this process star formation can be delayed and the SFE appears to be smaller.

Molecular clouds form when the material is compressed by the spiral shock (Dobbs et al. 2006, 2008). This leads to atomic hydrogen, HI, converting to its molecular form H_2 while the region cools. Together these regions form the non-uniform ISM consisting of higher and lower density zones, filaments, voids and clumps. Higher density regions containing a significant fraction of gas in molecular form are usually called molecular clouds. Although Dobbs et al. (2008) simulations show that molecular gas fraction is several 10% at densities > 10 cm^{-3}, the molecular cloud definition is not restricted and remains an open question. Compressed clouds move through the spiral arm until they reach the other side, where the material comes out from the spiral arm. Here, molecular clouds dissolve, material heats up from the galactic radiation and expands, and H_2 molecules start to break up again to form atomic HI (Dobbs et al. 2008). The lifetime of molecular clouds can be defined as the time taken for the material to move from one side of a spiral arm to the other. The values of molecular cloud lifetimes are still under great debate, but they likely range from several to several tens of Myrs (Blitz & Shu 1980; Dobbs & Pringle 2013). Clouds can also experience disruption by feedback from massive stars (if formed), which can reduce cloud lifetimes to several Myr (Zasov & Kasparova 2014).

Molecular clouds can have a filamentary structure. Herschel observations found high density filaments with a characteristic width of 0.1 pc (André et al. 2010, 2014). Cloud forma-

tion simulations with self-gravity naturally form filamentary structures (Gómez & Vázquez-Semadeni 2014; Smith et al. 2014; Federrath 2016). Simulations have also shown that turbulence and magnetic fields influence the filaments (Kirk et al. 2015). It is currently thought that filaments play an important role in cloud collapse, as material on large scales firstly collapses into the filaments, which themselves feed protocluster forming clumps in intersection points (Vázquez-Semadeni et al. 2017). This is in good agreement with observations, showing the flow along filaments towards the clump (Peretto et al. 2013).

Another major physical process in the ISM is turbulence. Turbulence is defined as the internal motions inside molecular clouds (Falceta-Gonçalves et al. 2015). The Larson scaling relation (Larson 1981) shows that the line of sight velocity dispersion, found by observing spectral linewidths, scales with the size of molecular clouds according to $\sigma = l^{\alpha}$. Here α is usually around 0.5, but may also vary with surface density within a cloud (Heyer et al. 2009). Turbulence in high density collapsing cores can be regulated by gravity (Yoshida et al. 2010). Supernovae can inject turbulence into surrounding regions (Gressel et al. 2008; Hill et al. 2012), but their effects may be limited to only local gas (Heitsch et al. 2006). A more universal mechanism of the turbulence generation in spiral galaxies could be gas interaction with spiral arm potential (Falceta-Gonçalves et al. 2015). Simulations with spiral shocks (Bonnell et al. 2006; Dobbs et al. 2008; Bonnell et al. 2013) provide local instabilities which can create turbulent perturbations at galactic scales throughout the entire disc.

1.5 Stellar clusters

Stellar clusters are compact objects, containing large numbers of stars in a small region of space, higher in concentration than the stellar background (i.e. Murdin 2001). The two most common types of stellar clusters are well known from optical observations - these are globular and open clusters. Murdin (2001) gives appearent sizes of open clusters to be 4 pc while for globular clusters instead of appearent size Murdin (2001) gives core radii between 1 and 10 pc. According to Murdin (2001), open cluster masses range between 10 and 10^4 $M_{\odot}$, while globular clusters are much more massive, i.e. 10^4 - 10^6 $M_{\odot}$. Globular clusters are distributed in the whole halo of the Milky Way, while open clusters are in the disc. Globular clusters in the Milky Way are also old objects, with ages of 8-16 Gyr (Murdin 2001), while ages of open clusters ranges between 5 Myr and 9 Gyr (Murdin 2001). The youngest clusters are sometimes referred to as embedded clusters as they are visible in IR surveys and not in optical

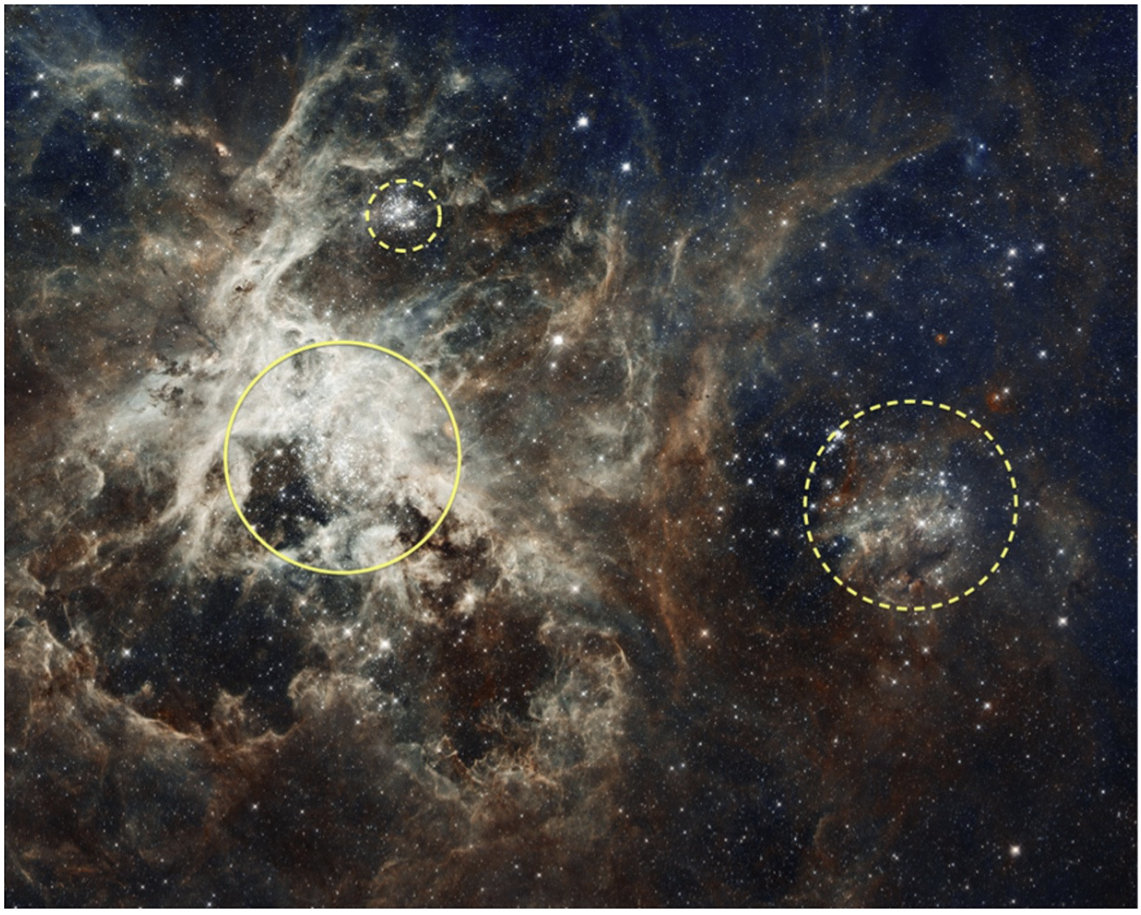

Figure 1.4: The HST image of Tarantula star forming region taken from Cignoni et al. (2015). 30 Doradus, here shown contained by the solid circle, is known as one of the most intensively star forming regions known in the nearby Universe. The image shows the complex structure of the region with imprints of various physical processes, such as gravity, magnetic fields, feedback, etc. The interaction of these effects is complex and makes it difficult to tell which is dominating star formation. For this reason it is necessary to develop numerical simulations which allow us to separate physical processes and investigate star formation dynamically.

wavelengths. Typical sizes of embedded clusters are 1 pc, masses 100 - 1000 $M_\odot$ and ages 1-5 Myr (Murdin 2001). These young clusters are found in active star forming regions and are still undergoing star formation processes (Greene & Meyer 1995; Palla & Stahler 1999; Gutermuth et al. 2009; Saral et al. 2015). While Murdin (2001) suggests a cluster definition based on the visual overdensity, it is important to determine the state of cluster gravitational boundedness where possible.

Most of the stars and probably all massive stars (> 10 $M_\odot$) form in clusters or OB associations (Lada & Lada 2003). Most of the young compact clusters later disperse (especially low mass, Moeckel et al. 2012) and enrich the galaxy's background population with their stars. Moreover, when clusters are defined as bound systems (i.e. Gieles & Portegies Zwart 2011), only around 10 % of star formation would be happening in such clusters while the majority of star formation would occur in associations (Bastian 2013). However, earliest phases of bound clusters and associations are the most difficult to distinguish. As a result, understanding cluster formation is a key step in the star formation process.

It is thought that clusters form from clumps - high density regions in molecular clouds. As the bound region in the turbulent cloud collapses, it fragments hierarchically into clumps that form small clusters, which later merge to form higher mass clusters (Bonnell et al. 2003; Bate et al. 2003; Krumholz & Bonnell 2007; Offner et al. 2008; Smith et al. 2009). Observations of star forming regions in molecular clouds such as Peretto et al. (2013) show the fragmentation in terms of filamentary structure (André et al. 2010, 2014; Hacar et al. 2017), transferring gas towards the cluster forming clump. The concept that clusters grow hierarchically is also supported by observations, such as that by Rathborne et al. (2015), who suggests that G0.253+0.016 is about to form a cluster from hierarchical and filamentary structures present in the turbulent medium.

A large number of optical and near-IR observations are made in order to understand the process of stellar cluster formation. These observations have allowed measurements to be made of the mass-radius relation (Pfalzner et al. 2016), stellar age spreads (Getman et al. 2014; Kuhn et al. 2015a), line of sight velocities (Fűrész et al. 2008; Hacar et al. 2016), distribution of positions (Kraus & Hillenbrand 2008; Gutermuth et al. 2009) and spatial structure (Kuhn et al. 2014, 2015a,b). The mass-radius relation shows that more massive clusters are also larger in size. Stellar age spreads give an indication of the period of time over which

star formation has taken place. The line of sight velocities allow us to measure the velocity dispersion for the whole cluster. The velocity dispersion is related to the total cluster mass - the more massive the cluster, the larger the velocity of the star in the cluster centre where most mechanical energy is in the form of kinetic energy. The set of these observables allows us to describe the current state of the cluster.

Observations have the challenges of producing 3D maps of clusters, and following their evolution through time, both of which are crucial steps in the understanding of cluster formation. This is where hydrodynamical simulations can help. Recent simulations have addressed in detail fragmentation, collapse, turbulence and accretion in star forming regions (Bate et al. 2003; Bonnell et al. 2003, 2011; Krumholz et al. 2011; Bertelli Motta et al. 2016). As the cloud collapses, due to internal turbulence it fragments into chunks and filaments, creating higher and lower density regions in the cloud. The highest density regions form cores and in turn eventually form protostars. Forming protostars can be represented by sink particles in simulations. Sinks may continue to accrete gas from their surroundings. This leads to mass growth through accretion until the reservoir is depleted or stellar feedback clears the environment. An important factor here is the cloud's gravitational boundedness which leads to bound clouds producing more efficient clustered star formation, while unbound clouds possess inefficiently distributed star formation (Bonnell et al. 2011). However, this does not tell how close simulated clouds are to real clouds in spiral arms and thus initial cloud boundedness remains an open problem in simulations. For this reason, it is essential to use initial conditions inherited from more realistic models run on a galactic scale, rather than generated from simplified geometry (such as uniformly distributed particles in a sphere, cube or cylinder).

When massive stars are formed in a cluster, they produce strong stellar winds and ionising radiation (Dale et al. 2005, 2007; Dale & Bonnell 2008), and when they finally blow up as supernovae (SN) they create expanding shells of SN ejecta. These processes are called stellar and SN feedback. Stellar winds can inject momentum into surrounding gas, directed radially outward and thus oppose the gravitational infall of new material (Dale & Bonnell 2008). This can, in turn, reduce accretion onto the star. SN feedback is much stronger and can potentially exert its influence over kiloparsec scales (Girichidis et al. 2016; Gatto et al. 2017). As a result star formation is likely to be affected by feedback from stars which have already formed. It is thought that lower star formation efficiencies in real molecular clouds compared to simulated ones can be explained by this feedback (Megeath et al. 2016; Dubois & Teyssier 2008; Ostriker

& Shetty 2011; Girichidis et al. 2016; Gatto et al. 2017). In hydrodynamical simulations implementing feedback, star formation efficiencies are reduced by around two times (Dale & Bonnell 2012; Dale et al. 2014, 2015; MacLachlan et al. 2015; Dale 2017).

1.6 OB associations

OB associations are known to be large loose clusters containing OB stars. The first associations were found by Ambartsumian (1949, 1955). Several dozen OB associations are known to exist in the Milky Way around the Sun (Mel'Nik & Efremov 1995). The diameters of OB associations are usually between several tens of parsecs and sometimes above 100 pc (Murdin 2001). Murdin (2001) compares OB associations with globular, open and embedded clusters, with OB association masses in the range of 10^3 - 10^4 $M_\odot$, and ages between 5 and 20 Myr. Individual stars also show similar kinematics (i.e. most members moves in the same direction). OB associations are also observed in other spiral galaxies (Magnier et al. 1993; Bresolin 1996; Pietrzyński et al. 2001, 2005), and may be related to major OB star groupings in spiral arms (Mel'Nik & Efremov 1995).

When Lada & Lada (2003) defined clusters based on the visual stellar density, the boundedness of these clusters was not considered. Later, Gieles & Portegies Zwart (2011) revised that real clusters are bound systems and can survive for multiple crossing times. Gieles & Portegies Zwart (2011) noted that the main feature of bound clusters would be that their age ratio with the crossing time is above 1. According to Gieles & Portegies Zwart (2011), unbound associations would have large crossing times and thus their age ratio with the crossing time would remain below 1. Based on this definition Bastian (2013) finds that most of stars are forming not in bound clusters but in unbound associations. However, at the earliest stages of cluster formation the cluster age is not well defined. Ongoing star formation and merging processes can also change cluster age and its crossing time. As a result, differences between clusters and associations at their early ages remains unclear.

The origin and formation mechanism of OB associations is not well known. Oort (1955) proposed that OB associations can form from expanding unbound clouds, with expansion amplified by radiation from stars and feedback. Elmegreen & Lada (1977) suggested that star formation in unbound clouds could have been triggered by nearby feedback from neighbouring groups of stars, with star formation beginning from the edge of the cloud (sequential

star formation). Clark et al. (2005) proposed that OB associations form in globally unbound clouds, where only locally bound subclusters form, which are unbound to each other. Studies of backwards integration of the nearest Sco-Cen association members have shown that large scale star formation could have been triggered by the shock of the Inner spiral arm (Fernández et al. 2008). As all these theories are still being debated, it remains unclear which theory (or a combination of theories) is the most likely to explain the formation of OB associations.

1.7 Thesis outline

In this thesis I use smoothed particle hydrodynamics (SPH) simulations to investigate key star formation problems. Most of it is centred on the formation of stellar clusters.

- In chapter 2 I review how SPH simulations work in general and in terms of applications in star formation. I discuss fluid equations and derivation of SPH equations. Mass, momentum and energy conservation equations are discussed in detail. I overview how smoothed quantities are calculated, which explains how SPH works. Finally I review sink particle formation and accretion.

- In chapter 3 I review the initial conditions of Bonnell et al. (2013) simulations, which were used in further chapters. I review the Global simulation, which was used to simulate the Milky Way type's galaxy disc with spiral arm structure. I also review galactic potential generation method, designed by Dobbs et al. (2006). Then I discuss the Cloud and Gravity simulations, which were used to investigate molecular cloud and star formation respectively. I finish the chapter by reviewing the cooling function, which was used in Bonnell et al. (2013) simulations in order to have two-phase ISM.

- In chapter 4 I discuss my new cluster finding algorithm which allows us to find clusters of sinks in SPH simulations. I also discuss free parameters such as gravitational potential thresholds, and their effects on how clusters are found at a given time. Cluster tracing over time is also discussed in this chapter.

- In chapter 5 I discuss the main properties of star formation in the Bonnell et al. (2013) simulations. I show maps of initial conditions, review the radial profiles of accreted particles at sink formation event, and address star formation efficiencies over different density scales.

- Chapter 6 includes the central discussion of cluster formation. This includes tracing

cluster members over time, determining cluster merging and formation histories, mass-radius relation, angular momentum, cluster mass growth, stellar age spreads, main star formation region age gradients, cluster sphericities, central condensation in terms of enclosed mass slopes, and half-mass radii.

- In chapter 7 I review one particular object, which is likely to be a failed cluster or even an OB association. I review the unusual expansion phase of the object during the last few Myr in terms of half-mass radii, densities, energies and tidal forces. I review the possibility of the object expansion phase caused by tidal effects.

- Finally in chapter 8 I conclude the work of my thesis and discuss future steps and directions.

2

Smoothed particle hydrodynamics

In this chapter, I will review the background and basis of smoothed particle hydrodynamics (SPH) simulations and analyse its application to star formation. SPH particles are used as Lagrangian fluid elements which can be used to represent gas in the interstellar medium. The principles of SPH, such as using a kernel to smooth particles through a volume, were laid down by Gingold & Monaghan (1977); Lucy (1977). Soon after that, different groups of astronomers started to use the idea and adopt the formalism to their own codes. Most of the currently used code for SPH was written by Benz (1990); Benz et al. (1990). sphNG, the code used in the work presented in this thesis, was based on the code of Benz but began to reach its modern form with the introduction of sink particles by Bate et al. (1995). Early codes were designed with very basic physics, but have since been updated to account for radiative transfer (Forgan et al. 2009; Clark et al. 2012a), magnetic fields (Price 2004; Price & Monaghan 2004a,b), better heating and cooling (Koyama & Inutsuka 2000, 2002; Vázquez-Semadeni et al. 2007) and stellar feedback (Dale & Bonnell 2012; Dale et al. 2015). When a simulation is run, the gas distribution in future timesteps depends on the initial conditions, i.e. the particle positions,

velocities and densities. Early SPH simulations of star and cluster formation used idealised initial conditions where particles were distributed in a sphere, cube or cylinder (Bate 2012). However, this has been addressed by firstly running a lower resolution larger scale simulation and then re-resolving and simulating a smaller portion of interest. This allows us to investigate cluster formation while taking into account the influence of the Galactic environment (Bonnell et al. 2013).

2.1 Fluid equations

In order to derive SPH equations, it is essential to briefly discuss fundamental fluid equations. Fluid equations allows us to define how the fluid evolves over the time. There are two definitions of such evolution: Eulerian and Lagrangian. The Eulerian definition is based on fixed positions in space. Grids are usually used in such a way that the entire grid is fixed in space and each grid cell represents the properties of the fluid at a given location. The Lagrangian definition is based on moving elements together with the fluid. These fluid elements are represented by particles in SPH simulations. So SPH has a Lagrangian nature. A generic relation can be defined between Eulerian and Lagrangian quantities:

$$\frac{dQ}{dt} = \frac{\partial Q}{\partial t} + \mathbf{u} \cdot \nabla Q; \tag{2.1}$$

where Q is a generic quantity and t is the time. There are three fundamental equations which defines how fluid evolves: mass conservation (continuity), momentum conservation and energy conservation. The continuity equation in Eulerian (left) and Lagrangian (right) forms is:

$$\frac{\partial \rho}{\partial t} + \nabla(\rho \mathbf{v}) = 0; \qquad \frac{d\rho}{dt} + \rho \nabla \cdot \mathbf{v} = 0. \tag{2.2}$$

Here ρ is the mass density and $\mathbf{v}$ is velocity vector at a given position (Eulerian) or fluid element (Lagrangian). The momentum conservation is defined as:

$$\frac{\partial \mathbf{v}}{\partial t} + (\mathbf{v} \cdot \nabla)\mathbf{v} = -\frac{\nabla P}{\rho}; \qquad \frac{d\mathbf{v}}{dt} = -\frac{\nabla P}{\rho}. \tag{2.3}$$

Here P is the pressure. The energy equation for the adiabatic state is:

$$\frac{\partial u}{\partial t} + (\mathbf{v}\cdot\nabla)u = -\frac{P}{\rho}\cdot\mathbf{v}; \qquad \frac{du}{dt} = -\frac{P}{\rho}\cdot\mathbf{v}. \tag{2.4}$$

Where u is the internal energy. These three fluid equations are used as fundamental starting points to derive SPH equations.

2.2 The method

The SPH method, as discussed by Benz (1990); Monaghan (1992), uses a smoothed function $< f(\mathbf{r}) >$:

$$< f(\mathbf{r}) >= \int_V f(\mathbf{r}')W(\mathbf{r}-\mathbf{r}', h)d\mathbf{r}' \tag{2.5}$$

Here $W(\mathbf{r})$ is a kernel, through which the function $f(\mathbf{r})$ is smoothed. Function $f(\mathbf{r})$ is defined within the volume V, while the h represents the size of the kernel. The W is also normalized and thus satisfies the following condition:

$$\int_V W(\mathbf{r}, h)d\mathbf{r}' = 1 \tag{2.6}$$

At small h, the kernel W converges towards the delta function:

$$\lim_{h\to 0} W(\mathbf{r}-\mathbf{r}', h) = \delta(\mathbf{r}-\mathbf{r}') \tag{2.7}$$

The smoothed function itself $< f(\mathbf{r}) >$ converges towards the non-smoothed function $f(\mathbf{r})$ at small h.

$$\lim_{h\to 0} < f(\mathbf{r}) >= f(\mathbf{r}) \tag{2.8}$$

The main goal in deriving SPH quantities is to replace integrals with summations over N discrete points. When $f(\mathbf{r})$ is known at these N points, the number density $n(\mathbf{r})$ can be defined through the summation of delta functions:

$$n(\mathbf{r}) = \sum_{j=1}^{N} \delta(\mathbf{r} - \mathbf{r}_j) \tag{2.9}$$

Multiplying Equation (2.5) by $n(\mathbf{r}')/ < n(\mathbf{r}') >$ and integrating, the expression of $< f(\mathbf{r}) >$ is obtained in terms of summation over N points:

$$< f(\mathbf{r}) >= \sum_{j=1}^{N} \frac{f(\mathbf{r}_j)}{< n(\mathbf{r}') >} W(\mathbf{r} - \mathbf{r}_j, h) \tag{2.10}$$

The number density can be expressed through the particle j mass m_j and the mass density of this particle $\rho(\mathbf{r}_j)$:

$$< n(\mathbf{r}_j) >= \frac{\rho(\mathbf{r}_j)}{m_j} \tag{2.11}$$

By plugging (2.11) into (2.10), the smoothed function $< f(\mathbf{r}) >$ becomes:

$$< f(\mathbf{r}) >= \sum_{j=1}^{N} \frac{m_j}{< \rho(\mathbf{r}') >} f(\mathbf{r}_j) W(\mathbf{r} - \mathbf{r}_j, h) \tag{2.12}$$

This expression is important in terms of deriving smoothed quantities in SPH.

The gradient of the quantity can be defined by applying gradient operator to both sides of the equation (2.5):

$$< \nabla f(\mathbf{r}) >= \int_V \nabla f(\mathbf{r}') W(\mathbf{r} - \mathbf{r}', h) d\mathbf{r}' \tag{2.13}$$

Integrating the right hand side by parts gives:

$$\int_V \nabla f(\mathbf{r}') W(\mathbf{r} - \mathbf{r}', h) d\mathbf{r}' = \int_S f(\mathbf{r}') W(\mathbf{r} - \mathbf{r}', h) \hat{\mathbf{n}} dS - \int_V f(\mathbf{r}') \nabla W(\mathbf{r} - \mathbf{r}', h) d\mathbf{r}' \tag{2.14}$$

By neglecting the surface integral and using the gradient with respect to $\mathbf{r}$ rather than to $\mathbf{r}'$, the expression becomes:

$$< \nabla f(\mathbf{r}) >= \int_V f(\mathbf{r}')\nabla W(\mathbf{r}-\mathbf{r}', h)d\mathbf{r}' \tag{2.15}$$

Finally, this expression of quantity's gradient can be discretised in a similar way to the non-gradient form:

$$< \nabla f(\mathbf{r}) >= \sum_{j=1}^{N} \frac{m_j}{< \rho(\mathbf{r}') >} f(\mathbf{r}_j)\nabla W(\mathbf{r}-\mathbf{r}_j, h) \tag{2.16}$$

Angled brackets in (2.12) and (2.16) can be discarded as there are no integrals left in these equations. Noting further that $r_{ij} = \mathbf{r}_i - \mathbf{r}_j$, $h_{ij} = (h_i + h_j)/2$ (the mean smoothing length, introduced by Evrard (1988)) and $W_{ij} = W(r_{ij}, h_{ij})$, the quantity and quantity gradient equations can be written:

$$f_i = \sum_j \frac{m_j}{\rho_j} f_j W_{ij} \tag{2.17}$$

$$\nabla f_i = \sum_j \frac{m_j}{\rho_j} f_j \nabla_i W_{ij} \tag{2.18}$$

Both equations (2.17) and (2.18) are used to derive smoothed quantities and their gradients in space. This is done by replacing generic function f by any other quantity, which smoothly changes over the space.

2.2.1 SPH kernel

As the kernel has to be even and peaked, Gausian function could be used for the kernel. However, Gausian kernel would have non-zero contribution from distant particles. This would lead to N^2 performance as for each particle it would be necessary not only to loop over the nearest neighbours but also over all other particles in the simulation. For this reason, sphNG uses the M_3 cubic spline introduced by Monaghan & Lattanzio (1985). In 3D space, this function is described as:

$$W(r,h) = \frac{1}{\pi h^3} \begin{cases} 1 - \frac{3}{2}q^2 + \frac{3}{4}q^3 & \text{if } 0 \leq q < 1 \\ \frac{1}{4}(2-q)^3 & \text{if } 1 \leq q < 2 \\ 0 & \text{otherwise} \end{cases} \tag{2.19}$$

with $q = r/h$, where r is the distance from the kernel centre to the measuring point (this is usually the distance between two particles, as in this case the calculation is of what one particle is doing to another).

The kernel and its gradient can be tabulated for easy lookup, making it unnecessary to calculate derivatives and kernels every time kernel is used. As can be seen from (2.19), the kernel contribution extends no further than $2h$. It is also commonly accepted that the number of particles within $2h$ is the same through the entire simulation. These particles, within $2h$ are usually referred as neighbours for the particle in question. When the number of neighbours is fixed, the h on each particle is found as half of the distance to the furthest neighbour. In sphNG, simulations with $50-70$ neighbours are commonly used. Neighbour finding in sphNG is accelerated to $N \log N$ performance due to the use of the binary tree (Press 1986).

2.3 The continuity equation

The continuity equation is the first and the simplest one to derive. It is derived by replacing generic function f with the mass density ρ in Equation (2.17):

$$\rho_i = \sum_{j=1}^{N} m_j W_{ij} \tag{2.20}$$

As particle masses m_j are conserved, this equation satisfies the continuum equation (2.2). The summation here is over all N neighbours of particle i.

2.4 The momentum equation

Benz (1990); Monaghan (1992) derives SPH form of the momentum equation by using Eulerian form of (2.2) and (2.5):

$$\frac{d\mathbf{v}_i}{dt} = -\sum_{j=1}^{N} m_j \left(\frac{P_j}{\rho_j^2} + \frac{P_i}{\rho_i^2} \right) \nabla_i W(r_{ij}, h_{ij}) \tag{2.21}$$

Here $\frac{d\mathbf{v_i}}{dt}$ is the acceleration of the particle i. The summation at the beginning of the right-hand side in equation (2.21) is the summation of the particle's i neighbours. m_j is the m_j neighbour mass. P_j and P_i are the scalar pressures on the corresponding particle calculated from the gas state equation. ρ_i and ρ_j are these particles' densities. Finally $\nabla_i W(r_{ij}, h_{ij})$ is a gradient of the kernel function W. This equation is set in a symmetrical way in order to conserve the momentum for each pair of neighbours in the simulation.

2.4.1 Grad-h formalism

In order to account for the gradient of the smoothing length between two neighbours, Monaghan (2002) implemented the additional term Ω:

$$\Omega_i = 1 - \frac{\partial h_i}{\partial \rho_i} \sum_{j=1}^{N} m_j \frac{\partial W(r_{ij}, h_i)}{\partial h_i} \tag{2.22}$$

The momentum equation with pressure term becomes:

$$\frac{d\mathbf{v}_i}{dt} = -\sum_{j=1}^{N} m_j \left[\frac{P_i}{\Omega_i \rho_i^2} \nabla_i W(r_{ij}, h_i) + \frac{P_j}{\Omega_j \rho_j^2} \nabla_i W(r_{ij}, h_j) \right] \tag{2.23}$$

Here it can be seen that the mean smoothing length h_{ij} is gone, and the smoothing lengths are being treated instead through the derivative $\frac{\partial W}{\partial h}$ in W.

2.4.2 Artificial viscosity

In SPH simulations shocks can occur, where the two fronts of fluid are colliding with their relative velocities to each other being above the speed of sound. Particles in shocks move with high velocities, and it is likely that some will penetrate others without interaction. This occurs when the incoming particle's kinetic energy is not correctly converted into thermal energy. To resolve this problem, artificial viscosity is often used. Monaghan & Gingold (1983); Monaghan (1992) used an additional term in the momentum equation, which is also used in sphNG:

$$\Pi_{ij} = \begin{cases} \frac{-\alpha \bar{c}_{ij} \mu_{ij} + \beta \mu_{ij}^2}{\bar{\rho}_{ij}} & \text{if } \mathbf{v}_{ij} \cdot \mathbf{r}_{ij} < 0 \\ 0 & \text{otherwise} \end{cases} \tag{2.24}$$

with

$$\mu_{ij} = \frac{h\mathbf{v}_{ij} \cdot \mathbf{r}_{ij}}{\mathbf{r}_{ij}^2 + (0.01h^2\overline{c}_{ij})^2} \tag{2.25}$$

In these two equations $\overline{c}_{ij}$ is the mean sound speed and ρ_{ij} is the mean density of i and j particles. h is the smoothing length. $\mathbf{r}_{ij}$ and $\mathbf{v}_{ij}$ are the position and velocity of the i particle relative to the j particle.

α and β are scaling coefficients which determines the strength of bulk and Neumann-Richtmyer viscosity respectively. The bulk viscosity is defined:

$$\Pi_{\text{bulk}} = -\frac{\alpha l c_s \nabla \cdot \mathbf{v}}{\rho} \tag{2.26}$$

Here l is the length scale over which the shock is spread. The bulk viscocity applies to subsonic interactions and can reduce post-shock oscilations. Neumann-Richtmyer is used for supersonic interactions in order to transfer information through the shock:

$$\Pi_{\text{Neumann}-\text{Richtmyer}} = -\frac{\beta l^2 (\nabla \cdot \mathbf{v})^2}{\rho} \tag{2.27}$$

Since Monaghan & Gingold (1983) set values of $\alpha = 1$ and $\beta = 2$, it became common to use these values and thus they are used in sphNG as well.

The final momentum equation with included pressure, grad-h correction and artificial viscosity becomes:

$$\frac{d\mathbf{v}_i}{dt} = -\sum_{j=1}^{N} m_j \left[\frac{P_i}{\Omega_i \rho_i^2} \nabla_i W(r_{ij}, h_i) + \frac{P_j}{\Omega_j \rho_j^2} \nabla_i W(r_{ij}, h_j) + \Pi_{ij} \nabla_i W(r_{ij}, h_{ij}) \right] \tag{2.28}$$

2.4.3 Self-gravity

Self-gravity is often used in star formation simulations. This requires an additional component in the momentum equation. For sink particles, as they are treated as point masses, the self-gravity component can be calculated simply by summing the gravity force over the rest of the

particles:

$$\mathbf{a}_{i,\text{gravity}} = G\sum_{j=1}^{N}\frac{m_j\mathbf{r}_{ij}}{|r_{ij}^3|} \tag{2.29}$$

However, gas particles cannot be treated simply as point particles as their masses are spread out through the volumes of their kernels. Benz (1990) used the Poisson equation to derive the gravitational force from the density:

$$-\nabla\phi = -G\sum_{j=1}^{N}\frac{M_{ij}\mathbf{r}_{ij}}{|r_{ij}^3|} \tag{2.30}$$

where

$$M_{ij} = 4\pi\int_0^{|r_{ij}|} r^2\rho(r)dr = 4\pi\int_0^{|r_{ij}|} r^2 W(r,h)dr \tag{2.31}$$

The integral can be solved by substituting the cubic spline from (2.19) and solving it with respect to r. Equation (2.30) can be substituted into the momentum equation, which, including pressure, the grad-h correction, artificial viscosity and self-gravity, is:

$$\begin{aligned}\frac{d\mathbf{v}_i}{dt} = -\sum_j m_j\left[\frac{P_i}{\Omega_i\rho_i^2}\nabla_i W(r_{ij},h_i) + \frac{P_j}{\Omega_j\rho_j^2}\nabla_i W(r_{ij},h_j) + \Pi_{ij}\nabla_i W(r_{ij},h_{ij})\right] \\ -G\sum_{j=1}^{N}\frac{M_{ij}\mathbf{r}_{ij}}{|r_{ij}^3|}\end{aligned} \tag{2.32}$$

This summation for self-gravity would be over all remaining particles in the simulation, as gravity has a large range meaning that it cannot rely on a calculation over just the neighbours. As a result, the computing performance scales as N^2. To improve this in order to use a larger number of particles, the octree (Barnes & Hut 1986) and binary tree (Press 1986) algorithms were developed. The binary tree is used by sphNG, and as such the computing performance is improved to N log N.

2.4.4 Equation of state

Pressure terms used by the momentum equation are calculated from the equation of state. The pressure P is calculated by rearranging ideal gas equation $PV = NkT$ in terms of gas density ρ and the sound speed c_s in that gas:

$$P = \rho c_s^2 \tag{2.33}$$

The sound speed is dependent on the gas temperature:

$$c_s^2 = \frac{R_g T}{\mu} \tag{2.34}$$

The R_g is the universal gas constant. The mean molecular weight μ is defined:

$$\mu = \left(\sum_i \frac{x_i}{A_i} \right)^{-1} \tag{2.35}$$

with x_i as the mass fraction relative to the total mass for a given atom, and A_i is the molecule or atom mass in hydrogen masses. The sum here is counted over all species in the medium (e.g. H, He, C, O, etc.).

The temperature T in the Equation (2.34) is calculated from the internal energy u:

$$T = \frac{2\mu}{3R_g} u \tag{2.36}$$

The internal energy u is obtained from the energy equation, discussed in section 2.5. Substituting (2.36) into (2.33) and (2.34), the pressure and the sound speed becomes:

$$P = \frac{2}{3} \rho u \tag{2.37}$$

$$c_s = \sqrt{\frac{P}{\rho}} \tag{2.38}$$

Equations (2.37) and (2.38) apply to the isothermal case. In Bonnell et al. (2013) simu-

lations, discussed in this thesis, used the adiabatic equation of state. In the adiabatic case the pressure and the sound speed are given by:

$$P = (\gamma - 1)\rho u \tag{2.39}$$

$$c_s = \sqrt{\frac{\gamma P}{\rho}} \tag{2.40}$$

Here $\gamma = C_P/C_V$ is the adiabatic index which for monatomic gas is $5/3$. This value was used for simulations, discussed in this thesis.

2.5 Energy equation

The fluid must be allowed to evolve while conserving the total energy (in the absence of sources and sinks of energy), which has so far not been touched on.

Benz (1990) gives the expression for the time derivative of the energy. Similarly to the momentum equation, it is expressed in terms of the particle's own properties and a sum over its neighbours:

$$\frac{du_i}{dt} = \frac{P_i}{\rho_i^2} \sum_j m_j \mathbf{v}_{ij} \cdot \nabla_i W(r_{ij}, h_{ij}) \tag{2.41}$$

To incorporate the grad-h formalism, Monaghan (2002) used a constant entropy assumption to derive the internal energy equation:

$$\frac{du_i}{dt} = \frac{P_i}{\Omega_i \rho_i^2} \sum_j m_j \mathbf{v}_{ij} \cdot \nabla_i W(r_{ij}, h_i) \tag{2.42}$$

2.6 Evolution of particles

The evolution of the simulation depends on what types of particles are used. There are three commonly used types of particles in SPH simulations - gas, sink and dead particles. Gas particles (sometimes called just SPH particles) are the main particles, which represent the fluid. Sink particles (or sinks) are point mass particles, which, similarly to N-body particles, only

feel the gravitational force, but can also dynamically replace high density regions of gas and later accrete further. Depending on the level of mass resolution in the simulation, sinks can represent anything from individual protostars to entire clusters of stars. Sinks form from high density gravitationally bound regions of gas particles. Particles which are used to form sinks or are accreted to them transfer their mass and are then converted to dead particles. These remain present in the simulation but are no longer evolved.

2.6.1 Motion of particles

The main feature of particles is that they can move in space, dynamically representing the changing fluid. A particle's motion is defined by its velocity and integration timestep:

$$\mathbf{r}_{\text{new}} = \mathbf{r}_{\text{old}} + \mathbf{v}\Delta t \tag{2.43}$$

This is a simple method of integration used solely for the purpose of illustration. Here $\mathbf{r}_{\text{new}}$ is the new particle's position vector in 3D Cartesian space, and $\mathbf{r}_{\text{old}}$ the old position vector. At a given time each particle has its own timestep Δt and velocity vector $\mathbf{v}$. At the end (or at the beginning) of the time step the particle velocity is recalculated in order to prepare the particle for the next time step:

$$\mathbf{v}_{\text{new}} = \mathbf{v}_{\text{old}} + \frac{d\mathbf{v}}{dt}\Delta t \tag{2.44}$$

Here $\frac{d\mathbf{v}}{dt}$ is the acceleration, calculated from momentum equation (2.32). Depending on the type of the particle, not all force terms are always used. In the case of sinks, pressure and artificial viscosity terms are neglected and only gravity is used. In simulations, where gas particles are used without self-gravity, the acceleration is calculated by using pressure and artificial viscosity terms, and gravity term is neglected.

The specific internal energy of the gas particle changes over the time:

$$u_{\text{new}} = u_{\text{old}} + \frac{du}{dt}\Delta t \tag{2.45}$$

where $\frac{du}{dt}$ is the energy change rate, obtained from energy equation (2.42).

2.6.2 Runge-Kutta two timestep integration

The above equations are simplified for clarity. Modern sphNG uses a Runge-Kutta-Felhlberg method of integration, calculating the positions, velocities and forces at a trial timestep halfway through the full step. A weighted average is then used to find the values after a full step's integration. The weighting coefficients are 1/256, used for the positions, accelerations and internal energies, found at the beginning of the timestep, and 255/256 for the ones calculated at the half-step. This then makes the quantity update equation:

$$x_1 = x_0 + \frac{1}{256}\frac{dx_0}{dt}\Delta t + \frac{255}{256}\frac{dx_{0.5}}{dt}\Delta t \tag{2.46}$$

Here x is a quantity which stands for position, velocity and internal energy of the particle. x_1 is the quantity at the end of the timestep, x_0 the quantity at the beginning of the timestep. $\frac{dx_0}{dt}$ is the quantity change rate at the beginning of the timestep, $\frac{dx_{0.5}}{dt}$ the quantity change rate at the half timestep and Δt is the full timestep.

Particles in sphNG are allowed to have individual timesteps and these are recalculated following each full timestep's integration. The following expression shows how new timesteps are calculated:

$$\Delta t_{\rm new} = \Delta t_{\rm old}\sqrt{\frac{\epsilon}{TE}} \tag{2.47}$$

Here ϵ is the desired level of error in the simulation. TE is the truncation error, which is calculated as:

$$TE = \frac{1}{512}MAX(|v_{x-\rm new} - v_{x-\rm old}|, |v_{y-\rm new} - v_{y-\rm old}|, |v_{z-\rm new} - v_{z-\rm old}|)h \tag{2.48}$$

Here the factor of 1/512 comes from the choices of 1/256 and 255/256 for the weighting coefficients, which allows a higher order integration to the timestep's end. Then the differences between the old and new velocities of the particles in the x, y and z components are calculated. The final velocity difference is found by picking the largest absolute value from these three velocity difference components. h is the particle's smoothing length. This timestep calculation allows the timesteps to be reduced for particles which are fast-moving or in high

density regions, increasing the accuracy of the integration. It also saves computing time by using larger timesteps for particles in low density regions which interact with other particles on longer timescales.

2.7 Sink formation and accretion

In SPH star formation is followed by using sink particles in the simulation. Bate et al. (1995) introduced sinks in order to reduce computing power requirements in high density regions, where particles have very small timesteps. Frequent calculations needed to integrate such small timesteps consume most of the computing power. These regions are usually compact clumps, which collapse to form sinks. A clump of 70 (the number of neighbours used in the particle's kernel calculation) particles in sphNG is replaced by a single sink particle, which interacts with other gas and sink particles only through gravity. The main feature of sinks is that they can form and accrete dynamically in any region when the required conditions occur. As a result sink formation and accretion are the two main processes, which makes sink particles so useful for star formation simulations.

2.7.1 Sink creation

Bate et al. (1995) defined several conditions in order to create a sink particle:

1. $\rho_i > \rho_{\rm crit}$
2. $h_i < r_{\rm crit}$
3. $E_{\rm th} < 0.5E_{\rm grav}$
4. $E_{\rm kin-rot} < 0.5E_{\rm grav}$
5. $E_{\rm grav} + E_{\rm kin-rot} + E_{\rm th} < 0$
6. div $\frac{d\mathbf{v}}{dt} < 0$

The 1. condition is to check if individual gas particle density is greater than a critical density, defined for the whole simulation. As particles are sorted by density at this point, the first particles checked are the highest density ones. The 2. condition is checking if this particle's smoothing length is smaller than a critical distance, which is also defined for a whole simulation. After 1. and 2. pass, the 70 neighbours of the i particle are taken as a subset and further energy tests are performed. 3. checks if the total thermal energy of all 70 neighbours

does not exceed half of their self-gravitational energy. This ensures that thermal energy does not prevent the clump from collapsing. Similarly, 4. ensures that rotational energy will not be able to prevent the clump from collapsing (which would turn the system into a disc rather than a spherical central object). If thermal and rotational energy separately do not exceed half of the gravitational energy, it does not mean they both together could not exceed gravitational energy. For this, condition 5. is needed. The final 6. condition checks the divergence of the accelerations in order to prevent sinks forming in tidally disrupted or bouncing regions.

The sink is created only if all six conditions pass. In this event, the protosink (the original highest density particle used in 1. and 2. steps) is placed at the centre of mass of all 70 neighbours and the protosink. The total mass of all 70 neighbours is also added to the sink. The sink velocity is calculated as the centre of mass velocity of these 70 neighbours. This allows us to conserve the momentum. The angular momentum is also conserved through the spin of the sink. The 70 neighbours which went into sink formation are flagged as dead particles and no longer used in any calculations of the simulation.

2.7.2 Sink accretion

Bate et al. (1995) also defined the continuous dynamical accretion onto existing sinks in the simulation. Two accretion radii are used - the outer accretion radius $r_{\rm out}$, which is usually the same as $r_{\rm crit}$, used for sink creation, and the inner accretion radius $r_{\rm in}$, which is several times smaller than the outer radius. Both inner and outer accretion radii are pre-set before running the simulation and remain constant during evolution in order to remain consistent with level of resolution.

If a gas particle comes within distance $r_{\rm out}$ of the sink, the following checks for accretion are performed:

1. The gas particle is bound to the sink;

2. The particle's angular momentum is small enough that it could be placed on a circular Keplerian orbit at $r_{\rm out}$;

3. The gas particle is more bound to the sink in question than to any other sink.

If these three checks pass, the gas particle is accreted, and its mass, momentum and angular momentum are added to the sink. The sink is placed at the centre of mass of both particles -

the old sink and the accreted gas particle. The sink velocity is changed to that of the centre of mass. And the angular momentum of the accreted gas particle is added to the total spin of the sink. The accreted gas particle is marked as a dead particle and is no longer updated in the simulation. The particle is accreted without any additional conditions if it comes closer than $r_{\rm in}$ to the sink.

2.8 Summary

In this chapter, I reviewed the basics of SPH simulations (especially sphNG) which I use in later chapters to investigate star and cluster formation processes. I started from fluid equations in Eulerial and Lagrangian forms. Then I showed the derivation of smoothed function $< f >$ which is used together with fluid equations in order to derive continuity, momentum and energy equations for SPH. I discussed kernel functions, the usage of M_3 cubic spline in sphNG and the role of particle neighbours. Discussion on SPH equations started from continuity equation, which is used to calculate particle densities. The acceleration equation, which is also known as the momentum equation, was reviewed in detail. The simplest momentum equation for gas particles is based on the pressure gradient, which in sphNG simulations is calculated through particle neighbours. sphNG uses a more advanced version with grad-h formalism through the Ω term. Then I discussed artificial viscosity terms, which are added to the momentum equation as they can reduce post-shock oscillations and help to solve the problem of particle penetration through each other. The self-gravity term in sphNG is derived through the Poisson equation in order to treat particles as fluid elements rather than point masses. The equation of state is used to calculate gas pressure. Then, I reviewed internal energy equation, which is used to account for heating and cooling by thermodynamical processes. The evolution of particles was discussed in terms of position, velocity and internal energy changes over the time. Finally, I reviewed sink formation and accretion conditions, which are commonly used to convert gas particles into sinks.

3

Initial conditions

In this chapter I present an overview of the initial conditions used for the simulations presented in this thesis. These initial conditions are similar to those presented by Bonnell et al. (2013) wherein Global galactic scale simulation and cloud-scale simulations are used.

3.1 The Global simulation

The first simulation, which was later used in Bonnell et al. (2013), was the Global galactic simulation, developed by Dobbs et al. (2006). The principle interest of this simulation is the galactic gravitational potential which includes the disc, halo and spiral arms. The logarithmic disc potential was used with flat rotation curve (Binney & Tremaine 1987):

$$\Phi_{\rm disc}(r,z) = \frac{1}{2}v_0^2 \log\left(r^2 + R_{\rm c}^2 + \left(\frac{z}{q}\right)^2\right) \tag{3.1}$$

Here $R_{\rm c} = 1$ kpc is the halo core radius, $v_0 = 220$ km/s and $q = 0.7$ is the disc scale height.

The spherical dark matter halo has a contribution to the potential:

$$\nabla^2\Phi_{\rm halo}(r) = -4\pi G\rho_{\rm halo}(r) \quad \text{where} \qquad \rho_{\rm halo}(r) = \frac{\rho_{\rm h}}{1+(r/r_{\rm h})^2} \tag{3.2}$$

Here $\rho_{\rm h} = 0.0137$ M$_\odot$ pc^{-3}, $r_{\rm h} = 7.8$ kpc and these are respectively the halo density and halo scale radius (Caldwell & Ostriker 1981).

Finally Dobbs et al. (2006) used Cox & Gómez (2002) in order to define the spiral arm potential:

$$\begin{aligned}
&\Phi_{\rm sp}(r,\theta,t) = -4\pi GH\rho_0 \exp\left(-\frac{r-r_0}{R_{\rm s}}\right)\sum_{n=1}^{3}\frac{C_n}{K_nD_n}\cos(n\gamma)\\
&\gamma = N\left[\theta - \Omega_{\rm p}t - \frac{\ln(r/r_0)}{\tan(\alpha)}\right]\\
&K_n = \frac{nN}{r\,\sin(\alpha)}\\
&D_n = \frac{1+K_nH+0.3(K_nH)^2}{1+0.3K_nH}\\
&C_1 = 8/3\pi, \quad C_2 = 1/2, \quad C_3 = 8/15\pi
\end{aligned} \tag{3.3}$$

Here Dobbs et al. (2006) used $N = 4$ (number of spiral arms), $\Omega_{\rm p} = 2\times10^{-8}$ rad yr^{-1} (angular velocity of the spiral pattern), $\rho_0 = 1$ atom cm^{-3} (the amplitude), $\alpha = 15°$ (pitch angle), $r_0 = 8$ kpc, $R_{\rm s} = 7$ kpc and $H = 0.18$ kpc. Coefficients K_n, D_n and C_n defines how amplitude is dependent on radius.

In order to maximise resolution in the galactic disc Dobbs et al. (2006) distributed particles between 5 and 10 kpc of the disc. The corrotation radius was 11 kpc (from Cox & Gómez 2002) and thus all SPH particles are inside the corrotation radius.

Firstly Dobbs et al. (2006) uses a 2D test simulation with uniformly distributed particles with circular velocities, based on Equation (3.1). The test simulation was evolved for two orbits in the galactic potential in order to get the spiral density pattern. After two periods of rotation Dobbs et al. (2006) adopts the 2D simulation to 3D by using 100 pc disc scale height. Finally, the 2.5 % random Gaussian velocity dispersion of the orbital velocity was injected for all particles in the z direction as well as in the galactic plane (Dobbs et al. 2006).

Simulations in Dobbs et al. (2006) were run with 10^6 and 4×10^6 particles. Bonnell et al. (2013) increased this to 2.5×10^7 particles, which Bonnell et al. (2013) used to get Cloud and Gravity simulations. The total mass of the disc was set to 10^9 $M_\odot$, giving 40 $M_\odot$ resolution per SPH particle and the initial surface density of $\Sigma_{\rm disc} \approx 4.2$ $M_\odot$ pc^{-2} in the Global simulation of Bonnell et al. (2013). The simulation was evolved for 350 Myr of galactic time in order to provide the initial conditions for Bonnell et al. (2013) Cloud and Gravity simulations.

No boundary conditions were used in the simulations of Dobbs et al. (2006) and Bonnell et al. (2013) simulations. As a result a slight distortion was present in the inner and the outer edge of the disc due to the underestimated gas pressure.

3.2 Cloud and Gravity simulations

The high density region from the spiral arm of the Global simulation was chosen in order to initialise the subsequent Cloud and Gravity simulations on smaller scales (Bonnell et al. 2013). The region of 250 pc size containing 1.71×10^6 $M_\odot$ mass and 272500 particles was taken at the Global simulation time of 350 Myr. Each particle was split into 256 smaller mass particles, increasing resolution from 40 $M_\odot$ down to 0.156 $M_\odot$ per SPH particle.

Bonnell et al. (2013) used the following methods to include the boundary particles. Simulation was set for the region to include boundary particles, which were traced for 54 Myr (1/4 of the galactic orbit) backwards in time. Such boundary particles are considered to be all those which came within 40 % of the size of the region at any time within this 54 Myr period. Those which came closer than 15 % are additionally split in 4 lower mass particles. A third group of boundary particles was made up of those which came closer than 10 h (the SPH smoothing length) of any particle in the region of interest. The particles in this group were split 16 times. A fourth group of particles was found in the same way as the third, but instead included particles within 4 h of the region. These were split into 64 particles. This setup means particles can encounter others whose masses are different by factors of 4. Bonnell et al. (2013) evolved these boundary particles in the same way as the regular SPH particles together with the region of interest particles. After including boundary particles, the number of particles is set to 2.8×10^7 and the total mass in the simulation 3.09×10^7 $M_\odot$.

Bonnell et al. (2013) evolves the region of Cloud simulation between 310 and 364 Myr (for 54 Myr time) of the Global simulation timescale. During this time, the cloud experiences

its full life cycle, i.e. formation, maximum compression and being torn apart in the galactic tidal field.

The last in the set of Bonnell et al. (2013) simulations is the Gravity simulation, which was the one used in this thesis. Bonnell et al. (2013) derived the Gravity simulation from the high density central 250 pc of the Cloud simulation. Bonnell et al. (2013) sets the evolution to begin at a galactic time of 350 Myr and go on for a further 5 Myr. Unlike the Global and Cloud simulations, the Gravity simulation included self-gravity, calculated according to the (Press 1986). Star formation was simulated with the dynamic formation of sink particles from self-gravitating gas (Bate et al. 1995). I discussed sink formation and tree codes in more detail in Chapter 2.

3.3 Cooling function

The Bonnell et al. (2013) Global, Cloud and Gravity simulations used a gas cooling function originally derived by Koyama & Inutsuka (2000, 2002) and later improved upon by Vázquez-Semadeni et al. (2007). The cooling function is described in terms of heating Γ from background radiation and cooling Λ by atomic, molecular and dust processes:

$$\frac{\Lambda(T)}{\Gamma} = 10^7 \exp\left(\frac{-114800}{T+1000}\right) + 0.014\sqrt{T}\exp\left(\frac{-92}{T}\right) \tag{3.4}$$

Here Koyama & Inutsuka (2002) used the constant value for heating Γ of 2×10^{-26} erg s^{-1} in the galactic disc.

The equilibrium temperature $T_{\rm eq}$ is the temperature at which heating and cooling rates are balanced. The equilibrium is given at the density $n_{\rm eq}$:

$$n_{\rm eq} = \frac{\Gamma}{\Lambda(T_{\rm eq})} \tag{3.5}$$

To find the equilibrium density Equation (3.4) must be inverted, giving the temperature as a function of the cooling rate, i.e. $T(\Lambda)$. The code does this by tabulating the cooling rate over a logarithmic grid in (n, T) space. After adding the rate of change in internal energy due to hydrodynamic processes to the heating Γ and cooling Λ terms, the energy equation becomes:

$$n\left(\frac{du}{dt}\right)_{\text{total}} = n^2\Lambda + n\Gamma + n\left(\frac{du}{dt}\right)_{\text{hydro}} \tag{3.6}$$

Here $\left(\frac{du}{dt}\right)_{\text{hydro}}$ is the internal energy change rate from compression and expansion, discussed in Chapter 2.

Vázquez-Semadeni et al. (2007) gives the cooling timescale, which is the time needed for gas to reach the equilibrium internal energy from its current given value. By adding the $\dot{u}_{\text{hydro}} = \left(\frac{du}{dt}\right)_{\text{hydro}}$ term, the Vázquez-Semadeni et al. (2007) cooling timescale becomes:

$$\tau_\Lambda = \left|\frac{u - u_{\text{eq}}}{n\Lambda(T) - \dot{u}_{\text{hydro}} - \Gamma}\right| \tag{3.7}$$

Finally Vázquez-Semadeni et al. (2007) give the equation for updated particle's internal energy:

$$u_{\text{new}} = u_{\text{eq}} + (u - u_{\text{eq}})\exp\left(-\frac{dt}{\tau_\Lambda}\right) \tag{3.8}$$

Here u_{new} is the new internal energy of the particle, u is the old internal energy of the particle from the previous timestep and dt is the timestep.

This cooling function is used in the Bonnell et al. (2013) simulations to allow a two-phase interstellar medium (ISM) to develop naturally. This two phase ISM (Field et al. 1969; Wolfire et al. 1995) is in pressure equilibrium between warm ($T \approx 10^4$ K) and cold ($T \approx 10$ K) gas.

4

Cluster finder

Clustering analysis is one of the most difficult problems, not just in astronomy, but also in computer sciences, medicine, statistics and data analysis (Hartigan 1975; Jain et al. 1999; Zhao & Karypis 2005; Soni & Ganatra 2012). The most natural cluster detection "algorithm" is the human eye. However, in large datasets, manual cluster finding would become a very slow and tedious process. The best solution here is to develop an automatic cluster finding algorithm, where a computer program could find clusters in the most realistic way, comparable with human eye detection. However, cluster finding algorithms are not easy to develop, and often come with limitations.

Due to different applications of clustering, and the variety of features and algorithm limitations, a large number of algorithms have been developed (Soni & Ganatra 2012; Zafar & Ilyas 2015). Soni & Ganatra (2012) in their Figure 2 present a detailed tree-scheme of how clustering algorithms can be classified. They divide cluster finding algorithms into two categories - partitioning and hierarchical. Density based clustering algorithms (which Soni & Ganatra 2012 classified in the partitioning category) are likely to be a good fit when finding stellar

clusters in simulations. Hierarchical clusters can also be used, especially in the regions where clustering itself is hierarchical. Hierarchical clustering also allows us to build a full hierarchical tree-dendrogram which can be used to analyse clustering at different scales. K-means based clustering algorithms are also popular in data science, but they use a number of clusters in the dataset as a pre-defined parameter. Thus K-means algorithms are not the best solution for simulations in which a number of clusters are unknown before the algorithm begins to search.

A cluster in a dataset is a group of data points which have similar properties to one another. In astronomy, the term 'stellar cluster' refers to a group of stars visible at a similar position. Observationally it is often done in 2D, when clusters are defined as groups of stars in the plane of the sky. In order to obtain 3D geometry, distances to individual stars of the cluster would be needed. In simulations, all three dimensions are available and clusters can be defined in 3D. The density of stars in a stellar cluster is higher than in the surrounding background, so a cluster finding algorithm should be able to identify these groups of stars in higher density regions.

In this thesis, I used a gravitational potential based algorithm (which is a sub-class to the density based algorithm) in order to find clusters in star formation simulations in a manner most closely approximating the method performed by the human eye.

4.1 Gravitational potential based clustering

The human eye naturally sees high density nearly spherical regions in simulations as clusters. Sinks remain in the forming clusters for several crossing times as they are gravitationally bound to the cluster and thus are moving inside the global gravitational potential of the cluster. Filaments, which are also present in star forming regions, can be collapsing and present as short-lived structures at a given time. As a result, the cluster finder should identify already formed clusters and separate them from filamentary and other short-lived structures. As the boundedness of the cluster is so important, the gravitational potential based cluster finder is likely to be a good solution.

4.1.1 Local and enclosed gravitational potentials

Before starting the cluster finding algorithm, the first thing to be done is to calculate the local gravitational potentials at all sinks in the simulation. Potentials are often used in order to

estimate the gravitational field in simulations but potentials can also be used in order to find clusters. The local potential at each given sink can be calculated by using other sinks:

$$\Phi_i = -G \sum_{j=1}^{N} \frac{m_j}{R_{ij} + \epsilon} \Bigg|_{R_{ij} < R_{\mathrm{pot-out}}} \tag{4.1}$$

Here Φ_i is the local gravitational potential measured at the sink i. m_j is the mass of another sink j. R_{ij} is the distance between particles i and j. ϵ here is a tiny distance, through which potential is smoothed in order to avoid contribution from close binary sinks. Potential calculations are also limited at large radii by $R_{\mathrm{pot-out}}$ - the external radius, beyond which other sinks from the simulation are not included in the potential calculations. In this thesis values of $R_{\mathrm{pot-out}} = 2$ pc and $\epsilon = 0.05$ pc were used. If the nearest neighbour sink j for the sink i is beyond $R_{\mathrm{pot-out}}$, the potential $\Phi_i = 0$ and the sink i is not used in the cluster finder.

The enclosed gravitational potential Φ_{enc} is also used in the potential based cluster finding algorithm. The enclosed potential is relative to the centre of mass of the cluster in question. As a result, the enclosed potential is calculated as:

$$\Phi_{\mathrm{enc},c,k} = -G \sum_{j=1}^{k} \frac{m_j}{R_{\mathrm{com},j}} \Bigg|_{R_{\mathrm{com},j} < R_{\mathrm{pot-out}}} - G \sum_{j=k+1}^{N} \frac{m_j}{R_{\mathrm{com},k}} \Bigg|_{R_{\mathrm{com},k} < R_{\mathrm{pot-out}}} \tag{4.2}$$

Here $\Phi_{\mathrm{enc},c,k}$ is the enclosed potential calculated for the sink k, relative to the cluster c. The list of all sinks in the simulation is sorted by the distance of each sink to the cluster c centre of mass. The first sum is over internal sinks, which are closer to the cluster c centre of mass than the sink k and no further than the $R_{\mathrm{pot-out}}$ (which was set to 2 pc). The second sum is over all the remaining sinks which are further away from the cluster c centre of mass than the sink k but also no further than the $R_{\mathrm{pot-out}}$. The m_j is the j sink mass and the $R_{\mathrm{com},j}$ is the j sink distance from the cluster c centre of mass. $R_{\mathrm{com},k}$ is the k sink distance from the cluster centre of mass. If the sink k is further away than $R_{\mathrm{pot-out}}$, its enclosed potential is only calculated from internal sinks which are closer to the cluster centre of mass than $R_{\mathrm{pot-out}}$; this means that enclosed potentials beyond $R_{\mathrm{pot-out}}$ are flat. Enclosed potentials are only calculated when there are clusters already found in the simulation. Otherwise, only local potentials are used in the definition until the first cluster is found.

4.1.2 Definition criteria

Once the local gravitational potentials are known at every sink particle, the cluster finder can begin to search. The search follows these steps:

1. The list of sinks is sorted by local potentials.

2. The lowest potential sink is taken from the sinks list. The sink's local potential is checked against the critical background potential threshold above which the cluster finding algorithm ends.

3. If there are no previously classified clustered sinks, the current sink is immediately added to the first cluster c_1 and the cluster finder goes back to step 2 in order to find the next lowest potential sink. If other sinks have previously been classified as clustered, next steps are done in order to find if the current sink should be added to one of the already defined clusters.

4. The enclosed potentials, relative to the existing clusters, are calculated for the given sink candidate as described in Equation (4.2). The first cluster taken for enclosed potential calculation is the one whose centre of mass is closer to the sink in question than any other cluster centre of mass.

5. The ratio of the local sink potential to the enclosed sink potential of the nearest cluster should not exceed 2, as low local sink potential is likely to be caused by another cluster. If this criterion fails, then step 4 is repeated to find the next nearest cluster and the ratio is checked again. This repeats over all already found clusters.

6. If step 5 fails and the local to enclosed potential ratios are found to be greater than 2 for all clusters, then no other cluster can add a contribution to such low local potentials. A new cluster is created and the sink assigned to it.

7. If step 5 passes, the sink is added to the nearest cluster satisfying the potential ratio criterion.

8. Steps 2 to 7 are repeated over all remaining unclustered sinks until either the end of the list, the zero or the background potential is reached.

9. Clusters smaller than 6 sinks and also gravitationally unbound clusters are removed after 1 to 8 finishes.

Defining clusters by following these steps allows us to find clusters starting from the lowest potential sinks moving outwards. In the case of filamentary structure, the lower potential in the filament could be a subcluster and the definition does not spread along the filament. This is because when sinks are distributed in a filament, the enclosed potential rises rapidly, while the local potential remains nearly the same. The 5th criterion fails to classify sinks which are not in clusters but instead in filaments as being clustered.

4.1.3 Free parameters

As it can be seen, the cluster finder has several free parameters, which the user can choose before running the algorithm. Here is the summary of these parameters:

1. $\Phi_{\rm bg}$ - local gravitational potential background threshold. This prevents the definition from spreading into large potential areas, where non-clustered sinks are present (distributed mode). The background threshold has been set throughout this thesis to -10^{11} cm^{2}s^{-2}, as this is where virialised motions of sinks were no longer observed (see subsection 4.1.4 for mode detail).

2. The ratio between local and enclosed gravitational potential. This prevents the definition from spreading into other clusters. Large values of the ratio allows definition to spread into other clusters easier and merge them together. Small values of ratios allow us to separate smaller subclusters. The ratio value was chosen (by eye) to be 2 through this thesis.

3. $R_{\rm pot-out}$ - the outer radius at which both local and enclosed gravitational potentials are limited. This allows the user to chose the locality from which gravitational potential calculations are most desirable. Large values of $R_{\rm pot-out}$ can include more contribution from inter-cluster sinks and thus weaken the effect of the potential of the cluster in question. Small values can include contribution only from a part of the cluster. The chosen value in this thesis is 2 pc.

4. ϵ - the tiny distance, used to smooth local gravitational potential calculations. This is used primarily to avoid significant potential contribution from binary sinks and instead focussing on the cluster scales.

5. Minimum number of sinks in the cluster. This parameter allows us to avoid clusters with a small number of sinks, which would give low number statistics. The value was chosen to be 6 through the thesis.

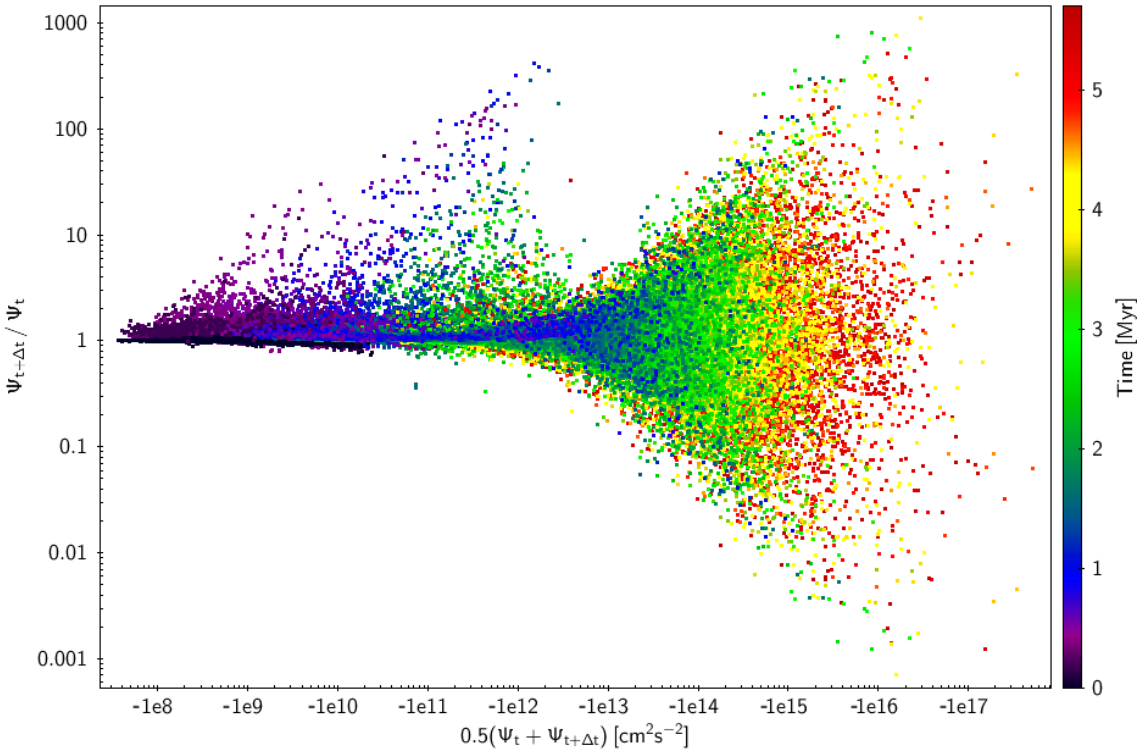

Figure 4.1: The gravitational potential threshold can be determined by measuring the changes in the potential from the virialised motions of sink particles. Changes in the gravitational potential over time are shown in this diagram as a function of the potential itself. The virialised motions of clustered sinks are clearly seen at potentials smaller than -10^{11} cm^{2}s^{-2}. This can be used as a potential threshold in order to separate clustered and distributed modes.

4.1.4 Background potential threshold

The background potential threshold is a free parameter and difficult to estimate. The problem arises as the transition between clustered and distributed sinks is smooth. However, the virialised motions of sinks in the cluster can help here. Figure 4.1 shows how the local gravitational potential of sinks changes over time in the Bonnell et al. (2013) simulation. The mean potential between two timesteps is plotted on the horizontal axis (note that due to potentials being negative, the direction of the horizontal axis is from right to left). On the vertical axis is the ratio of potentials at these two timesteps. This is repeated over all timesteps of the simulation. Sinks (and protosinks, i.e. gas particle which becomes a sink at a later time) at higher potentials do not belong to any cluster and thus the change of the potential can be explained by large scale motions only. At lower potentials, sinks are in clusters and their motions virialised. As a result, the potential ratio is scattered more at smaller potentials. Virialised motions end at potentials larger than -10^{11} cm^{2}s^{-2} where the distributed and clustered modes can be separated. This threshold was used at step 1 in the cluster finding algorithm, described

in subsection 4.1.2.

4.2 Tracing clusters over time

A cluster finding algorithm allows us to find clusters of sinks in a single timestep. However, these simulations are of particular use because they show the evolutionary process of cluster formation. When the simulation was run it produced this evolution, but it is still not clear which particles contributed to the clusters, how and why particular regions formed clusters, and what their formation histories are. Do sinks remain in their clusters, or do they move out? These questions can be answered by tracing the cluster definition over time.

4.2.1 Connecting two timesteps

The best method of tracing clusters is to develop a time-independent tracing algorithm, as at individual timesteps it is important to find clusters without knowing their evolution (as is the case for observations). In order to do this it is firstly necessary to find the clusters at each timestep, independently of the other timesteps. The cluster IDs may not necessarily match for the same cluster across different timesteps. The main task then is to map the connection between the same clusters in time. In order to find if the cluster is the same at time t_i and t_{i+1}, the list of cluster members can be used. The cross matching is performed between the sinks in cluster "A" at time t_i and all the clusters found at t_{i+1}. Cluster "B" at t_{i+1} is taken to be the same as cluster "A" at t_i if cluster "B" has more mass from the sinks in cluster "A" than any other cluster at time t_{i+1}. Here $\Delta t = t_{i+1} - t_i$ is a free parameter. In this thesis Δt was set to the full timestep in the simulation, which in the Bonnell et al. (2013) simulation is 0.05 Myr.

4.2.2 Cluster events between timesteps

There are six events which a cluster can experience between two timesteps (Figure 4.2) and the tracing of clusters through time should properly account for them.

1. **Cluster merging.** This event occurs when two clusters merge into a single more massive cluster. Merging occurs when two clusters with different IDs at the earlier timestep are found to place most of their mass in a single cluster at the next time. Usually, when two clusters merge, one is more massive than the other. The more massive cluster is described as the "parent", while the less massive one is the "child". A major merger event occurs when the child

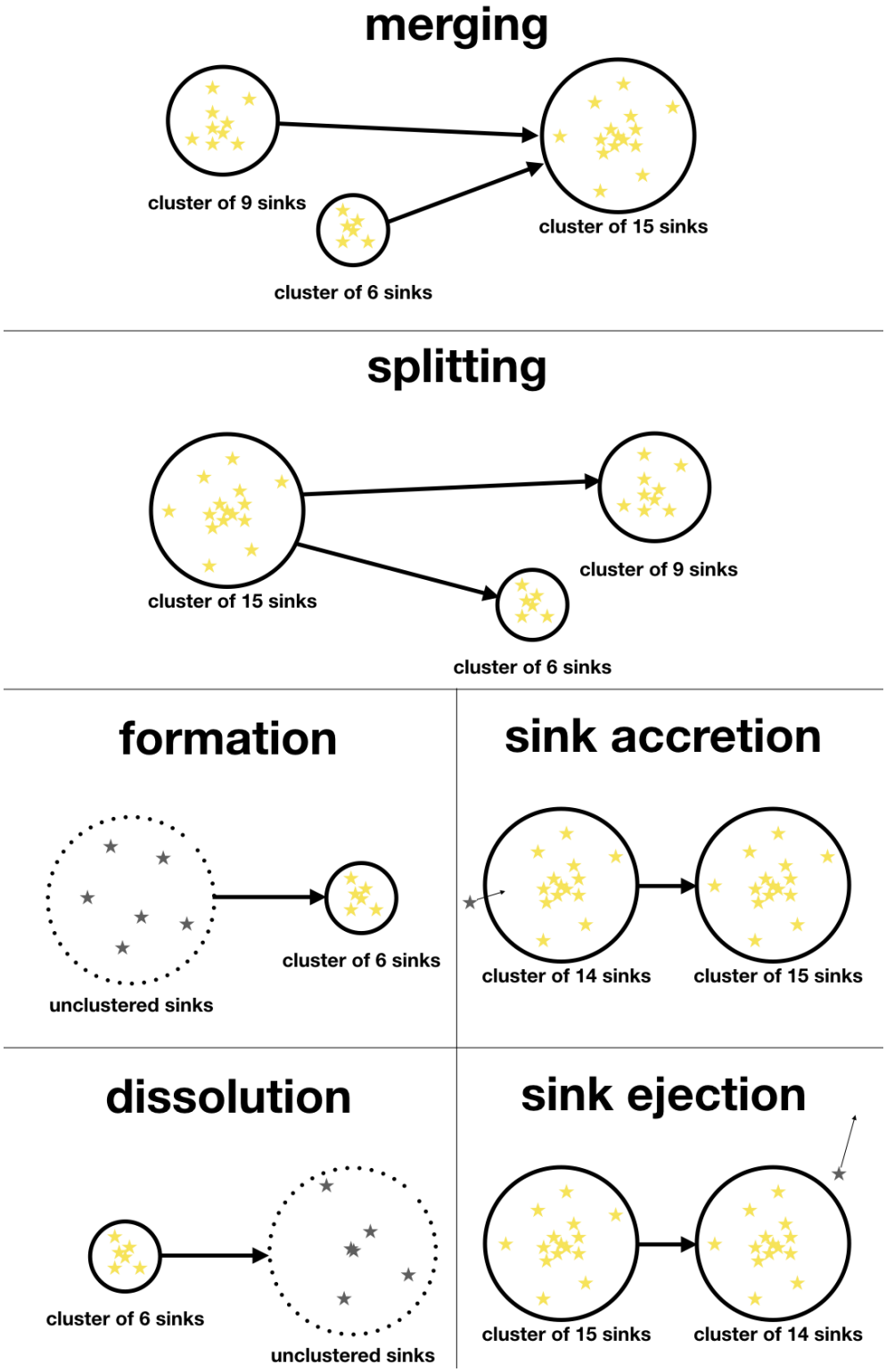

Figure 4.2: This cartoon shows six possible events which can occur when tracing clusters through time. Mergers, producing larger clusters, are common, while splitting is rarer. New clusters can form from groups of sinks which come together in a compact region of space. They can also dissolve if they become unbound. Sink accretion and ejection events are also possibilities. These six events are the full set of possibilities while tracing cluster formation and evolution.

cluster contributes more than 30% of the total mass of the merged cluster, and minor mergers otherwise.

2. **Cluster splitting.** This is a rare event in which a single cluster splits into two. This can happen if two clusters are not fully merged and the gap between them increases. This can occur, for example, if one cluster is falling into another but there is not enough gas in the collision region to dissipate the energy and cause the accretion of the infalling cluster. In such a case, when the separation is the minimum the clusters would be taken to be merged, but part of the infalling cluster would continue to move away from the collision. Several infalls may be needed until the child cluster fully merges with the parent. So far splitting has not been seen in clusters found from the Bonnell et al. (2013) simulations as clusters merge almost immediately, but it can take place in N-body and especially cosmological simulations.

3. **Cluster formation.** This is a typical event in which a cluster is defined for the first time. Usually, this occurs with six sinks initial clusters. This can be different if two subclusters with less than six sinks individually merge and form a cluster with more than six sinks.

4. **Cluster dissolution.** This takes place when sinks in the next timestep are classified as being unclustered. This can occur due to physical reasons in small clusters of six sinks when one of the sinks is moving away from the rest. It can also occur if the cluster expands and the potential criterion is no longer satisfied, or if the cluster is stripped due to tidal disruption and its shape is extended. The cluster can also split into two subclusters, each possessing fewer than six sinks which would then by definition be treated as unclustered.

5. **Sink accretion.** This event describes the addition of an unclustered sink (one or more) to an existing cluster at the next timestep. Usually this happens when new sinks, recently formed in the cluster's periphery, fall into that cluster while satisfying the local and enclosed gravitational potential criteria. This could also take place when the sink is on a highly elliptical orbit. At the apocentre of the orbit, the sink may not satisfy the potential criterion, and so it would be treated as unclustered. When it begins to move back towards pericentre, it would once more be assigned to the cluster. This would oscillate sinks between the states of being assigned and unassigned.

6. **Sink ejection.** The ejection event occurs when the sink moves out of the cluster and becomes classified as unclustered. This could be a real event such as when a sink in a cluster is ejected through a three-body close encounter event. This might give the sink a large enough

velocity to unbind it, causing it to leave the cluster indefinitely. Sink ejection may also occur if a sink enters a large orbit but remains bound, causing it to later return, as mentioned above for sink accretion.

Including treatment of these six events in the cluster tracing algorithm allows us to trace dynamical cluster formation over time. It is also possible to trace short-lived clusters, determine cluster lifetimes and merger histories, and build cluster merger trees. The cluster mass merger tree is a diagram, which shows how cluster mass changes over the time. The mass merger tree has imprinted merging and accretion events along the cluster mass evolution.

The mass merger tree can be quite "noisy" when individual sinks are assigned and unassigned according to the criteria above. In order to smooth it, two solutions can be used: to use the time-dependent cluster finder, or to smooth over time. The time-dependent definition is to find the sinks in the cluster at t_i and check if at t_{i+1} they still define the same cluster. However, this removes the method from the observation-based definition i.e. an observer would need to know cluster formation histories in order to define them. The tree can be smoothed over time by checking cluster membership over longer periods of time, for example by checking whether a sink has been assigned to a given cluster not only from t_i to t_{i+1} but also to t_{i+2}. For example, if a sink is found to be assigned to the same cluster at t_i and t_{i+2} but not at t_{i+1}, it is assigned back to the cluster at the missing timestep t_{i+1}. Repeating over multiple timeseps, this method smooths cluster evolution tracks in the merger tree. In this way there is no need to know cluster histories as the smoothing would not be used if the cluster state at other timesteps is not known. Time tracing can be used both forwards and backwards. The results produced in this thesis are based on the smoothed merger tree and backwards tracing in time.

4.3 Summary

In this chapter I discussed the new cluster finding algorithm which I use for identification of clusters of sinks in SPH simulations. A large number of cluster finding algorithms exist, but each was usually developed for use in a particular case. The cluster finder adopted for finding sink groups in SPH simulations is based on gravitational potentials.

The potential based algorithm uses the local and enclosed gravitational potentials as calculated for sink particles to find the boundaries between clusters and the background, and to

separate individual clusters. I discussed the steps at which the algorithm uses these potentials in order to find clusters. The algorithm has five free parameters which need to be set before running. This includes the potential threshold, the critical ratio between local and enclosed potentials, the outer radius which limits local and enclosed potentials, the smoothing distance in local potentials, and the minimum number of sinks needed to recognize the cluster.

I also discussed my solution for the long-standing problem of how to trace clusters through sequential timesteps in numerical simulations. Firstly, I defined the cluster tracing method between two successive timesteps. Numerous processes both numerical and physical may take place. These are cluster creation, dissolution, merging, splitting, and individual sink accretion and ejection. I also covered how to identify specific clusters across time by finding which clusters retain the majority of their mass from the same sinks in subsequent timesteps. Finally I discussed how to allow clusters to be traced over more than two timesteps, and how noise can be removed from the results by smoothing.

5

Triggering star formation

Star formation in galaxies is not well understood, and how effective the triggering of star formation really is remains largely debatable. Many processes may help to trigger star formation, such as spiral arm passage (Dobbs et al. 2015), cloud-cloud collisions (Bisbas et al. 2017), and stellar feedback (i.e. stellar winds, supernova (SN), Elmegreen 2011). However, it is still unknown which processes dominate and are potentially responsible for the creation of the majority of stars in spiral galaxies. The most energetic processes are likely responsible for the distribution of kinetic and gravitational energies in the galaxy and therefore play a key role in star formation. Passage through a spiral arm is the most energetic process, as it compresses clouds in the interstellar medium (ISM) and enables them to reach the point at which they can become self-gravitating.

While spiral arm passage, cloud-cloud collisions and stellar feedback triggered star formation brought some answers, it remains unclear at what scale clouds become gravitationally bound and how the collapse progresses. While simulations such as Dobbs et al. (2015) provide a good background and Bate et al. (2003), Smith et al. (2009), Bonnell et al. (2011)

investigate in detail the formation of stellar clusters, the link between these two fields remains missing. Thus the main reason of this chapter is to address the missing properties of star forming clouds.

As a result I have investigated in detail the compression of the ISM and star formation during spiral arm passage. I start my analysis with the simulation data of Bonnell et al. (2013) in which star formation was observed during spiral arm passage. Star forming regions in Bonnell et al. (2013) simulation are represented by dynamically forming and later accreting sink particles. However, as the simulation was designed to resolve over 400 pc size region in the spiral arm, minimum sink mass is set to 11 $M_{\odot}$. Due to that, sinks can't resolve individual stars and instead represent groups or small clusters of forming stars.

5.1 The region structure

5.1.1 Spiral shock and velocities

The spiral shock provides the triggering mechanism for star formation and thus I discuss it first. Figure 5.1 shows the position-position-velocity map for the initial conditions of the gas in the simulation. The map shows the x-y positions of the particles, which are equivalent to a face-on view of the galactic plane. The positions and velocities as shown in the diagram are relative to the centre of mass (for all particles in the simulation) values. The direction of galactic flow is almost parallel to the y-axis, so the shock is strongest in this direction. As a result, I show the v_y velocity component, which demonstrates the greatest difference between pre- and post-shock velocities, making the shock front itself visible. In Figure 5.1 particle positions are colour coded by v_y. The flow of low density gas from the inter-arm region is visible as red diffuse clouds in the lower left part of the diagram. This gas moves in a positive-y direction with $v_y \sim$ 10-20 km/s. The post-shock gas is visible as chunky high density material in the central region of the diagram, extending from the upper left to the lower right side as blue-green material. These gas particles move at $v_y \sim 0$ to -10 km/s. Thus, the difference between the pre- and post-shock velocities is around 20-30 km/s in the y-direction.

Due to this strong supersonic shock the front side forms pillars. They form as the pre-shock gas pushes lower density regions more efficiently into the spiral arm, while the higher density regions remain less affected. The gas in the tails of the pillars is well protected by a shielding effect from the pillar heads, which are usually high density clumps. The lower density pre-

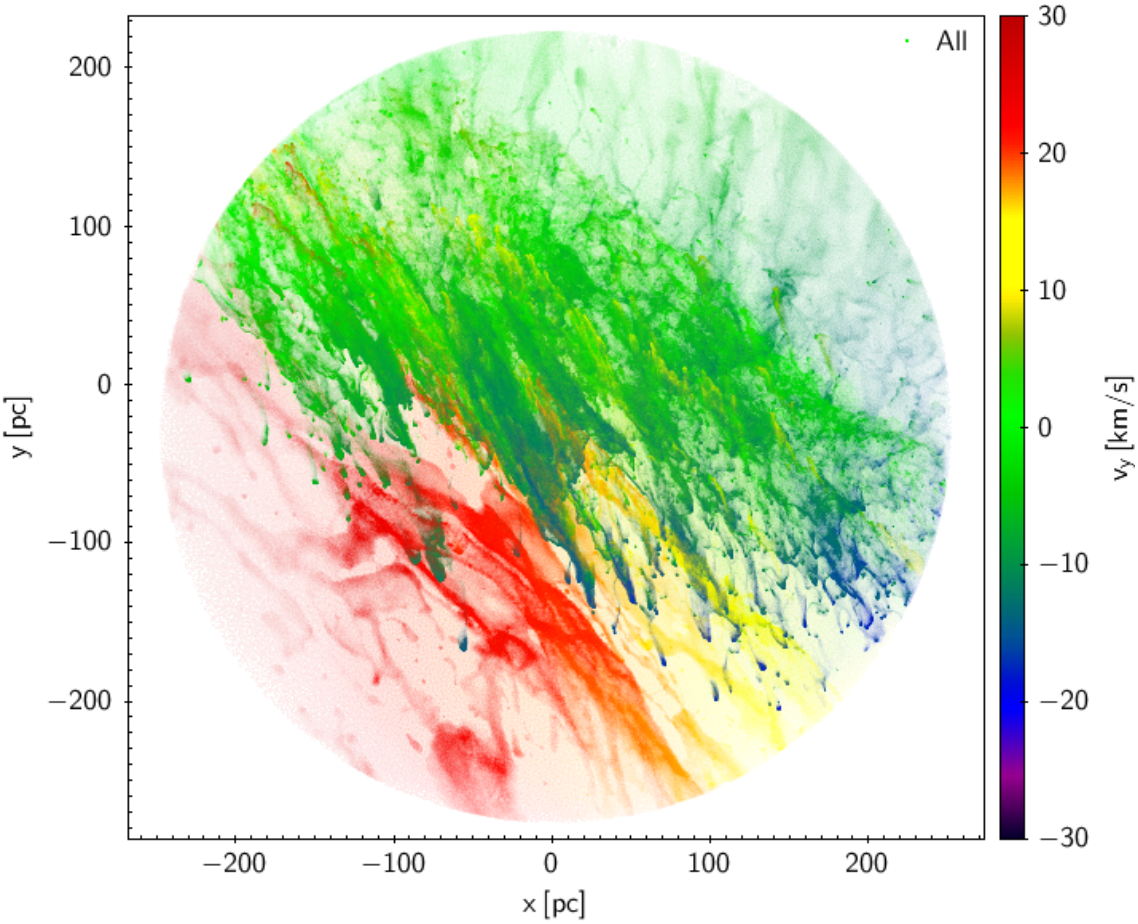

Figure 5.1: The galactic spiral shock is shown in this diagram in terms of velocities. This is a position-position-velocity map of all the gas particles at the beginning of the simulation, with particle velocities in the y-direction given by their colours. The velocity is taken relative to the centre-of-mass of the simulation. The shock front is clearly visible in the diagram, with a nearly 30 km/s difference in velocities between the pre- and post-shock material.

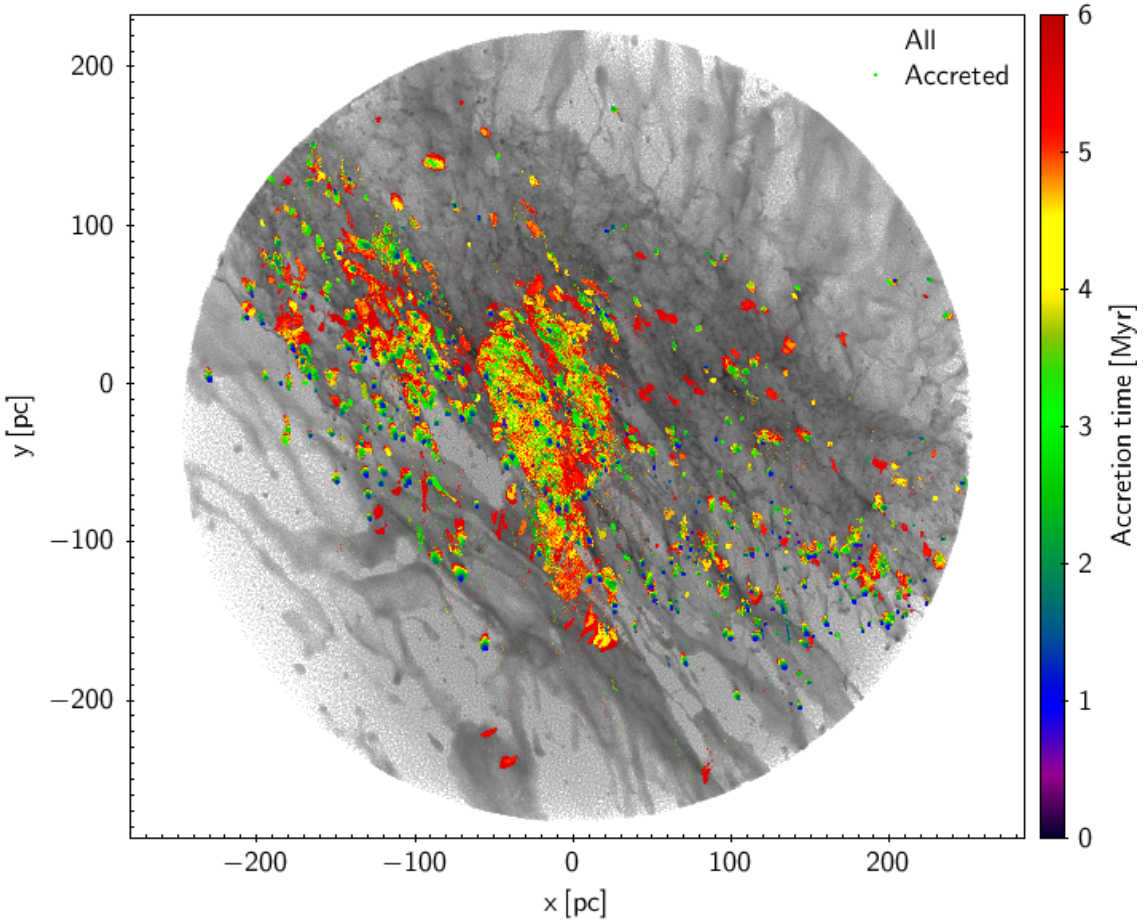

Figure 5.2: This plot maps where sink formation and accretion took place in relation to the overall distribution of gas. Grey dots show the positions of all the gas particles, while coloured dots represent accreted gas, with the colour indicating the time at which they were accreted. The map shows the locations of sink forming regions as well as the larger reservoirs of sink forming gas. As the plot shows, early sink formation and accretion occurs in compact high density clumps, while late sink forming and accreted gas undergoes collapse from large scales.

shock gas is not uniform either, and as a result the galactic flows create clumpy shocks as have been investigated in earlier works (Clark & Bonnell 2006; Dobbs & Bonnell 2007).

5.1.2 Sink forming regions

The spiral shock compresses the ISM gas to higher densities. If the density is high enough, the region becomes gravitationally bound and starts to collapse. This leads to sink formation, which I plot in Figure 5.2. The positions of all the gas particles in the simulation are plotted in grey-scale. Gas particles which are accreted at some point in the simulation are plotted on top and colour-coded according to the simulation time at which that occurs (accretion time).

Regions where sink formation and accretion have occurred are clearly visible. The main sink forming region appears as an extended ridge elongated along the direction of gas flow.

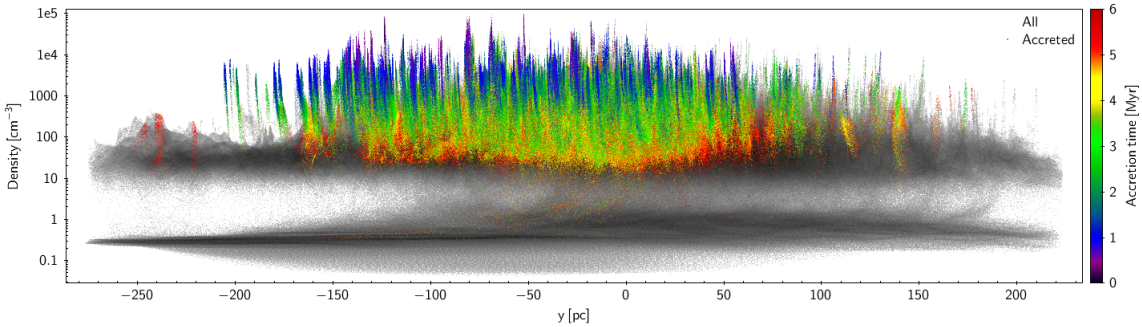

Figure 5.3: "Cities diagram". The diagram shows gas particle densities plotted against y position at the beginning of the simulation. Grey particles represent all gas in the region, while on top are particles accreted at a time indicated by their colour-coding. The diagram shows that high density particles are accreted first, while lower density particles follow after at later times. The cold high density spiral arm gas and warm low density inter-arm gas is visible as a multi-phase medium of the gas. The shock approaches from the left-hand side of the diagram. It can be seen that sink formation and accretion is triggered first in the highest density regions while later accretion follows from lower density gas from extended sink reservoirs.

There are also dozens of individual smaller clouds, scattered along the spiral arm. The map shows the size scales on which sink formation and accretion takes place: the main region is about 150-200 pc long, and 30-40 pc wide. However, as can be seen from the colour-coding, sink formation and accretion takes place on different scales at different times. Early sink formation and accretion appears to be concentrated into compact clumps, which form first, while later gas is accreted from extended reservoirs distributed across larger scales. This shows that gas particles accreted early on were already close to the locations at which they were accreted, while particles which were initially more distant needed time to travel to the accretion sites.

In Figure 5.3 I plot the same particle y-positions against the SPH gas densities for all and accreted gas particles. This plot shows the multi-phase nature of the gas in the simulation, with cold high density gas present alongside warm low density gas. Accreted particles were for the most part initially in the high density phase and show good correlation between accretion time and gas density. As a result, early sink formation and accretion takes place in high density gas (i.e. $\approx 10^4$ cm^{-3}), while later sink formation and accretion is extending to lower densities (down to ≈ 100 cm^{-3}). Gas particles must not only move closer to their accretion sites, but must also increase in density to the point where sink formation can take place. The tiny clumps seen in Figure 5.2 are seen in Figure 5.3 instead as thin blue columns rising towards the highest densities. Sink formation and accretion densities in this simulation are set between 6.8×10^3 and 1.1×10^6 cm^{-3} (which are based on the assumption that gas would be distributed uniformly within 0.1 pc and 0.25, respectively the inner and outer accretion radii). It is between these

densities that gas particles are converted to sinks and the vertical columns, visible in Figure 5.3, do not approach the higher densities.

5.2 Properties of sink forming reservoirs

In order to fully understand star formation we must be able to explain the physical properties of star forming regions and follow them over time. Masses, sizes and energies are the primary ones, which can be measured directly from simulation data. I discuss here the properties of individual sink forming reservoirs (note that the sinks in the Bonnell et al. (2013) simulations do not represent individual stars).

5.2.1 Sink forming masses

At the beginning of the simulation, only gas particles are present. The first sinks start to form at around a simulation time of 0.5 - 1 Myr. They also can accrete gas particles later. I track all accreted particles in order to find their distribution at all time steps. As each sink is forming from its gas reservoir, the mass between time steps is conserved. In other words, this conserved sink reservoir mass is the total mass of the sink itself, combined with the gas particles yet to be accreted at any time, or the final sink mass at the end of the simulation. By using the time of sink formation I offset the simulation time scale for each sink in order to get sink ages for each time and each sink. Before sink formation, I use the protosink (the gas particle, which becomes a sink after sink formation) position as a reference centre of the system and calculate the distances of other reservoir particles to it. Doing this, at the last time step before sink formation, gives the distribution of particles in the reservoir just before sink formation. I use this distribution to calculate cumulative mass as a function of distance to protosink. I separated the sinks into four groups according to their final masses and made a histogram of the mean values for each group (Figure 5.4). The error bars here are calculated as a logarithmic standard deviation in cumulative masses from individual sink profiles in a given group. The number of individual sink profiles in each group is $N_{<100\,\mathrm{M}_\odot} = 1471$, $N_{100\text{–}300\,\mathrm{M}_\odot} = 821$, $N_{300\text{–}1000\,\mathrm{M}_\odot} = 231$, $N_{>1000\,\mathrm{M}_\odot} = 10$. Half-mass radii are also shown for each group as solid arrows.

This diagram shows how the masses of sinks with different final masses are distributed in their reservoirs. The profiles are unresolved within 0.1 pc. The masses at 0.1 pc are almost the same, as this is the sink mass at formation, which numerically requires 70 SPH particles

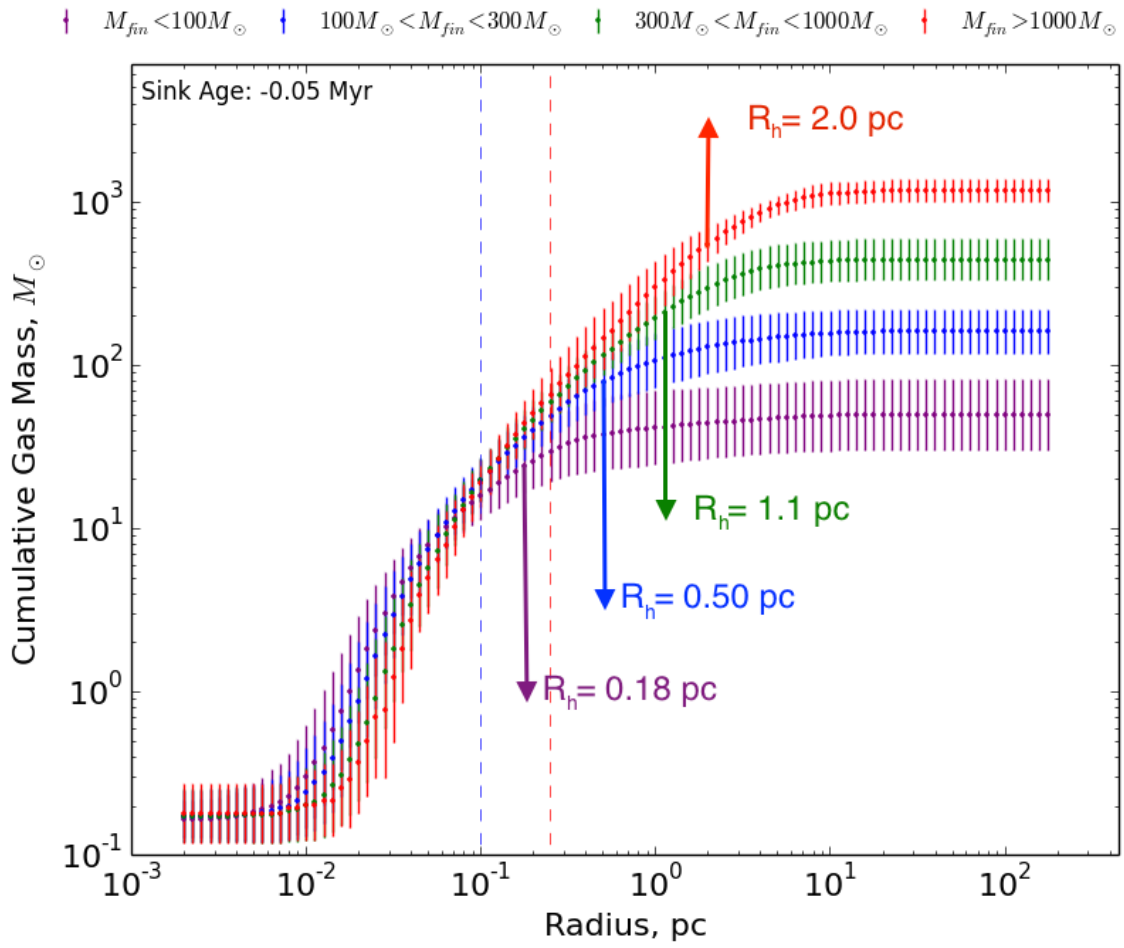

Figure 5.4: The sink mass profile is shown 0.05 Myr before sink formation. Sinks are collected from all timesteps when they are just about to form. Profiles are plotted by averaging cumulative masses in the corresponding radius bin for four different final mass subsets. The two dashed lines mark inner and outer accretion radii. Half-mass radii are shown for each subset as R_h. The figure shows that the most massive sinks gain most of their mass through accretion from scales of several parsec while lower final mass sinks gain most of their mass from sub-parsec scales.

in order to be created (as the gas particle mass is 0.156 $M_\odot$, the lowest mass sinks can be 10.9 $M_\odot$). The outer parts of the profiles show that larger final mass sinks have much more massive reservoirs over larger scales than the low final mass sinks. Low final mass sinks (<100 $M_\odot$) acquire a significant fraction of their masses during their formation, with their half-mass radius found to be 0.18 pc, which is smaller than the outer accretion radius (0.25 pc). The largest final mass sinks (>1000 $M_\odot$) contain most of their material in their reservoirs of gas particles remaining to be accreted, and as a result their half-mass radii extend up to 2 pc.

By comparing these cumulative masses to Rathborne et al. (2015) ones, shown in their top left panel of Figure 14, it can be seen that cumulative masses are much smaller in this work than in Rathborne et al. (2015). Rathborne et al. (2015) found 6×10^3 $M_\odot$ enclosed within 0.5 pc, while in Figure 5.4 the largest masses are $\sim$ 100 $M_\odot$. While in this work only those particles remaining to be accreted were used for a given sink, it could be that the larger contribution can be added from overlapping other sink reservoirs as well as from non accreted gas particles.

5.2.2 Local boundedness of star forming regions

Similarly to the method using enclosed masses, I calculate binding ratios using the gravitational, kinetic and thermal energies at each enclosing radius (Figure 5.5). The gravitational enclosed energy is calculated by directly summing over all possible pairs (N^2 computing performance). Kinetic energies are calculated using each particle velocity relative to the protosink velocity. Thermal energies are calculated by directly summing over the particles' internal energies. Finally, I obtain the binding ratio as a sum of kinetic and thermal energies divided by gravitational energy. These are again calculated for four final mass sink groups and binned into radial intervals.

Figure 5.5 shows where sinks are bound. It is clear that all sinks are bound at their accretion radii (as this is also the condition for the sink formation). Low final mass sinks are bound at smaller 1 pc radii, while higher mass sinks are bound at larger ~5 pc radii. This result shows that larger final mass sink reservoirs are dominated by self-gravity on larger scales as well.

This picture of the inner reservoir being bound and the outer unbound agrees well with Rathborne et al. (2015). The scales are also in relatively good agreement as Rathborne et al. (2015) show in their bottom right panel of Figure 14 that virial ratios are one at around 2 pc.

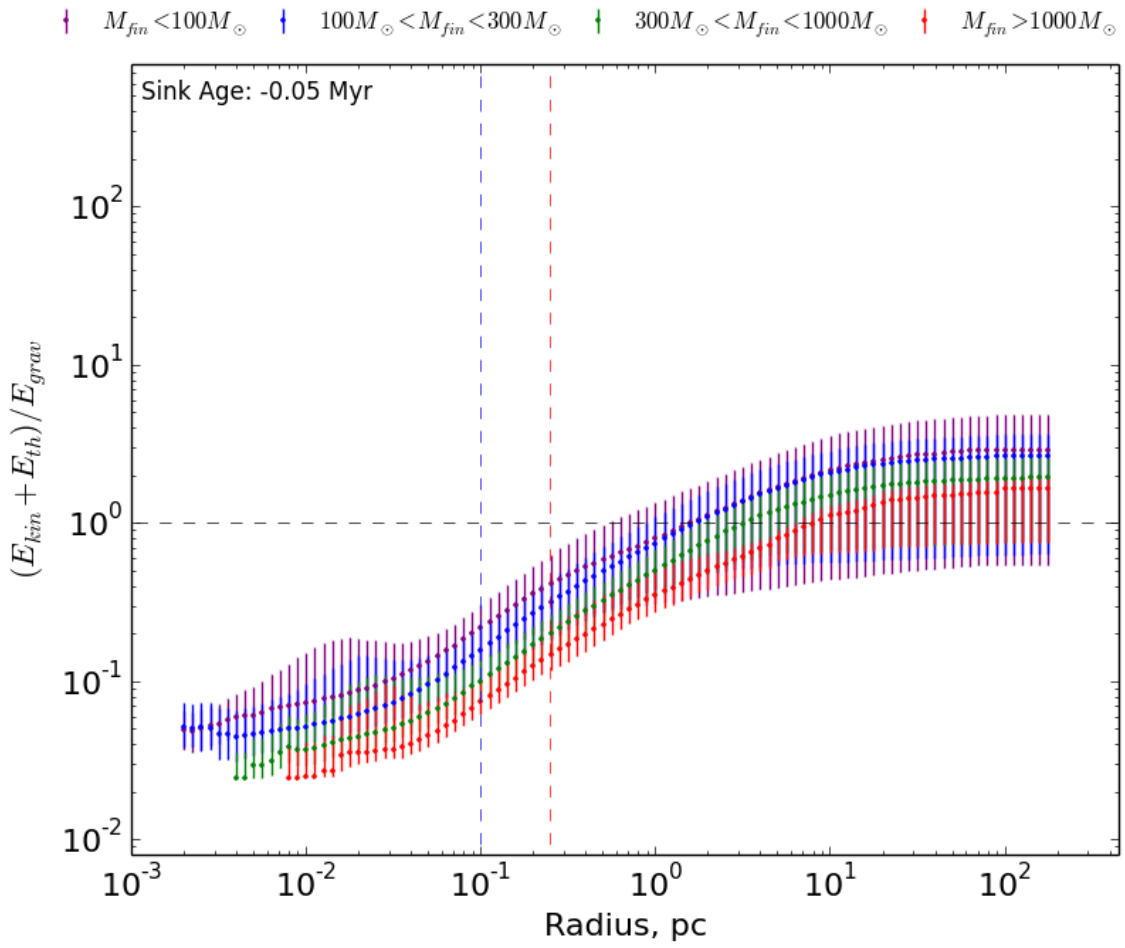

Figure 5.5: The boundedness of sink reservoirs is shown at 0.05 Myr before sink formation. The sinks were binned similarly to the process used to produce Figure 5.4. The two dashed lines mark inner and outer accretion radii. The lowest mass sinks are bound at a scale of about 1 pc, while the highest mass sinks are bound at nearly 10 pc. The outermost part of the sink reservoir is unbound at the time of sink formation, and that means the gas found there provides a smaller contribution to the cumulative sink mass (i.e. Figure 5.4).

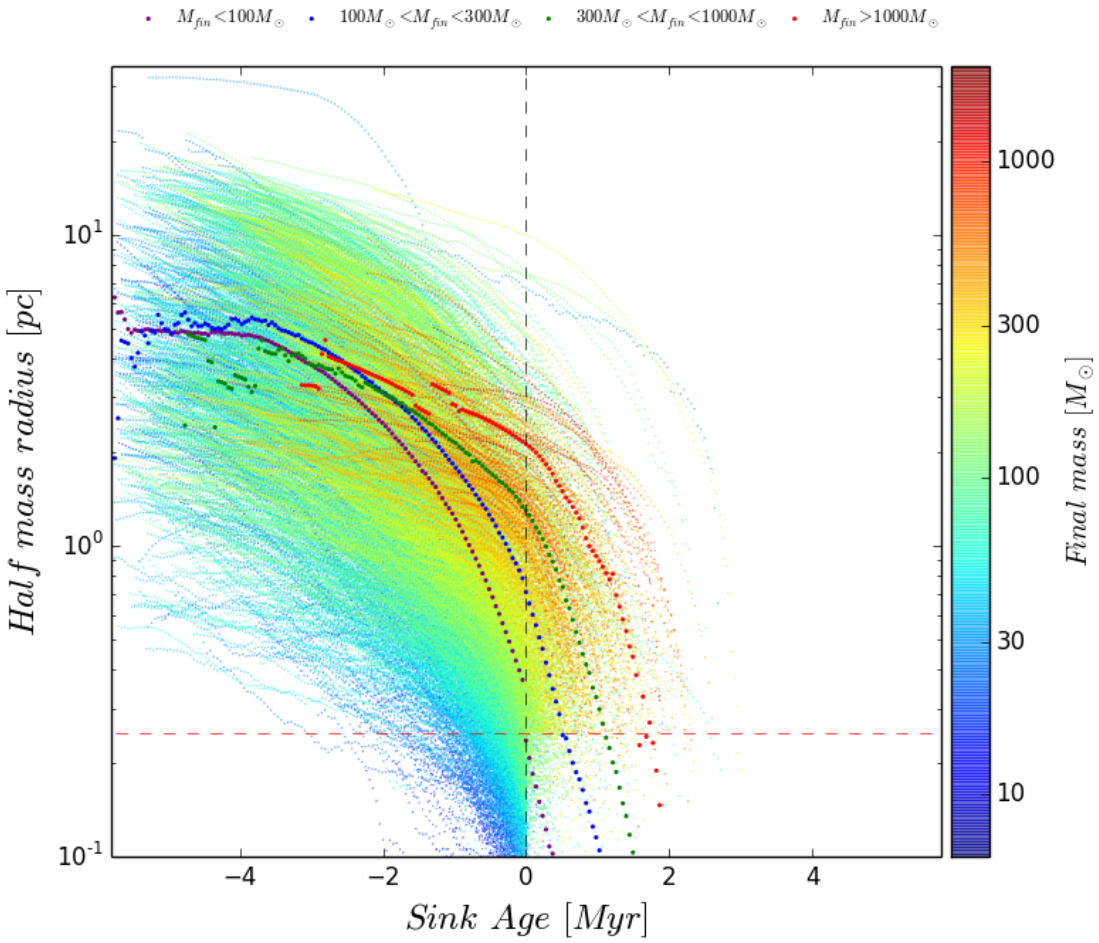

Figure 5.6: The evolution of sink half-mass radii is shown for all simulation sinks. Individual sink half-mass radii are plotted as small dots, while mean values for the four final mass sink groups are shown with larger dots. The sink tracks are also colour coded by final sink masses. Negative sink age means that the sink hasn't formed yet. The sink half-mass radii are clearly seen to decrease with age. Sinks with higher final masses also have larger half-mass radii which remain after their formation. Low mass sinks correspondingly have smaller half-mass radii which become undefined soon after sink formation.

Unlike cumulative masses, discussed in 5.2.1, the binding ratios in Figure 5.5 compare well to Rathborne et al. (2015) ones. This is because when calculating the ratio of energies for the vertical axis in Figure 5.5, the masses are cancelled out.

5.2.3 Half-mass radii

In order to define the size of the sink forming cloud, I use the 50% mass Lagrangian radius (or simply called the half-mass radius). The half-mass radius (HMR) encloses half the total mass of the sink reservoir when summing from the protosink's position outwards. I calculate the HMR at each time step for each sink and plot it in Figure 5.6 as a function of sink age. The small dots in the graph represent the HMR for individual sinks, with colour coding indicating

the final sink masses. The sinks were placed in four bins according to their final masses, and each bin's half-mass radius is shown by the large solid dots.

Figure 5.6 shows the evolution of the sizes of sink forming clouds. It is clear that all sink forming clouds are collapsing at all times. The half-mass radii at 3-4 Myr before sink formation appear to be almost independent of final sink masses. Sinks with low final masses show a faster decrease in half-mass radius during the period around 1-2 Myr before sink formation, and reach sub-parsec scales by the time the sink is formed. On the other hand, sinks with large final masses do not show a significant decrease in the half-mass radius before sink formation, but only 1-2 Myr afterwards. Also, there are not many high final mass sinks with very early histories, i.e. 3-4 Myr before sink formation. This is because it takes more time to form high mass sinks and, as a result, most of the highest mass sinks form no later than 1-2 Myr after the beginning of the simulation.

At the smallest sink ages, all sinks show $\sim$5 pc mean scale sizes, while individual cases are likely to vary between 1 and 10 pc. All half-mass radii are well-defined before sink creation. However, after sink creation the half-mass radius can be defined only if the sink mass does not exceed the remaining mass in gas particles that have yet to be accreted. This explains the empty region at 0 - 2 Myr for very small half-mass radii.

5.3 Galactic flows and gravity

It can be seen from Figures 5.2 and 5.3 that sink formation and accretion occurs mostly in the mid to high density regions. In Figure 5.5 I show that sinks are bound at 1-5 pc scales. However, this does not explain how accreted particles reach their sinks from larger scales, where sink reservoirs are unbound at the time of sink formation. In order to explain this, I calculate three different time scales which predict sink formation times for each particle. The first one is the free-fall or clump collapse time:

$$t_{\rm clump} = \sqrt{\frac{3\pi}{32G\rho}} \tag{5.1}$$

where ρ is the gas density of the SPH particles (calculated while the simulation was running). The clump collapse time accounts for the influence of the environment and shows how long it would take for gravity to collapse the clump to the point that the particles would reach

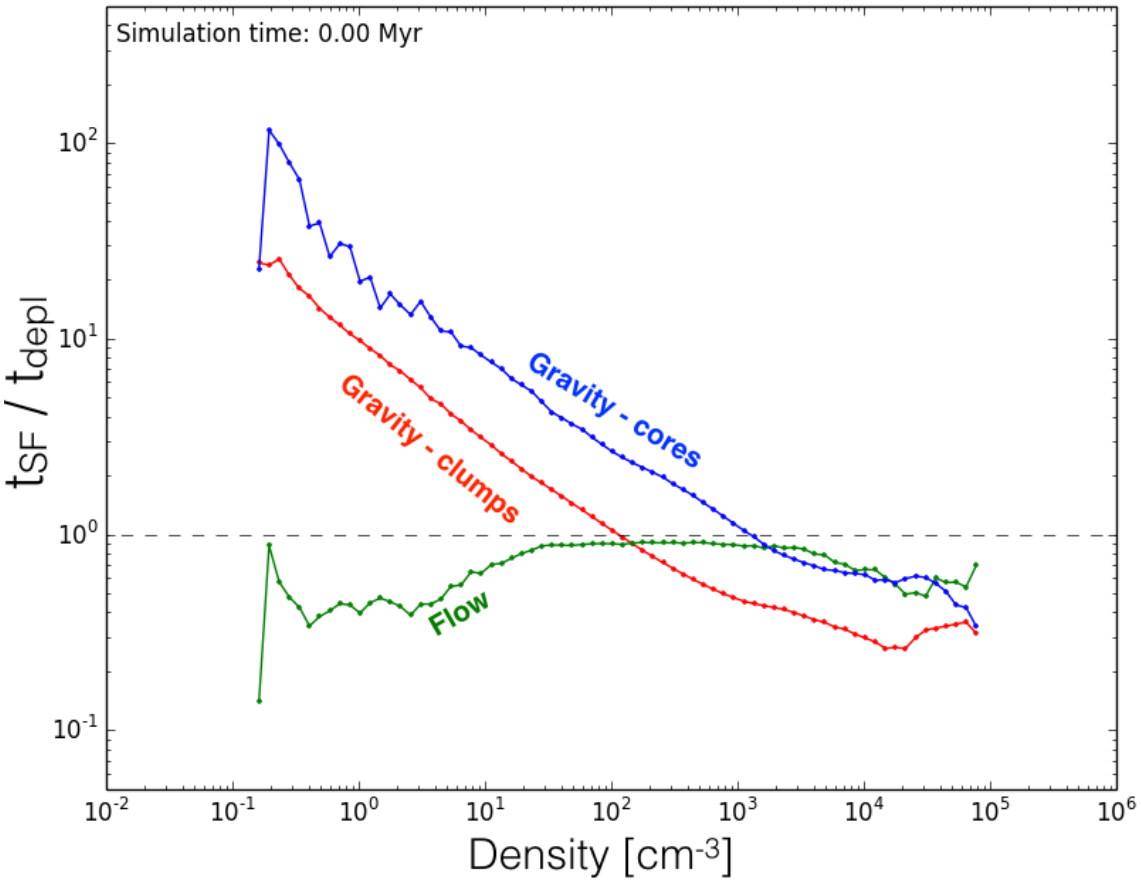

Figure 5.7: An explanation of sink formation and accretion over different scales is illustrated in this plot in terms of the depletion and sink formation time scales. The plot shows the predicted sink formation time ratio with the measured depletion time as a function of gas particle density. The figure was created using the properties at the start of the simulation of particles which were to be accreted later on. The three different methods used to calculate the sink formation time show that at high density (small scales) gravity dominates, while at low densities (large scales) it is the galactic flow alone which moves gas towards the sinks to which they will be accreted.

the sink. The second one is the core-collapse time:

$$t_{\mathrm{core}} = \sqrt{\frac{d_{\mathrm{sink}}^3}{GM_{\mathrm{sink}}}} \tag{5.2}$$

which I calculate using the distance d_{sink} between the accreted particle and the (proto) sink, and the enclosed remaining mass which is going to be accreted by that sink within that distance, d_{sink}. t_{core} shows how much time is remaining for the core collapse if the only given sink is considered. The third time scale is the flow time:

$$t_{\mathrm{flow}} = \frac{d_{\mathrm{sink}}}{v_{\mathrm{flow}}} \tag{5.3}$$

where v_{flow} is the radial velocity of the particle towards its sink. t_{flow} then is the time needed to reach the sink if the particle were to move at a constant v_{flow} the entire distance to the sink d_{sink}. The flow time accounts for the current particle velocity whose origin does not have to be gravity-based, but could instead be driven by the spiral shock.

All three times are independent predictions for the time for sink formation or accretion to occur if one or another physical process is dominating. In addition to these, I also calculate the depletion times t_{depl} for all particles in the reservoir remaining to be accreted. This is the actual time remaining in the simulation until each particle is accreted. It can be calculated by using current time (t_{current}) of the simulation and the particle accretion time (t_{acc}):

$$t_{\mathrm{depl}} = t_{\mathrm{acc}} - t_{\mathrm{current}} \tag{5.4}$$

The depletion time is positive only for particles which have not yet been accreted. The ratio between one of the three predicted star formation times and the depletion time $t_{\mathrm{SF}}/t_{\mathrm{depl}}$ shows how accurate that prediction is. If $t_{\mathrm{SF}}/t_{\mathrm{depl}} < 1$, then the actual sink formation or accretion in the simulation is happening more slowly than the model predicts. This means the model supports the driving of sink formation and accretion, but additional processes must also be taking place. On the other hand, if $t_{\mathrm{SF}}/t_{\mathrm{depl}} > 1$ then the sink formation and accretion in the simulation is happening more quickly than the model predicts, meaning that it alone cannot explain sink formation and accretion.

I calculated all three ratios and plotted them in Figure 5.7. Firstly I calculated these ratios for individual particles and then binned them according to their densities. I then calculated the mean value of the ratio for the particles in each bin. The diagram was produced using the particles at the start of the simulation (i.e. when $t_{\rm depl} = t_{\rm acc}$) as this includes the full sink mass reservoir consideration.

As is visible in the diagram, sink formation and accretion can only be explained at low densities by large scale flow. As low densities represent large scales, these low density particles have to move large distances till they reach their accretion points. Both gravity models at low densities show large $t_{\rm pred}/t_{\rm depl}$ ratios, which means that it would take longer times for these particles to reach their sinks than it actually did in the simulation. It shows that gravity alone is not sufficient to move these low density particles over large distances quickly enough to reach the sinks to which they accrete, and so large scale galactic flows are needed here.

For densities above 10^2 cm^{-3} $t_{\rm clump}/t_{\rm depl}$ becomes smaller than unity, showing that the large scale gravity within clumps at these densities becomes important. $t_{\rm clump}/t_{\rm depl}$ also becomes smaller than the flow timescale, indicating that gravity becomes the dominant process driving sink formation and accretion. At densities of several 10^3 cm^{-3} $t_{\rm core}/t_{\rm depl}$ also falls below unity, showing the gravity of individual sinks taking over. The flow model at higher densities works together with gravity as the collapse of a region induces radial velocities large enough for the flow to explain sink formation and accretion. This explains why $t_{\rm flow}/t_{\rm depl}$ is always below unity. Similarly, the gravity of individual cores brings particles to even higher density and it adds up with density support from the larger scale gravity of clumps.

5.4 Sink formation efficiencies

Now that it is clearer as to which processes drive sink formation at different densities, I assess how much and when gas contributes to sink formation. This is illustrated by the mass histogram binned by particle densities in Figure 5.8. The main set of data includes all particles which were accreted or contributed to sink formation. A further four subsets are shown, including only the particles which did so within 0.5, 1, 2 and 5 Myr of the simulation's start. The overall gas distribution is plotted as the black line.

The plot agrees well with Figure 5.3, showing that most of the gas contributing to sink formation and accretion comes from the high density tail. It also confirms that later accretion

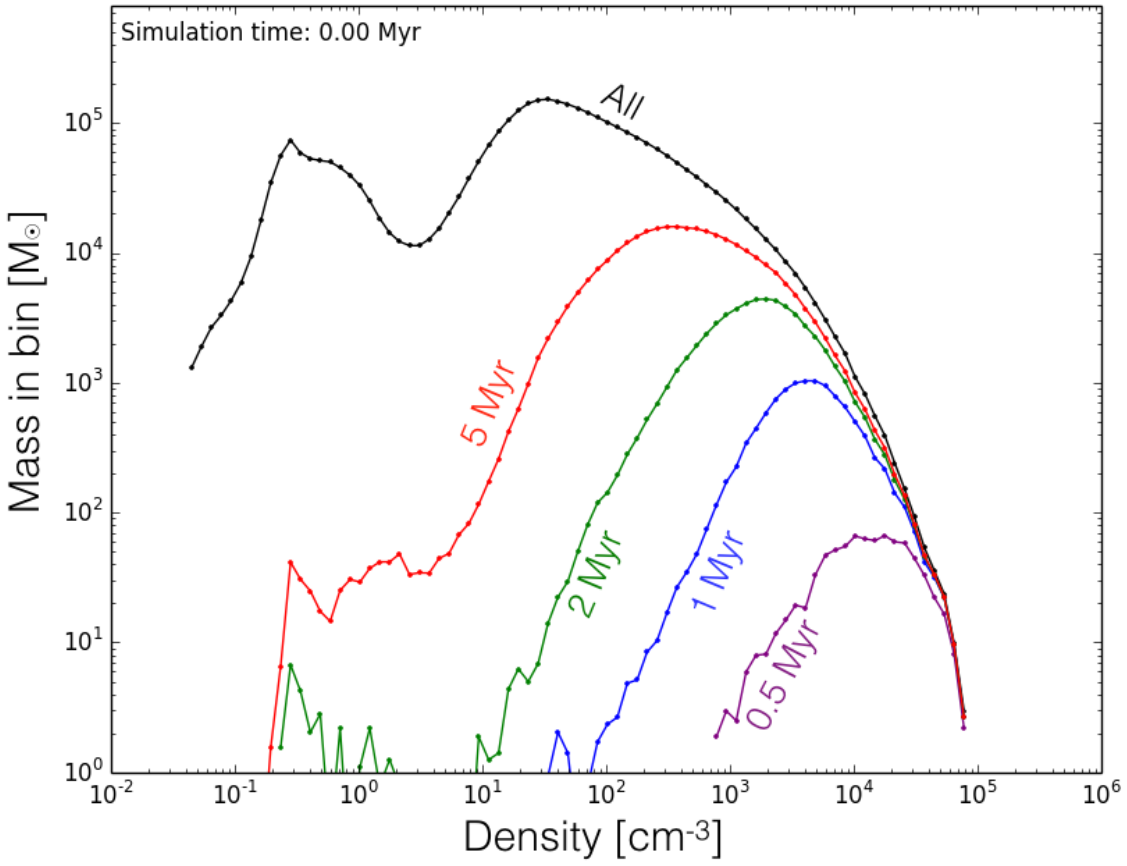

Figure 5.8: The distribution of mass with density is shown for all gas in the simulation as well as gas accreted by sinks. The accreted particles are shown after being separated into four subgroups based on their accretion times. As can be seen from the plot, particles accreted early on have high densities while those accreted later are further away and have lower densities. These particles at lower densities need to undergo collapse, or even to move with the galactic flow if at low densities, in order to reach their sinks. All four distributions of accreted gas particles have peaks shifted towards higher densities when compared with the overall density distribution.

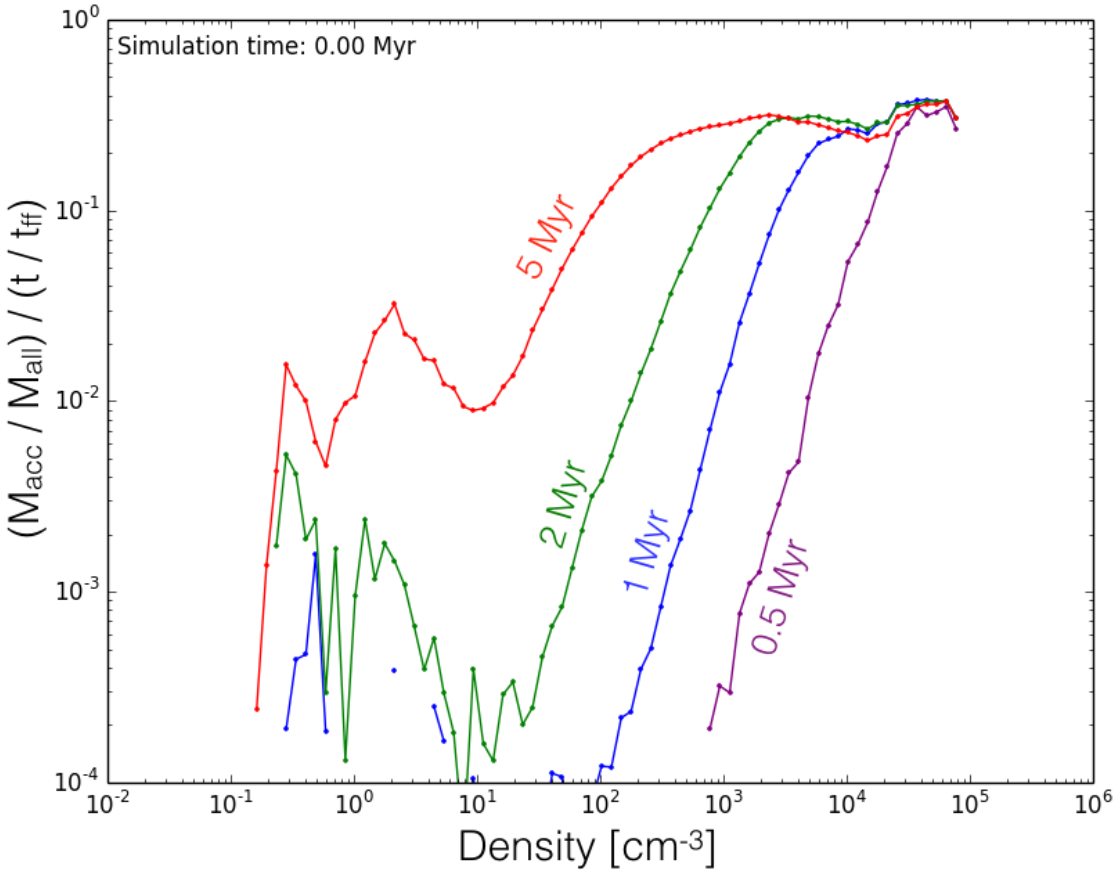

Figure 5.9: The star formation efficiency (SFE) per free-fall time for accreted gas is shown as a function of density at the start of the simulation. The accreted particles have again been subdivided by their accretion time. The SFE in high densities is large for all four subsets. However, only late accretion subsets have larger SFE in lower densities. This plot is useful in its ability to show where the SFE would drop at lower efficiencies if feedback had been included. In such a case, the late accretion would be reduced due to feedback, resulting in a lower overall SFE.

draws more and more from lower density gas. But more importantly, Figure 5.8 shows the peak values which are the densities contributing the most at the different sink formation times. Sink formation and accretion occurring early, within 0.5 Myr, mostly comes from the highest density regions at 10^4 cm^{-3}. Mid-age sink formation and accretion within 1 to 2 Myr mostly takes place in gas at lower densities of 10^3 cm^{-3}. Late sink formation and accretion beyond 5 Myr benefits mostly from lower densities of 10^2 cm^{-3} densities. As this simulation does not account for stellar feedback or supernovae, it is likely that late accretion (after 2 Myr) could be significantly reduced by feedback, yielding significantly lower final masses.

In order to calculate the actual sink formation efficiency (SFE) per free fall time, I use the ratios between accreted mass and total mass. The ratio is then divided by the time normalized to free fall time:

$$\mathrm{SFE} = \frac{M_{\mathrm{acc}}/M_{\mathrm{all}}}{t/t_{\mathrm{ff}}} \tag{5.5}$$

I calculate the SFE over the same data points from Figure 5.8 and plot them in Figure 5.9. The same four times of 0.5, 1, 2 and 5 Myr are used in order to find the sink formation efficiencies for particles accreted at different times.

It can be seen that at the high density end of Figure 5.9 the SFE is nearly flat at around 30%. The sink formation and accretion can be overestimated from the assumption that all particles entering the sink accretion radius will be accreted with 100 % efficiency. Going to lower densities, the SFE drops quite significantly between 0.5 and 2 Myr, yielding SFE at densities of 10^3 cm^{-3} as low as 2 to 3 %. As a result these estimates are larger with those of Louvet et al. (2014) who found star formation efficiencies 3 - 11 % from observations of the ridge-like structure W43-MM1 (average density $\sim 2 \times 10^4$ M$_\odot$). It is also noticeable that with time the sink formation efficiencies increased at lower densities as the particles in that environment were given the time needed to reach the sinks to which they accreted. This confirms the necessity of feedback which can reduce continuous accretion at later times. Sink formation efficiencies can also overestimate star formation efficiencies due to the minimum sink mass of 11 M$_\odot$ in Bonnell et al. (2013) simulation as the physics within the accretion radius is unresolved.

5.5 Summary

In this chapter I discussed the triggering mechanisms of star formation in spiral arm simulations. Most simulations which use idealised initial conditions, assumes that the cloud is bound and collapsing. These simulations allow the investigation of star and cluster formation, but neglect the triggering mechanism behind such assumptions. Here I used the simulations of Bonnell et al. (2013) for the investigation of triggering mechanisms as well as the details of the subsequent star formation. The triggering mechanism in this simulation is the galactic spiral shock which compresses the gas to high densities and allows self-gravity to take over in bound regions and drive collapse. While the simulation can't resolve the formation of individual stars due to the minimum sink mass of 11 M$_\odot$, the analysis is presented for individual sink formation and accretion. The analysis described in this chapter can be reused in future high resolution simulations in which sinks represent individual stars.

I have produced velocity difference maps (Figure 5.1) in order to show the strength of the spiral shock and find where it is most important. I combined this velocity map with a sink formation and accretion map (Figure 5.2), showing where the sink forming particles are located. From this it can be seen that sink formation and accretion occurs in the high density post-shock region which is compressed by the pre-shock inter-arm gas flowing in with a relative velocity of $\sim$30 km/s. Most sink formation and accretion is driven by self-gravity in the highest density regions, but the shock is responsible for raising post-shock gas to high enough densities for sink formation to start.

I have also investigated the formation of sink particles in order to find where the mass used in their assembly comes from (Figure 5.4), and also at what scales the accreted gas particles become bound (Figure 5.5). It appears that sinks with higher final masses grow through accretion from larger scales as particles become bound and collapse towards the sinks before being accreted. Less massive sinks are bound only on smaller scales and thus unable to drive a significant accretion from larger scales. Measurements of half-mass radii (Figure 5.6) show that all sink reservoirs do collapse over time. Furthermore, it was found that at all times sinks with higher final masses have larger half-mass radii than lower mass sinks.

Finally I review possible explanations for sink formation and accretion over different scales. Here I used a comparison between the measured depletion time and the predicted sink formation time as a function of density (Figure 5.7). Using three predicted sink formation times, I showed that sink formation on small scales is driven by gravity, while on large scales it is driven by the spiral shock. I also calculated sink formation efficiencies for different accretion times which shows that some additional mass could not be accreted if the feedback would start in several Myr.

6

Formation of stellar clusters

Inspection of the distribution of forming sink particles immediately reveals that they form in compact groups, which represent stellar clusters. Due to the minimum sink mass resolution of 11 $M_\odot$ in the Bonnell et al. (2013) Gravity simulation, each sink can also represent a cluster of stars. However, in such cases sinks would represent unresolved stellar clusters or widely distributed non-clustered groups. Therefore, clusters of sinks in the Bonnell et al. (2013) simulation would likely represent a clustered mode of star formation with resolved statistics, from which cluster properties will be determined in this chapter. I will treat the distributed population of sinks as that which represents distributed star formation or low mass unresolved clusters.

While it is known that stellar clusters form due to gravity, still unanswered are the key questions of where, when and how clusters form, what determines the clusters' physical properties and what influence Galactic flows have on cluster formation. In order to answer these questions, I perform an in-depth analysis on the identified clusters.

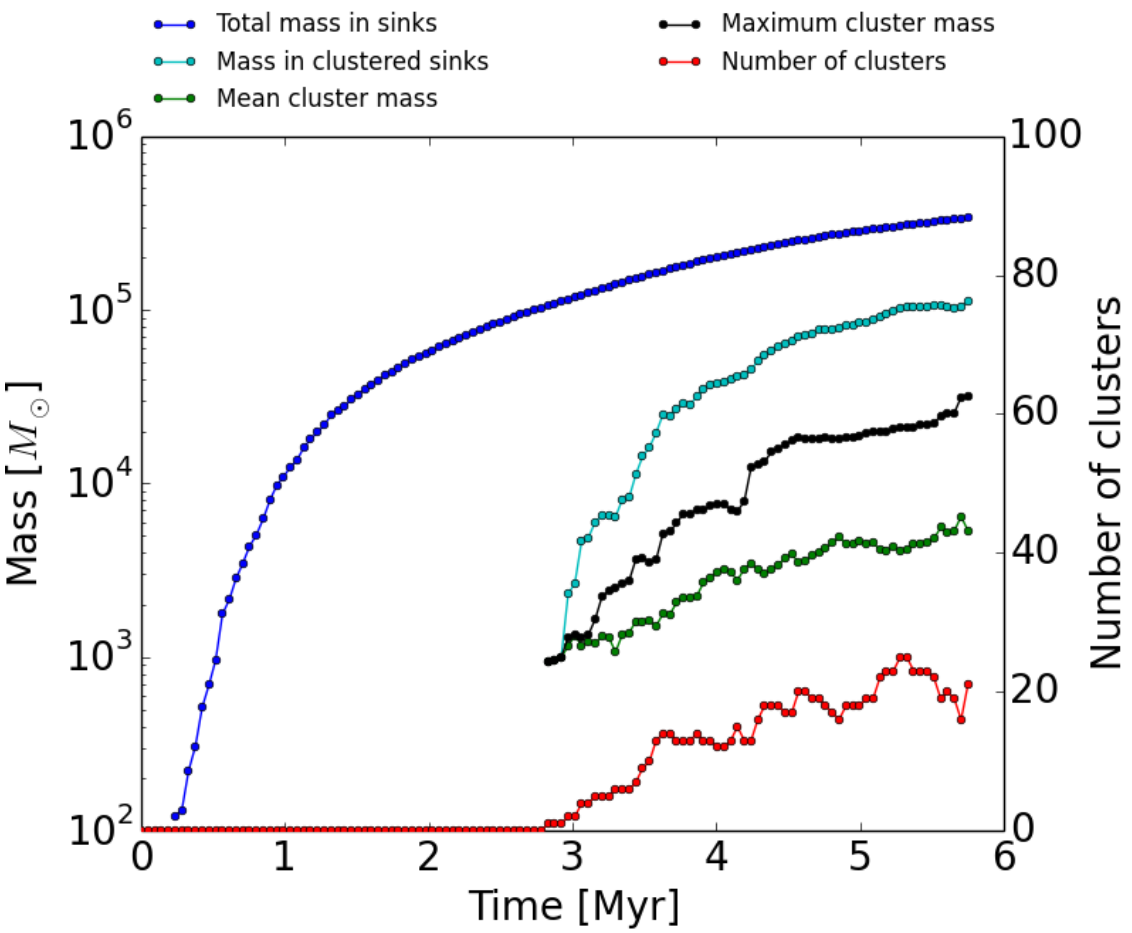

Figure 6.1: Simulation statistics over time are shown in this plot in terms of the total mass in sinks and in clusters, the mean and maximum cluster masses, and the number of clusters. The left-hand axis represents mass while the right shows the number of clusters. All properties shown here increase over the duration of the simulation, indicating continued star formation and cluster growth. Clusters only start to form at around 3 Myr, while individual sinks begin to form soon after the start of the simulation. By the simulation's end the mass in clusters contains around 20 % of the total sink mass in the simulation.

6.1 Cluster statistics

Firstly I performed a cluster search independently over all time steps of the Bonnell et al. (2013) Gravity simulation. This gives the statistics for sink and cluster numbers and masses. Figure 6.1 shows the total mass of all simulation sinks as well as the total mass in clustered sinks. I also calculated the individual cluster masses at each time step and plotted the maximum and mean masses on the same plot. Finally, the right-hand axis on this plot refers to the number of clusters at each time, plotted as a red line.

Figure 6.1 shows that the mass in sinks and in clusters continues to grow throughout the simulation. At the beginning of the simulation neither sinks nor clusters were present. The first

sinks start to form almost immediately in the highest density clouds. The total mass in sinks increases rapidly from several 100 to several 10^4 $M_\odot$ over the first million years. However, these very first sinks form as non-clustered sinks. From 1 Myr up to the end of the simulation the total mass growth in sinks continues but with a much smaller logarithmic slope such that it grows from several 10^4 to several 10^5 $M_\odot$ at the end of the simulation.

The first clusters start to form only half way through the simulation at 3 Myr. They also form from existing sinks which can be formed earlier in separate regions. At 3 Myr only 1 % of the sink mass is clustered, with a total mass in sinks of 10^5 $M_\odot$ and only 10^3 $M_\odot$ in clusters. An intensive phase of the formation of the first clusters takes place between 3 and 3.5 Myr, likely driven by the local gravitational collapse of sinks which are bound and falling into the first small clusters. During this phase, the gap between clustered and non-clustered mass narrows and $\sim$10 % of the total sink mass is in clusters at 3.5 Myr. It is also a period when the first 10 clusters are being formed.

From 3.5 Myr onwards, until the simulation's end, the fraction of the total sink mass in clusters stabilises at around 10 to 20 %. Cluster merging also occurs during this phase, with several smaller clusters coming together to form a more massive one. Merging itself does not increase the fraction of clustered mass as individual sinks are already clustered before and after merging. On the other hand, merging increases the maximum and mean cluster masses. The maximum cluster mass is increased the most rapidly, as the merger process and gas accretion is significantly stronger for the most massive clusters than for the less massive clusters. The mean mass also increases as intermediate mass clusters experience merging and the high-mass end of the cluster mass distribution rises, dragging the mean value as well. However, the total number of clusters does not increase quite as significantly as the merging of multiple clusters continues to bring it down. This is why between 4 and 5.6 Myr the number of clusters fluctuates: new clusters which have just formed increase the number, but mergers in other regions bring it down again.

Thus Figure 6.1 gives our first insight into three main stages of cluster formation: at 1 - 3 Myr individual sinks form, from 3 - 4 Myr the first seed clusters rapidly form, and from 4 - 5.6 Myr clusters grow and merge.

The number of clusters per kpc^2 is however overestimated in Bonnell et al. (2013) simulations compared to observations. Porras et al. (2003) finds that there are 17 young stellar

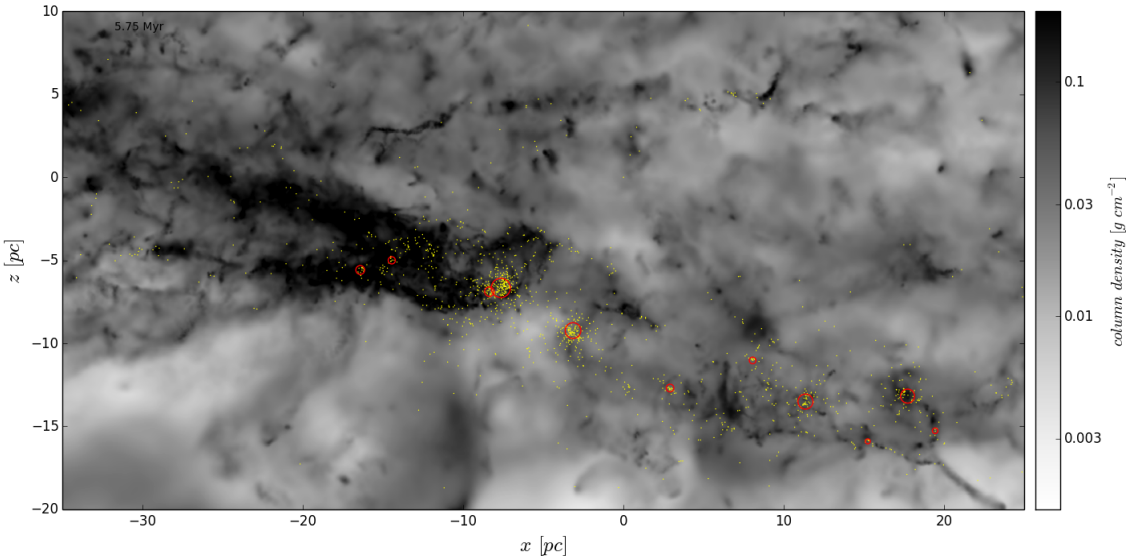

Figure 6.2: The distribution map of the gas, sinks and clusters is shown for the central star formation region at the end of the simulation. Gas is plotted as the grey scale column density map in the background of the plot. The star formation region is slightly offset from the Galactic mid-plane towards the negative z direction. Clusters do not necessarily overlay the highest density regions.

clusters (YSC) within 1 kpc around the Sun. This gives density of 5.4 YSCs per kpc^2 for the Milky Way disc. Gutermuth et al. (2009) gives 36 YSCs within 1 kpc around the Sun which translates to 11 YSCs per kpc^2. The number of clusters at the end of Bonnell et al. (2013) simulation is 20. Taking into account that the simulation is set within 0.25 kpc radius, the density of clusters in the disc would be 102 clusters per kpc^2.

The difference between simulations and observations could arise due to a number of reasons. Firstly, the number of clusters in Bonnell et al. (2013) could be too large due to the resolution as 11 $M_\odot$ is set to be the minimum sink mass and accretion could be overestimated due to large accretion radii (as gas is assumed to be accreted within accretion radii, while in reality at smaller scales some gas could escape or form accretion discs rather than directly being accreted by stars). Another reason could be that there are no stellar feedback and magnetic fields included in Bonnell et al. (2013) simulations and sink formation and accretion can be overestimated. Thirdly, Bonnell et al. (2013) select 250 pc radius region to be in the high density spiral arm segment. This means that if the empty inter-arm regions had also been included, the density of clusters per kpc^2 in the simulation would be significantly reduced.

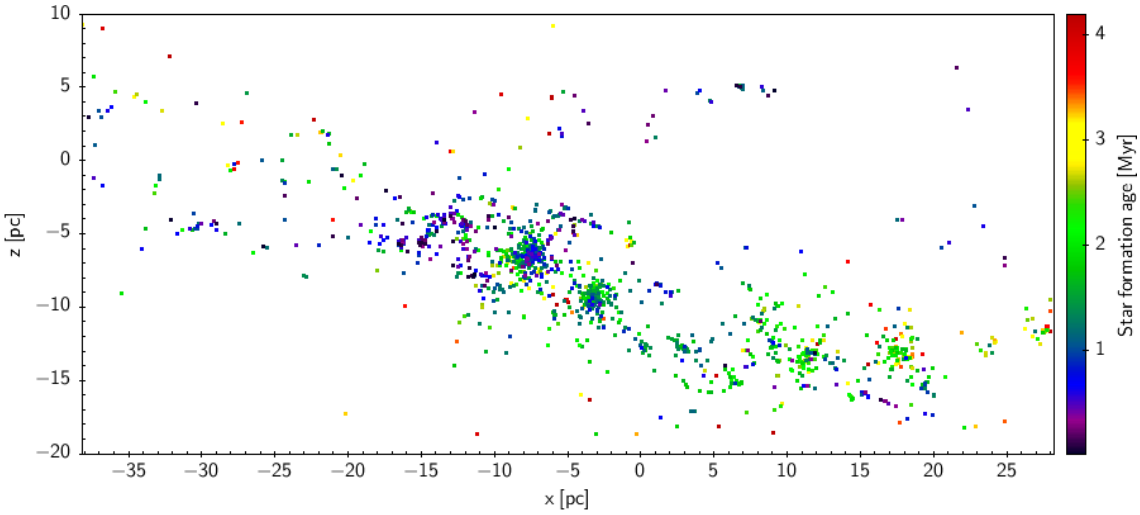

Figure 6.3: The distribution map of sinks is shown in the main star formation region at the end of the simulation. Each sink is colour coded by the star formation age, which is calculated by averaging the accretion times for the given sink's accreted gas particles in order to account not just for initial sink formation time but also later accretion. The map shows a systematic gradient in star formation ages as the sinks are older in the right portion of the map when compared to those on the left. This gradient came about as the spiral shock approached and triggered star formation in the right part earlier than in the left.

6.2 Cluster forming locations

The first questions asked about clusters are how they are distributed in space, where the cluster forming regions are found, and how they correlate with the distribution of gas. In order to answer these questions, position - position maps are the first source of information. I use two maps on the intermediate-size scale in order to see individual sinks in each cluster as well as the overall distribution of clusters and sinks, and their positions in the spiral arm. These are illustrated in Figures 6.2 and 6.3.

Gas column density is plotted as a gray-scale background in the Figure 6.2. Sinks are plotted on top as yellow dots and clusters are shown as open circles positioned at their centres of mass. Figure 6.3 shows only the sink particles, but they have been colour coded by mean star formation age, derived by averaging the accretion times of all particles accreted to each given sink. Both plots are made for the final timestep of the simulation.

The use of an edge-on projection (x-z) allows us to clearly see the structure of the region in the galactic plane. Interestingly, clouds and recently formed clusters do not necessarily lie exactly in the galaxy's midplane. Clouds appear more concentrated near the mid-plane at the left-hand side of the diagram, but moving towards larger x positions the clouds and clusters appear to tilt down to 10 - 15 pc below the mid-plane.

It is also interesting to note that at small x (the left-hand side of Figure 6.2) there is a small number of sinks and no clusters, but high density gas clouds (> 0.1 g cm^{-2}) are present. At large x (on the right-hand side) there is conversely no high density gas, but a larger number of sinks and clusters are present. Figure 6.3 also shows a stellar age gradient from left to right, with sinks on the right-hand side older than those on the left. These features tell the story of how the spiral shock passed through the region. As the shock approaches with a 10-20 degree pitch angle (estimated by eye), it starts compressing the first clouds at the positions with highest values of the x coordinate. The first sinks and clusters form there at simulation times of 2-3 Myr. The intersection area, where clouds are compressed, moves with the flow towards the left. After the shock passes the regions on the right, a large amount of gas there is depleted into sinks and clusters, while the remaining post-shock gas at the same time starts to slowly expand. It is likely that the combination of depletion and the post-shock expansion effect leaves just formed clusters in low density regions. As the wave of triggered star formation moves leftwards, it leaves behind it the gradient in stellar ages (Figure 6.3). At the end of the simulation (5.6 Myr), the triggering region is located at $x \sim -10$ pc, slightly left of the most massive cluster in the centre of Figure 6.2. This is where star formation should just be starting – a large number of very young sinks with ages below 0.5 Myr are present and likely to form the next massive cluster at $x \sim -15$ pc.

Five to six clusters visible in the middle-right of the diagram appear to be separated by characteristic gaps between the cluster centres of $\sim$10 pc in 3D space. This phenomenon could arise because of the ridge-like geometry of the main star forming region and the passage of the shock. Sinks starts to form in the ridge, following the locations of the highest density gas, created by the shock. As the ridge is not uniform, seed sub-clusters appear in the highest density clumps. In the 4th chapter, I show that most massive sinks are bound on scales of up to several pc, while the clusters are likely to be bound on even larger scales of up to 5-10 pc based on cluster reservoir sizes, which I discuss later in this chapter. As a result, this creates cluster forming "basins", where the combined material of sinks and gas is more bound to a corresponding cluster than to any other and flows toward the centre. This gives possible cluster forming reservoir sizes of up to 5-10 pc and is likely to form gaps between the clusters with characteristic sizes of $\sim$10 pc.

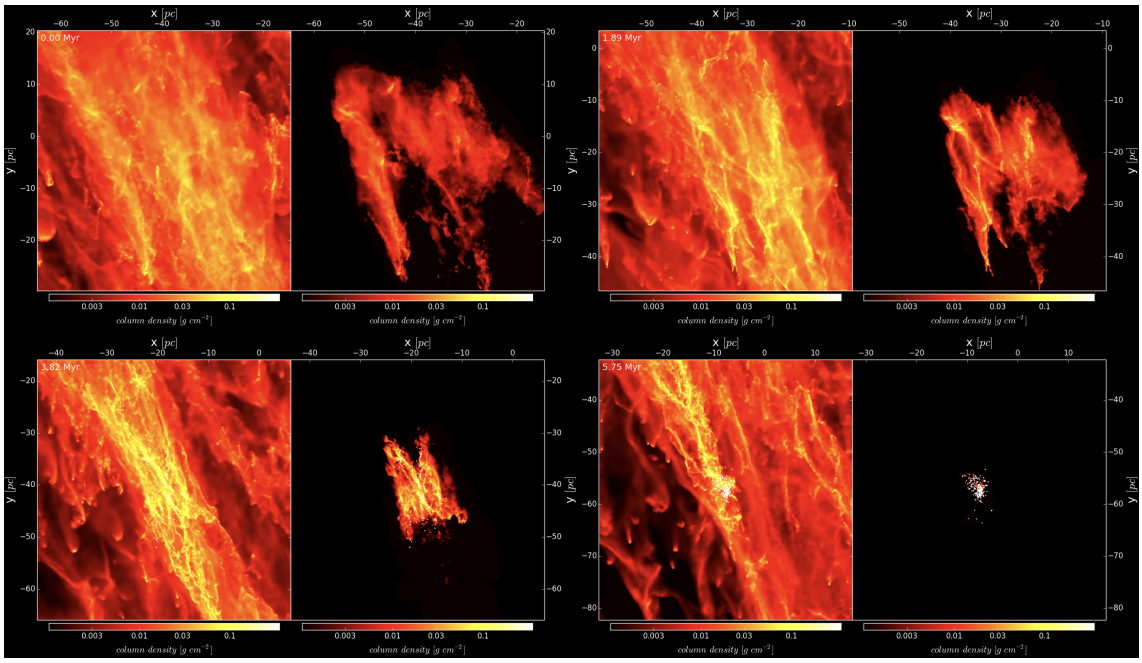

Figure 6.4: Evolution maps are shown for the most massive cluster in the simulation. Four panels represent maps of the region at four different times. The left sub-panels show column densities from all particles in the region while right-hand sub-panels show the density only from particles to be accreted to the cluster. Cluster sinks are plotted as white dots. The diagram shows that the fragmented cloud collapses globally at all times, resulting in the formation of the most massive cluster.

6.3 Spatial evolution of cluster forming clouds

Now that clusters have been identified in the simulation, I choose one in particular and describe in detail the evolution of the cloud from which it formed. Figure 6.4 shows a 50 x 50 pc size region, centred on the centre of mass of the most massive final cluster formed during the 5.6 Myr simulation time (34000 $M_\odot$). The evolution is represented in 4 different panels, showing different evolutionary stages of the cluster forming cloud. The initial conditions are shown at the top left, while the final timestep is at the bottom right. Each of the four panels has two sub-panels, on the left showing the column density as calculated using all gas particles and on the right using only those particles accreted to the 34000 $M_\odot$ cluster. As all four panels are centred on the cluster's centre of mass, the cluster forming cloud is followed during its collapse. Sinks which end up as members of the cluster (and not other sinks) are plotted in all panels over all timesteps.

The plot shows the collapse and fragmentation of the cluster forming region. What is unique about Figure 6.4 is that the cloud has been evolving along with its environment, and the Lagrangian nature of the particles allows us to actually trace which gas contributes to the formation of the cluster and which does not. The evolution seen in the left-hand panels shows

the propagation of the spiral shock and the compression of the cluster forming region. As the shock approaches from the bottom side of the diagram, it compresses the entire ridge seen lying across the plot from top left to bottom right. It follows that the ridge reaches higher densities as it evolves, leading to the global gravitational collapse of the cluster-forming cloud as seen in the right-hand panels. The cloud also breaks into several ridge-like fragments, which start to collapse locally faster than globally, creating sub-clusters. Following the global collapse of the region these sub-clusters merge into a single cluster. Initially there are no sinks - the first ones start to form in this region at around 2 Myr (the top right panel of Figure 6.4). In the third panel (bottom left) sink formation takes place in the "X" shaped ridge, which finally collapses into a several pc size cluster. The cloud's overall size during its collapse drops from $\sim$30 pc to $\sim$5 pc, meaning that it shrinks by a factor of 5-10. So, the evolution clearly shows the gravitational collapse of the region and the distribution of material at each evolutionary stage, but the internal structure of the cloud keeps changing and rearranging all the time during the collapse. This raises an open question about how challenging it could be for observations to find primordial cluster forming clouds (and also to obtain initial conditions), which are embedded in the environment and blend together along the line of sight with other clouds which do not contribute to the formation of the cluster. Another key problem is the difficulty of identifying which stage these natal cluster forming clouds are actually at. How much mass is nearby in order to support the cluster formation? At what point is it bound? And how massive will the final cluster be?

6.4 Initial distribution of cluster forming clouds

To further discuss the question as to where the cluster forming clouds are located and where the material to form the clusters comes from, I traced the gas particles accreted to all clusters and plotted their initial positions in Figure 6.5. The colours show the final masses of the corresponding clusters to which these clouds contribute. As a result, Figure 6.5 shows how each of the cluster forming clouds appeared in the initial conditions relative to the environment and neighbouring cluster forming clouds.

Figure 6.5 shows that the most massive clusters form in the middle of the main star formation ridge, following the high density regions in the spiral arms. Several isolated lower mass clusters also form outside the main region. More massive clusters also have physically larger reservoirs. As the flow approaches from the bottom of the diagram, visible streams of lower

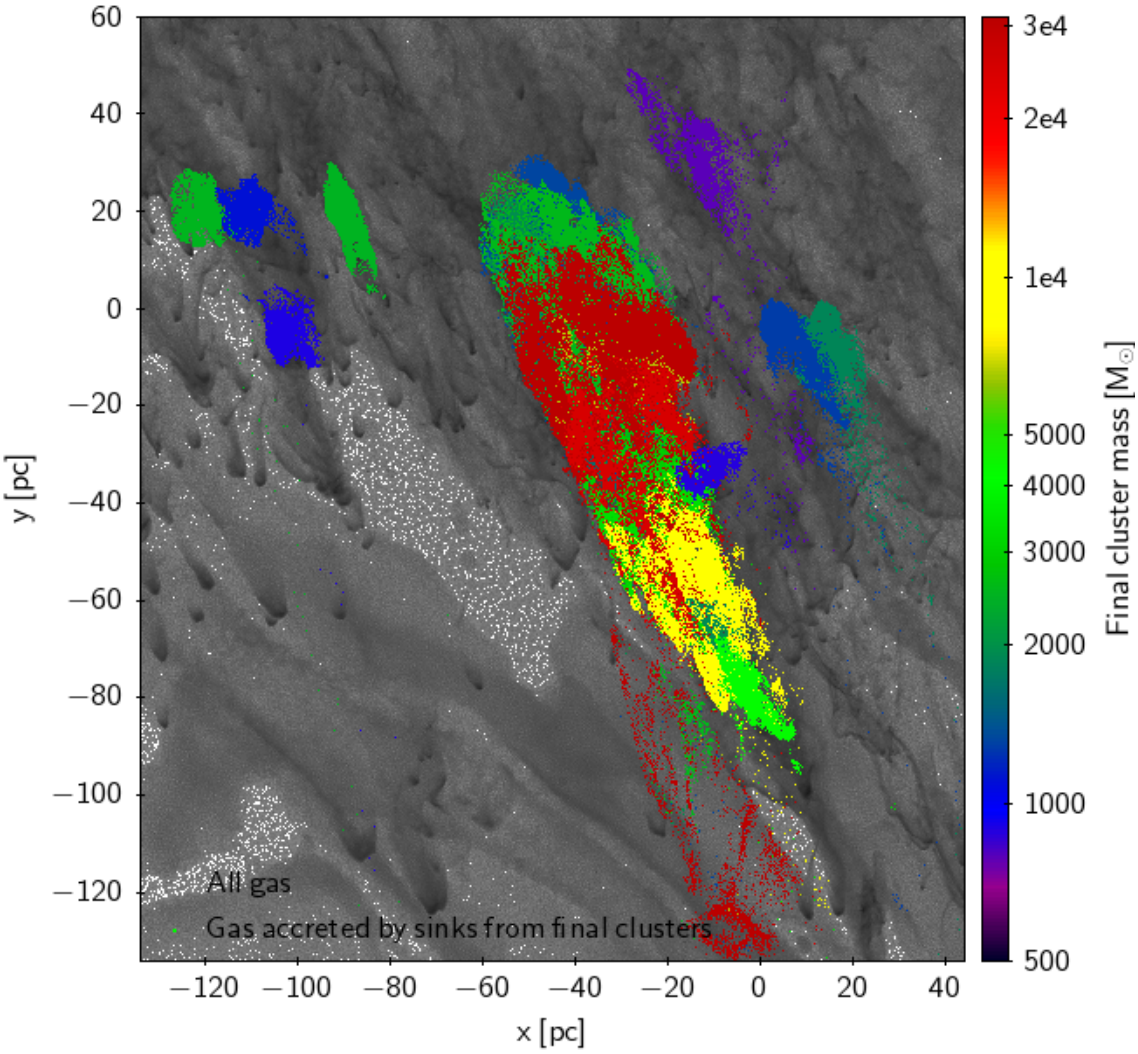

Figure 6.5: The map of the initial conditions is shown for the cluster forming regions. Gas particles contributing to the formation of clusters are colour coded by the final cluster mass, while the grey points plotted below show the positions of all particles whether or not they were accreted. White areas are transparent lowest density regions, where gaps between gas particles are visible. The map shows that cluster forming clouds are distributed over several 10 pc scales. Clusters with higher final masses tend to have larger physical sizes of their reservoirs. The main region contains several cluster forming clouds, but the boundaries between the clouds are sharp.

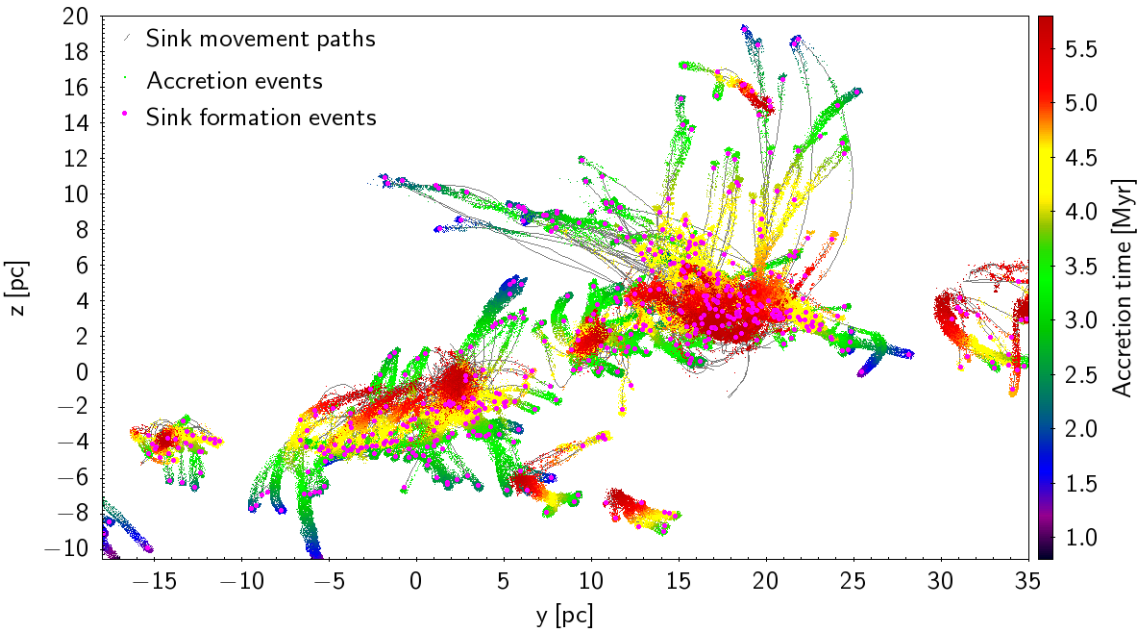

Figure 6.6: The evolution map is shown for the formation of the two most massive clusters. The positions of accreted particles are shown with small dots colour coded by accretion time. Purple dots show the position of sink formation, while grey lines show their later movement paths. Several subclusters merge before the final cluster is formed. Individual sinks form several pc away from the cluster centre and later assemble to form a single cluster.

density particles enter the main star forming region. The boundaries of cluster forming basins intersect several clouds in the main region, but do not intersect for isolated clusters, forming outside of the main region. Even if the boundaries of different clusters overlap, reservoirs are well defined in the initial conditions. This means that the majority of particles in a given reservoir could be more bound to their own cluster than to any other long before the cluster actually forms. On the other hand, some particles (like the ones in the low density pre-shock stream) are unlikely to be bound to the cluster so early but become bound later when, on moving through the shock, they lose a significant amount of relative kinetic energy to the cluster. This gas can not be detected by the observer, as the observer does not know how such gas will interact with the environment while moving towards the cluster. This brings another question - how do accreted particles move along their paths during the process of cluster formation and where are the accreted particles being accreted?

6.5 Cluster star formation and accretion history

In order to answer how star forming material moves during cluster formation, I use the information of particles at their accretion times. Figure 6.6 shows the spatial distribution of star formation and accretion over time. Positions are set relative to the centre of mass of the ten

clusters with the highest final masses. This centre of mass is a good estimation of the centre of the main star forming region. It also traces well the relative velocities between the clusters and allows us to map the dynamics for not just one cluster but the entire region. Coloured particles in Figure 6.6 are gas particles accreted by the cluster forming sinks, each one plotted at its position relative to the centre of mass when it was accreted, and colour coded by the time of accretion. The movement paths of the sinks are represented by grey lines. Finally, solid purple dots show the locations of sink formation.

Figure 6.6 shows cluster formation in unprecedented levels of detail at both large and small scales. The most massive cluster of 34000 $M_{\odot}$ is visible slightly right from the centre of the diagram, while the second one (25000 $M_{\odot}$) appears to the left and down from the first cluster. During the early stages they form in filamentary structures, especially for the second cluster where most of the sinks formed between y=-5 pc and y=5 pc at z=-4 pc. Finally the filaments themselves appear to collapse with sinks flowing down the filament till they reach the cluster centre. Most of the sinks start to group early on by forming small local clusters which eventually merge together into the final cluster. This shows the merging of clusters to be an important and commonly-occurring process during cluster formation and growth. The first sinks form as far as 15-20 pc away when measuring from one side to another and come into a compact 2-5 pc cluster. The fact that cluster stars start to form in separate spatial regions could result in a large variety of their physical properties, such as large stellar age spreads.

Independently of the size scales, most of the material appears always to flow towards the centre of the corresponding cluster. The boundary between the first and second clusters appears also to be clearly defined. Finally, clusters don't just collapse, but also move relative to one another. Several smaller clusters, which are not part of the two most massive clusters also appear in the field, but their movements may be affected by the presence of the two most massive clusters.

6.6 Evolution of cluster physical properties

The spatial distribution of sinks and clusters are the first steps to understanding the physics and evolution of the region. However, we still need the physical properties of the clusters in order to obtain quantifiable answers to the questions asked previously. In this section, I describe the physical properties of the clusters such as their masses, sizes, densities, angular

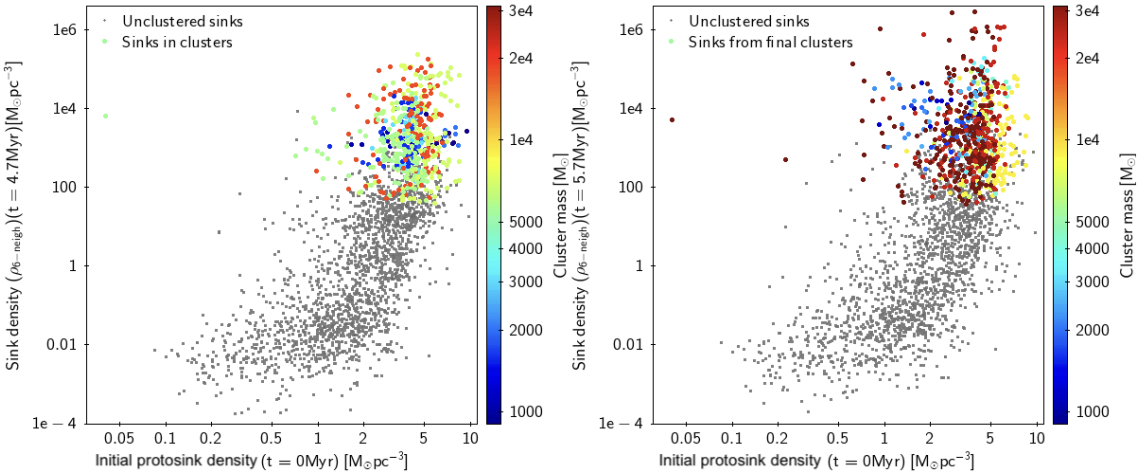

Figure 6.7: The sink densities are compared with the initial densities of the protosinks. The comparison is shown for two sink densities - at 4.7 and 5.7 Myr. Grey dots show non-clustered sinks while coloured dots show sinks coloured by the cluster mass to which they belong at the corresponding time. The plot shows a tendency for sinks with high final densities to form from protosinks with high initial densities. Sinks in clusters are found at the highest initial and final densities. accreted particles with high initial densities are more likely to contribute to clusters while lower density particles are more likely to contribute to isolated sinks.

momentum and more.

6.6.1 Mass density

The mass density is one of the most fundamental physical properties of a cluster. This can be measured for both stars and gas. The most important, mass densities could be traced by observations. The stellar density in clusters is usually defined as how much mass is packed into a cubic pc. The density can also be local or global, with a local density being a property of a particular region, while the global density is averaged over larger scales such as the whole cluster. In order to measure the mass density for each sink in a cluster, I use the distances to its neighbours. What defines the neighbourhood must be carefully chosen, as the closest neighbours give the local density, while the more distant neighbours give the global density. The closest neighbour may also be a binary companion. I used the fifth, sixth and seventh closest neighbour mean distances to derive each sink's density:

$$\rho_i = \frac{1}{3} \sum_{j=5,6,7} \frac{3(m_i + m_j)}{4\pi R_{ij}^3} \tag{6.1}$$

Here ρ_i is the density calculated at the sink in question i. j are sink's i neighbours. m_i and m_j are masses of sinks i and j. And R_{ij} is the distance between sinks i and j.

The usage of fifth, sixth and seventh neighbours gives meaningful statistics as the density is derived from the cluster scale rather than from binaries. Averaging over three neighbour values allows us to avoid picking particular neighbours which can be at the corresponding distance by accident and would not give smooth densities.

In Figure 6.7 I plot the final sink densities against the initial (i.e. start of simulation) protosink densities. During the evolution, all sinks undergo a collapse phase during which the density increases. This means that the plot shows how the density of individual sinks has changed during the simulation. Unclustered sinks in Figure 6.7 are plotted as grey points, while sinks in clusters are colour coded by their corresponding cluster mass. The two panels show the sink densities as calculated at two different times, 4.7 and 5.7 Myr.

The figure clearly shows that clustered sinks have high stellar densities above 100 $M_{\odot}pc^{-3}$. The majority of sinks in these clusters also have high initial gas densities, meaning that clustered sinks form mostly from initially high density environments. This could be because in initially high density clouds global gravitational collapse is significant, leading to more efficient star formation and cluster assembly. More isolated cloudlets seem to collapse only locally, resulting in isolated star formation. Figure 6.7 also shows a smooth transition between clustered and isolated star formation modes.

There is also visible a small population of sinks in Figure 6.7 with initial protosink densities of 1 $M_{\odot}$ pc^{-3} and high final densities of 10^4 $M_{\odot}$ pc^{-3} at 5.7 Myr. These sinks come to clusters from lower initial density regions. The origin of these sinks could be related with the infall from isolated sinks (formed in lower density regions) into clusters.

The scattering in the Figure 6.7 can be related with the differences between definitions of initial protosink density and the sink density at a given time. The protosink density was based on SPH densities obtained from 70 neighbours (note that protosink is a gas particle at the beginning of the simulation), while the sink densities are dependent on their fifth, sixth and seventh neighbour sinks. As a result, more detailed comparison between different density definitions is needed in order to better understand mapping relations between initial and final densities in sink forming regions.

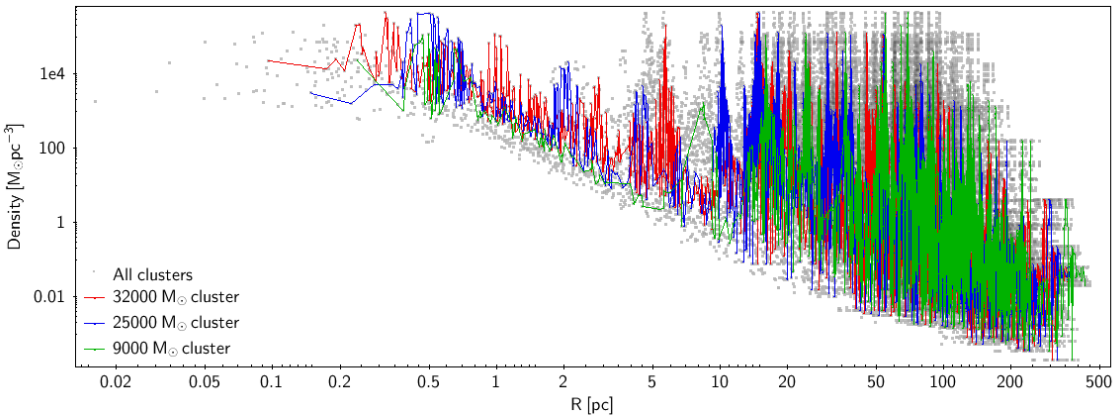

Figure 6.8: The radial density profile is shown for the three most massive clusters in the simulation. The profiles are also shown for other lower mass clusters as grey dots in the background. The diagram shows that local sink densities systematically decrease within 2 -5 pc. At larger distances, some sinks have even lower densities, while others are much higher. The high density spikes around 5 - 10 pc are due to the presence of other clusters. The internal part of the profile shows that local sink densities decrease when moving outwards according to a power law which approximately follows $\rho \sim R^{-3}$.

6.6.2 Cluster density profile

The radial density profile of a cluster shows how sinks are distributed at different radii from the cluster centre of mass. The density would normally be expected to be highest in the centre and then drop towards the outskirts. However, the uneven distribution of sinks in the cluster will produce variations in the profile.

Figure 6.8 shows the radial profile of local sink density for all clusters at the end of the simulation. The profiles are plotted not just for given cluster sinks but also for all the sinks in the simulation. The profiles of the three most massive clusters are plotted on top in colour.

As can be seen from Figure 6.8 these profiles extend from 0.1 pc to nearly 400 pc. At small radii the local sink densities are as high as 10^4 - 10^5 $M_\odot pc^{-3}$ as sinks here are in the central part of the cluster. At larger radii, the minimum value drops even below 0.01 $M_\odot pc^{-3}$ as these sinks can be the most isolated ones, far outside the main star forming region. Fluctuations in density are also visible, and are smallest at small radii. This is because at the smallest radii only each cluster's own sinks will be included. Also, as the next most distant sink used to calculate the profile could be located in any direction on the sky completely independently from the previous sink, the environment could also be different and so give a different local density. This is what brings small fluctuations. At around 5 pc the fluctuations appear to become much larger. This is because the profile extends not just for the cluster's own sinks but for all other sinks in the simulation. So profiles beyond 5 pc start to account for sinks from other clusters

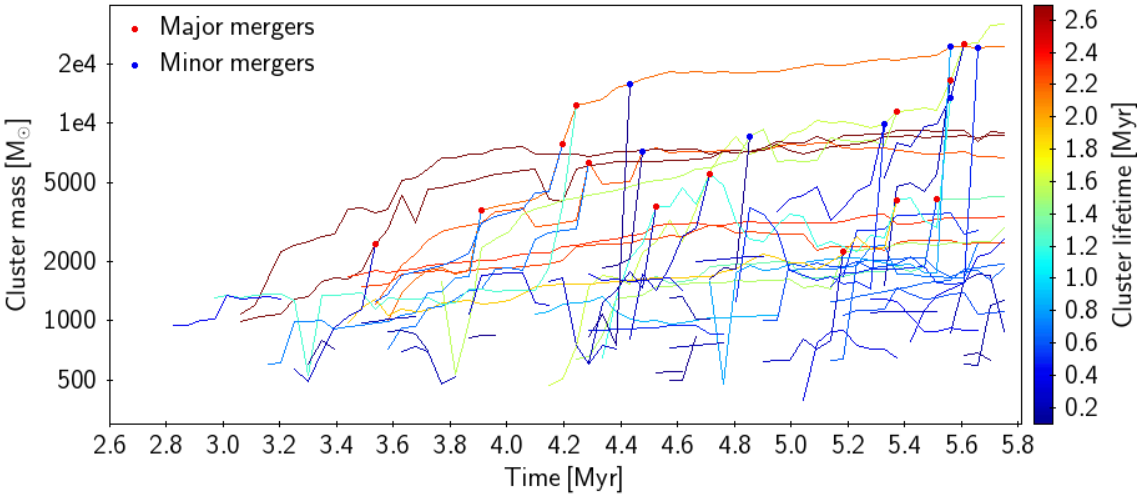

Figure 6.9: The cluster mass merger tree is shown as a function of time. Clusters are traced over time and connected with lines between timesteps. Each line is colour coded by the cluster lifetime, which is measured as the length of the line through all timesteps. When clusters merge, their tracks in this diagram are combined into one and the merging point is shown as a solid dot in the diagram. Major mergers (above 30 %) are shown as red dots while minor mergers are blue dots. The plot shows that the most massive clusters are likely to gain their mass from merging while the least massive clusters do not merge. It can be seen that clusters with a greater mass have longer lifetimes, while the least massive clusters are transient structures and only survive up to 1 Myr. These low mass clusters have low numbers of sinks (i.e. around six) and are treated as dissolved if they no longer satisfy the condition that they contain a minimum of six sinks.

at this distance. It is possible that another cluster is located on one side from the cluster being measured, while on the opposite side there is only a diffuse medium. In such a case, a sink found in the cluster would provide a high density, while one in the diffuse medium would give a much lower value. This produces the large fluctuations in the density profile visible at radii larger than 5 pc.

6.6.3 Mass merger tree

The simplest physical property of a cluster is its mass which is simply the sum of all its members' masses. However, finding the cluster mass over time is not so straightforward. Firstly, cluster mass changes due to sink formation and accretion onto the member sinks. This means the cluster mass grows if accretion of gas particles takes place. Secondly, the motion of sinks means that sinks might physically leave the cluster and no longer be counted as members. In that case, their mass would not contribute towards the cluster mass at this particular time step, until the sink re-enters the cluster again. This can lead to fluctuations of the cluster mass over time. Some sinks which are ejected by binary encounters leave the cluster and never come back – in this case, the cluster mass is reduced. Another process is cluster merging - this requires interaction between at least two clusters. When two clusters merge, their mass is

summed together. The time when merging occurs is dependent on the cluster definition, but at its simplest it is the point when one cluster is identified rather than two. A cluster can also be treated as dissolved if the definition no longer identifies a group of sinks as belonging to the cluster (this could happen for example if there are six sinks in the cluster and one of them moves away).

In Figure 6.9 I plot a mass merger tree diagram over all clusters in the simulation at all time steps. The diagram draws a line for the same cluster over multiple time steps. Two lines join to one if a cluster is merged and the solid dot is placed at this point. Red dots show major merger events (the child cluster's mass is more than 30 % of the parent's) while blue dots show minor mergers (the child's mass is below 30 % of the parent's). The colours of the lines represent cluster lifetimes. During merging events, the parent cluster (the merging cluster with larger mass) is identified as the same cluster before and after the merger. So the cluster lifetime is traced along the main trunk of the merger tree, always following the parent branch.

The tracing of clusters over multiple time steps is shown in impressive detail in Figure 6.9, providing us with information on how they evolved throughout their histories. At the end of the simulation, there are 2 clusters above 20000 $M_\odot$, 3 clusters between 5000 and 10000 $M_\odot$ and about 10 lower mass clusters below 5000 $M_\odot$. At the earlier times, most massive final clusters appear to have lower masses. More massive clusters also have longer lifetimes and richer merging histories. They formed at a simulation time of 3 Myr and survived for a further 2.7 Myr through two to five merger events as well as experiencing further accretion and star formation. On the contrary, lower mass clusters have shorter lifetimes. They end either in dissolution or by merging with larger clusters. Low mass clusters form continuously through the simulation – some may be re-forming from the remnants of previously dissolved clusters if the number of member sinks falls below six before rising to that number again as they leave and later return.

The minimum cluster mass is allowed to be 66 $M_\odot$ if all six sinks have a lowest mass of 11 $M_\odot$. However, this is not seen in Figure 6.9 as the lowest mass clusters are around 500 $M_\odot$. This could be due to the difficulty of producing such low mass clusters. It would be necessary that sinks would have formed and not experienced any further accretion. Moreover, six sinks would need to assemble in the compact region to form a cluster without accretion. Due to this difficulty lowest mass clusters formed in the simulation are around 500 $M_\odot$.

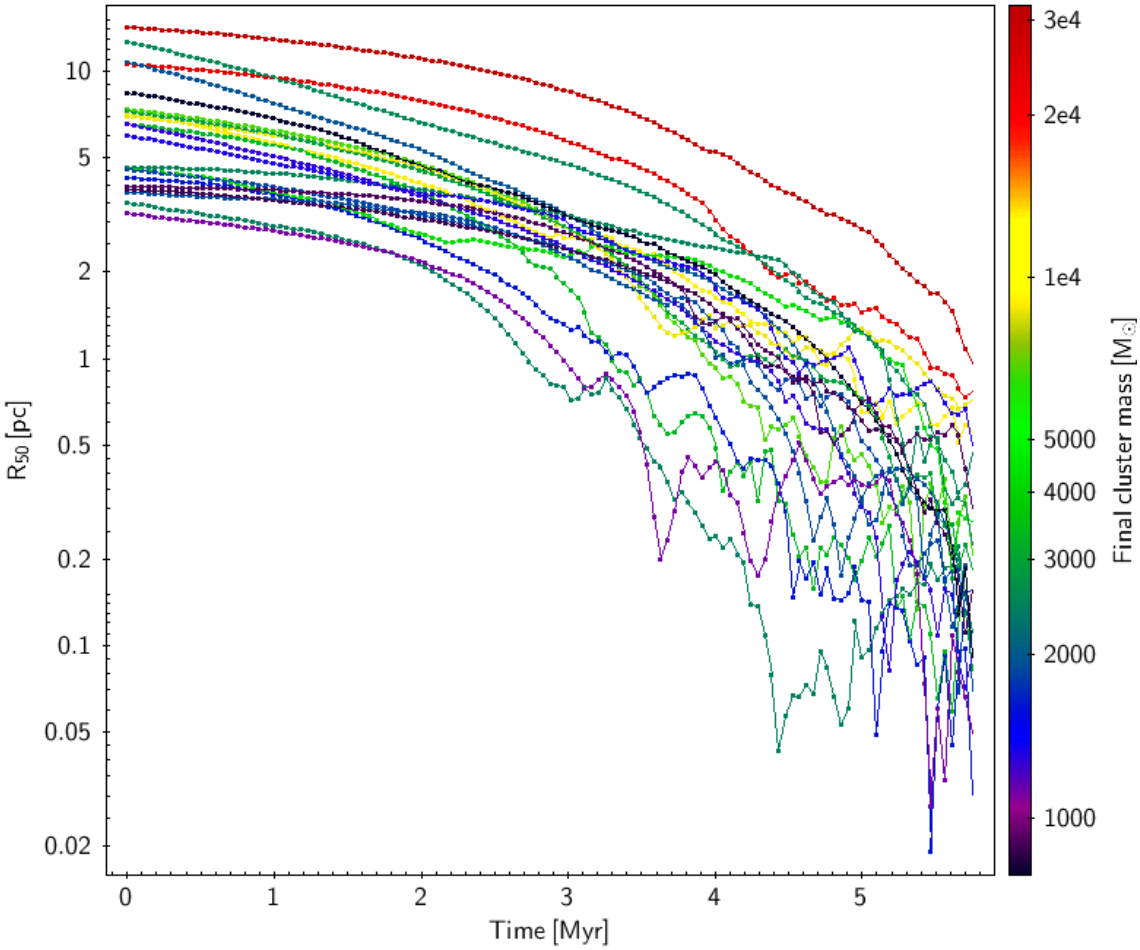

Figure 6.10: The half-mass radii for all clusters in the simulation are shown as a function of time. The half-mass radii were calculated using the conserved total mass of sinks and gas particles to be accreted. Data points are connected with lines between timesteps. Points and lines are colour coded by the final mass of the cluster, which is the same as the total mass of sinks and remaining accreted gas particles. The plot shows the half-mass radii decreasing with time. Over the entire period, the half-mass radii decrease by a factor of almost ten. At all times the more massive clusters have larger half-mass radii than the low mass clusters.

6.6.4 Cluster half-mass radii

Cluster size is the next physical property to be discussed. In this chapter I use the half-mass radius of the cluster, which encloses half of the cluster mass and is a good estimation for cluster size.

Figure 6.10 shows the evolution of half-mass radii for all final clusters. The calculation uses conserved mass by including both sinks and the remaining gas to be accreted to them. Dots in the figure show half-mass radii calculated at each time. The dots are connected by lines, showing how the half-mass radii evolve over multiple time steps. The dots and lines are colour coded by the final cluster masses.

All the clusters in Figure 6.10 show a continuous decrease of half-mass radii over time, which is the result of cloud collapse and cluster formation. Clusters with high final mass retain high half-mass radii throughout: at the beginning of the simulation they are around 10 - 15 pc, while at the end they contract to 1 - 2 pc. Low mass clusters also tend to have smaller initial half mass radii: they start from 3 - 5 pc and end at 0.1 - 0.2 pc half mass radii. High mass clusters also show a smooth evolution throughout the simulation – this is because these clusters never reach low number statistics. At the beginning, while cluster reservoirs are mostly gas dominated, there are around several tens of thousands of gas particles to be accreted, while at the end massive clusters contain several hundred sinks. Low mass clusters at the beginning have a large number of gas particles, but by the end they have been accreted by only a few sinks (close to the low limit in a cluster of six sinks), leading to the evolution of their half-mass radii being noisier.

6.6.5 Mass-radius relation

One of the most fundamental relations describing clusters, either simulated or observed, is their mass-radius (M-R) relation. This makes the M-R relation one of the most useful tools in comparing simulated and observed clusters. In order to obtain the M-R relation, I use the cluster mass (which is the sum of all cluster members) and the half mass radius multiplied by a factor of two. The results for all clusters at all simulation time steps are plotted in Figure 6.11. The data points there are also colour coded by time. Iso-potential and iso-density lines are over-plotted for reference in order to show where the clusters would lie if the cluster means densities or potentials were the same for all masses and sizes.

The doubled half-mass radii are around 0.1 - 0.2 pc for low mass clusters ($<$1000 $M_\odot$) while for the most massive clusters (20000 $M_\odot$) they are as large as 1 - 2 pc. Most of the clusters appear between the 10^{11} and 10^{12} cm^2s^{-2} iso-potential lines. This could be an effect of the cluster definition algorithm which is based on the local and enclosed potentials. This leads the definition to preferentially find spherically symmetric clusters. However, these spherical clusters are likely to be centrally condensed, virialized and not change their geometric shape over time (i.e. the cluster definition excludes filamentary or ridge-like structures which would not be stable).

During the formation of a cluster, gravitational collapse leads to a reduction in cluster size, while mass remains the same if no new sinks form or existing ones accrete. On the other hand,

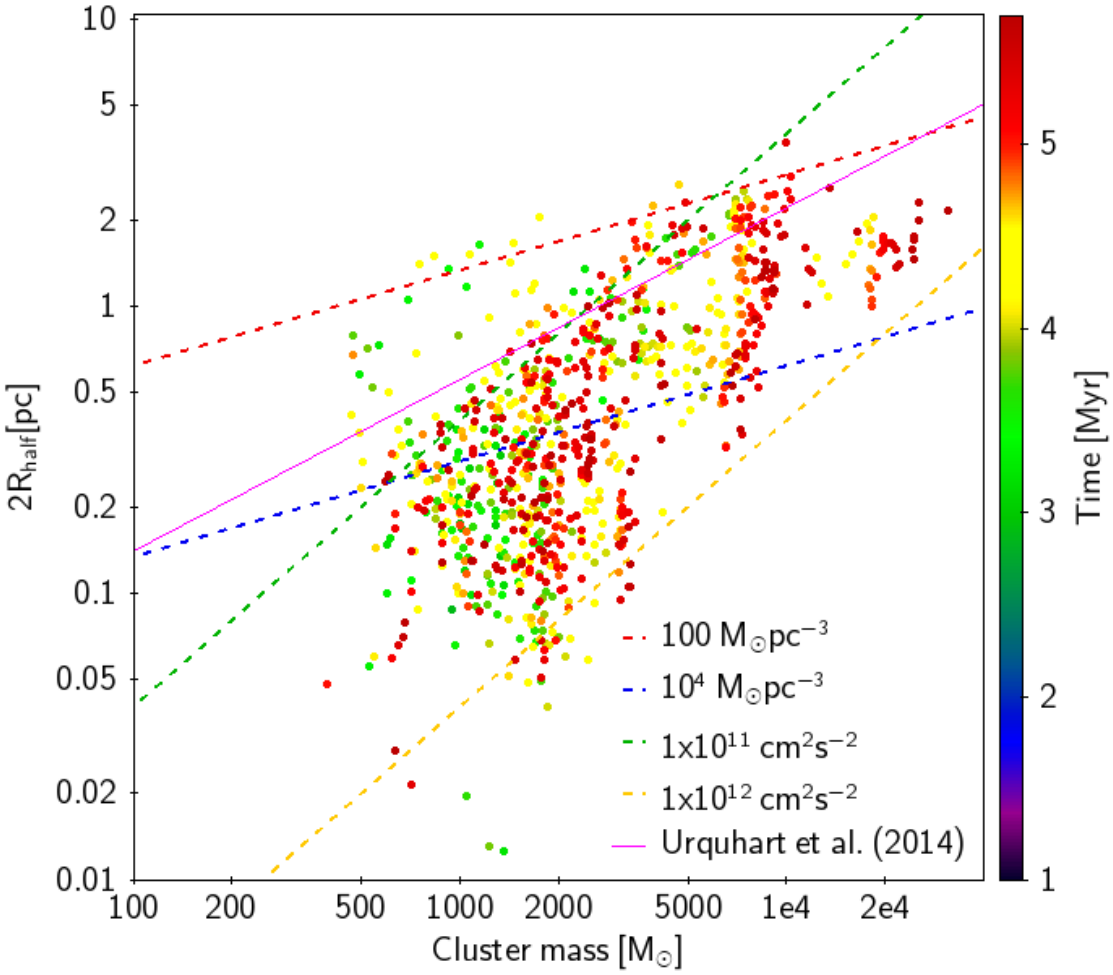

Figure 6.11: The cluster mass-radius relation is shown for all clusters in the simulation. Each data point is plotted for each time. Each cluster is also colour coded by the time at which its mass and half-mass radius were measured. The same clusters can be plotted multiple times - one point at a given time. Iso-density and iso-potential lines are plotted on top of the diagram. The plot shows that more massive clusters are also larger in their half-mass radii. Clusters also move towards larger masses and slightly larger half-mass radii over time.

when a merger occurs the cluster mass, and potentially its physical size, grow significantly as the two pre-merger clusters combine. Most of the clusters migrate towards higher masses in the M-R relation diagram. Their sizes also slightly increase due to merger events taking place.

The solid magenta line in Figure 6.11 shows the Urquhart et al. (2014) M-R relation, estimated for clumps. Clumps in Urquhart et al. (2014) are likely to undergo gravitational collapse and are thus still contracting in their sizes. Figure 6.11 shows just formed clusters. As the clumps collapse, they would move downwards in Figure 6.11 and thus this explains why the Urquhart et al. (2014) M-R relation is still above most of the clusters, discussed here. This does not contradict the evolution of clusters in Figure 6.11 as the cluster finder does not consider collapsing gas mass, which will be accreted at later times. The logharithmic slope of the Urquhart et al. (2014) M-R relation matches well with the one in Figure 6.11, showing that the forming cluster M-R relation is likely to be between iso-density and iso-potential power laws.

6.6.6 Specific angular momentum

The cluster angular momentum is another fundamental property, related to the cluster rotation. The specific angular momentum (angular momentum per unit mass) is also a property of the cluster forming environment. When a cluster forms, its angular momentum is likely to be conserved. However, some may be lost through shocking and transportation beyond the system (e.g. angular momentum could be transported from the inner parts of the cluster outwards). Thus, the angular momentum of the same mass making up a given cluster will not necessarily be conserved, as there may be losses through shocking and transportation through interactions with other particles in the environment.

Defining clusters at each timestep, I calculated their specific angular momenta and plotted specific angular momenta against cluster mass in Figure 6.12. Again each cluster is plotted at each time, which is indicated by the colour of the point. All the members of a given cluster are treated relative to its centre of mass when calculating the specific angular momentum.

Figure 6.12 clearly shows that more massive clusters have larger specific angular momentum. This might be because more massive clusters form over larger scales and have richer merger histories. Material falling into the cluster's gravitational potential during the collapse phase preserves its angular momentum, and if the material moves inwards from even larger

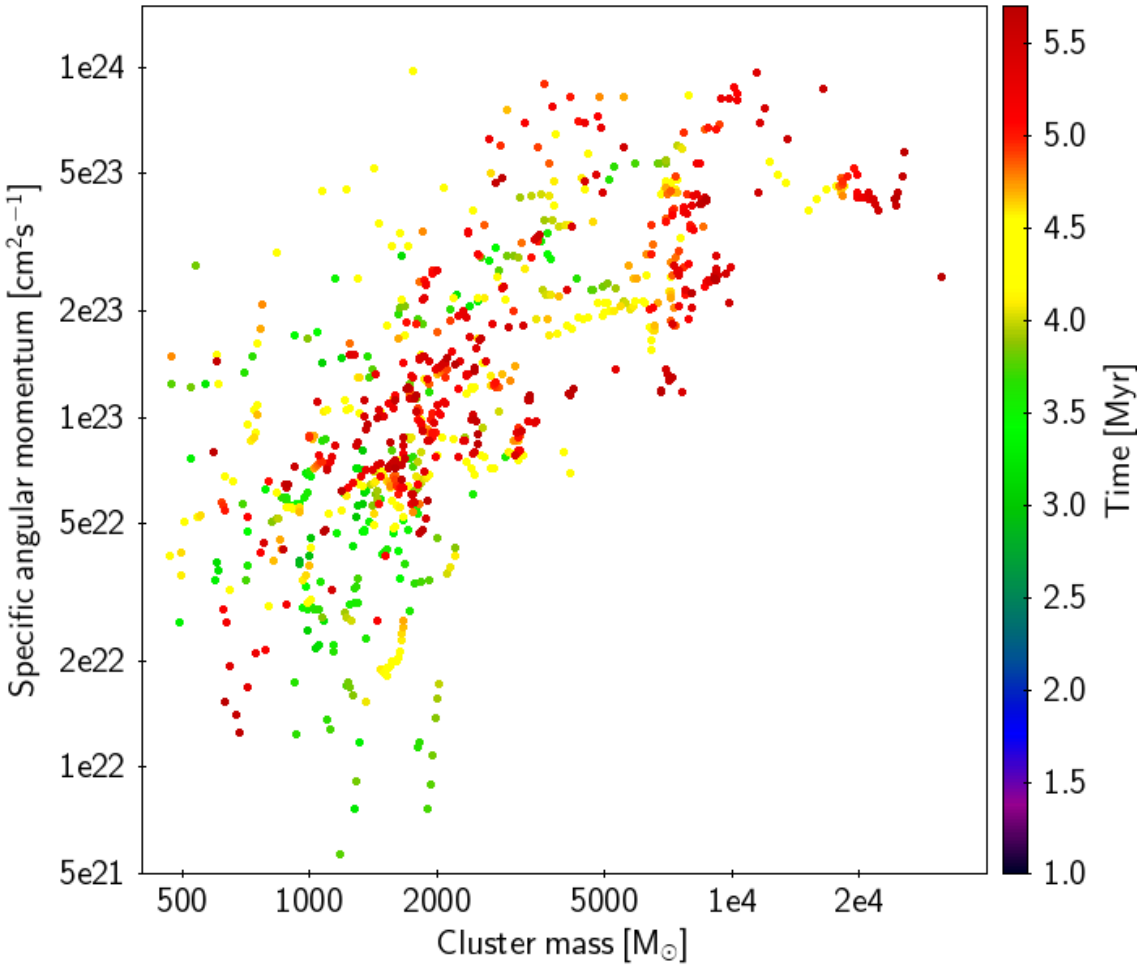

Figure 6.12: The specific angular momentum of clusters is shown as a function of cluster mass. Clusters are plotted for all timesteps in the simulation, meaning that the same cluster can be plotted at multiple points in the diagram. Each cluster is colour coded by the time when cluster mass and specific angular momentum were measured. The plot shows that the more massive clusters have higher specific angular momenta. This happens because more massive clusters form from physically larger clouds and so inherit more angular momentum. The clusters also evolve in time to higher masses and specific angular momentum.

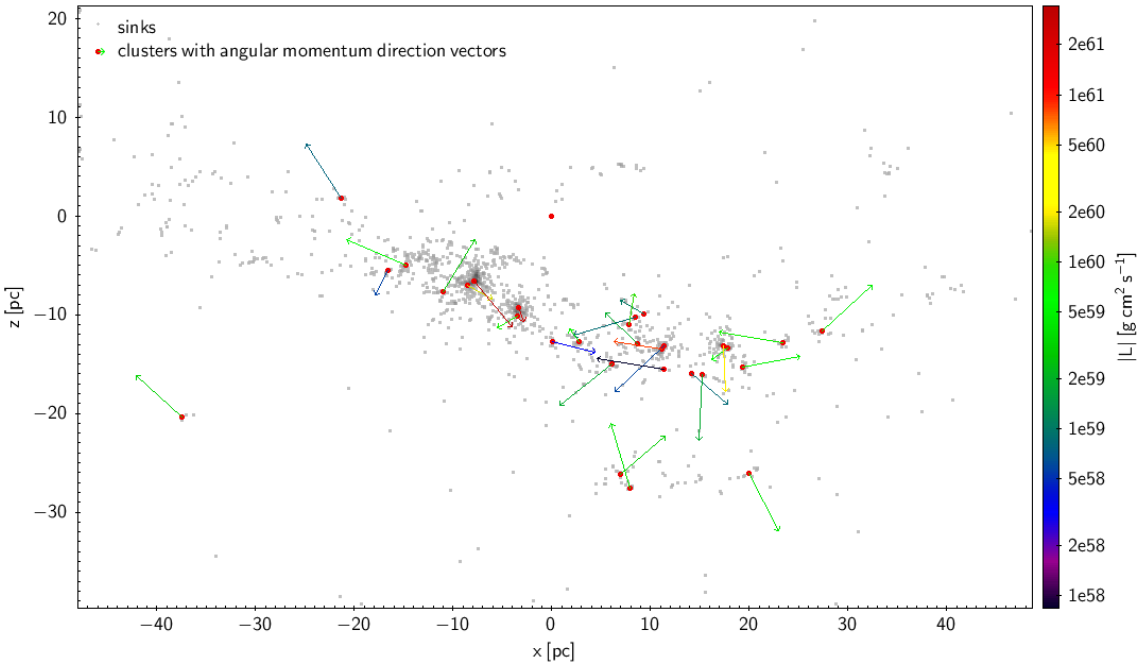

Figure 6.13: The cluster angular momentum vectors are plotted for clusters in the main star formation region at the end of the simulation. Grey points show the positions of all the sink particles and red dots the centres of mass for clusters which have been identified. The vectors point in the direction of the clusters' angular momenta and are also colour coded according to the magnitude of the angular momentum. The plot shows that the directions of angular momentum vectors are random and do not display correlation with the presence of the spiral arm or the direction of the shock. More massive clusters possess more angular momentum.

scales it naturally brings more angular momentum with it. The merging of clusters not only produces the jumps in mass seen in Figure 6.12, but also increases the specific angular momentum as the pre-merger clusters formed in separate environments. This means they possess not only their own internal angular momentum, but also the relative angular momentum between the two clusters. Thus mergers bring clusters towards both higher masses and specific angular momenta in Figure 6.12.

6.6.7 Cluster angular momentum direction

The direction of a given cluster's angular momentum vector describes the axis of the cluster's net rotation. While observations can't measure clusters' angular momentum vectors, they are easily measurable in simulations and reveal more about cluster evolution.

Figure 6.13 shows the map of clusters with their actual angular momentum vectors plotted as arrows. The arrows are colour coded by the absolute value of cluster net angular momentum and point in the direction of the vector. The cluster centres of mass are plotted as red dots, and all sinks as grey points.

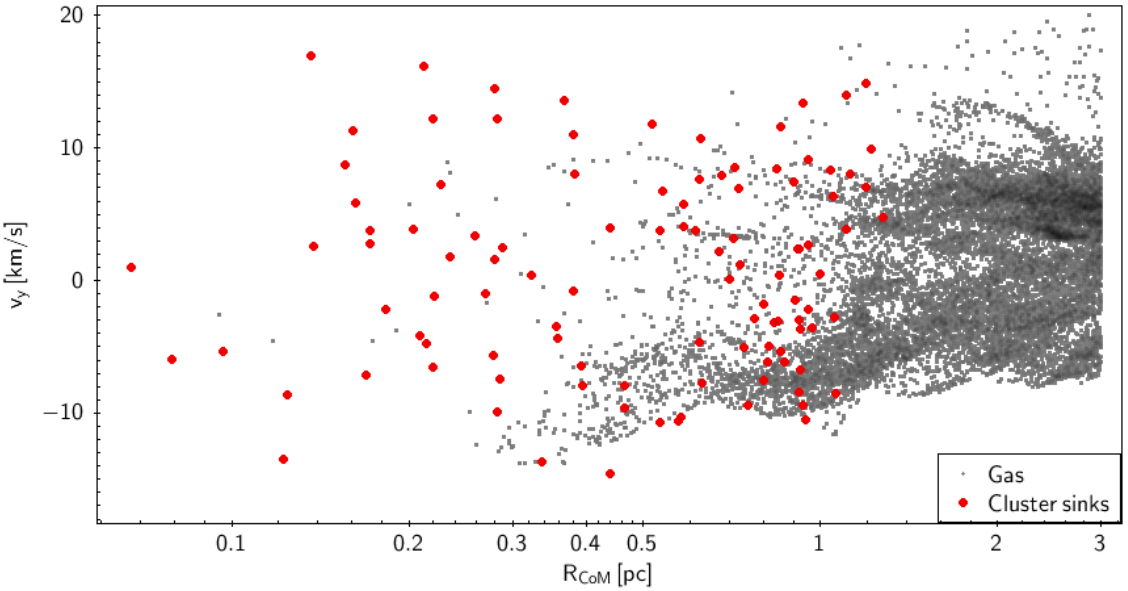

Figure 6.14: Sink and gas particle velocities v_y relative to the centre of mass for the second most massive cluster are shown at the end of simulation. Red dots represent sink members of the cluster, and the small grey dots all gas particles within 3 pc of the cluster's centre of mass. The internal part of the profile contains only sinks. On the other hand, there are only gas particles outside 1 pc. Any gas particles moving towards the centre of the cluster are accreted on their way and so never reach the inner regions. Most of the accretion happens within 0.5 - 1 pc radius. A velocity dispersion in the y component of nearly 20 km/s is visible. This is lower in the outskirts of the cluster. This trend in the velocity dispersion is visible in the sinks as well as the gas particles, with material showing a wide range of velocities across both positive and negative y towards the cluster's centre of mass.

The angular momentum vectors appear to be randomly oriented in space, showing very little correlation with the larger scale cluster distribution along the spiral arm. This might be due to the angular momentum being predefined by the material contributing to cluster formation. As the material collapses locally, it brings angular momentum from the larger cloud scales to smaller scales. However, as individual clouds have their own internal motions, this means that the combined rotation of the final cluster could also be quite random.

6.6.8 Internal velocities

The velocity dispersion in the cluster can be used to measure how fast the stars are moving, which itself gives information on the cluster's overall gravitational potential. At small radii, where stars are close to the cluster centre of mass, they move at their maximum velocities, as all gravitational potential energy is turned into kinetic energy. On the outskirts of the cluster, the situation is the opposite: most of the kinetic energy of stars has been turned into potential energy and as a result, stars move more slowly.

Figure 6.14 shows the example profile of velocities for the second most massive cluster

at the end of the simulation. The second most massive cluster was chosen because it had no major mergers for 1.5 Myr and developed a smooth centrally condensed internal structure, while the most massive cluster in the simulation experienced a major merger just 0.2 Myr before the end of the simulation and thus still has a hierarchical structure (see Figure 6.9). The v_y velocity component (chosen due to the same direction as the spiral shock) is plotted as a function of distance from the cluster's centre of mass. v_y is also calculated to be relative to the cluster's centre of mass velocity. Red dots represent individual sinks, while grey dots represent gas particles.

Figure 6.14 clearly shows that at smaller radii (0.1 - 0.5 pc) the region is dominated mostly by sinks. At large radii (0.5 - 3 pc) it is dominated by gas. Due to the low number statistics, a velocity dispersion profile can't be calculated accurately but instead an approximate comparison can be done based on visual scattering in the inner and outer parts of the profile. The inner part of the cluster shows a slightly larger scattering in velocities ($\sim$15 km/s between smallest and largest v_y values) than the outer part ($\sim$10 km/s), which is a natural consequence of the kinetic-potential energy distribution in the cluster. As there are a larger number of gas particles present in the outer part of the profile, flow streams are clearly visible in the profile. These streams show larger spreads in velocity when moving from large (3 pc) to small (0.5 pc) radii, which indicates that they have been accelerated by the global gravitational potential of the cluster. Moving inwards it becomes more and more likely that gas will have been accreted to a sink – this is why there is no gas visible at the cluster centre. As a result, small radii are dominated by the mass in sinks, and large radii by the mass in gas.

6.6.9 Cluster sphericity and enclosed mass slope

The cluster sphericity is a property describing how spherical a cluster's shape is. On the other hand, the enclosed mass slope, derived from enclosed mass radial profile, describes how centrally concentrated the cluster is.

To calculate the sphericity, I use the moment of inertia tensor:

$$\begin{bmatrix} I_{xx} & I_{xy} & I_{xz} \\ I_{yx} & I_{yy} & I_{yz} \\ I_{zx} & I_{zy} & I_{zz} \end{bmatrix}$$

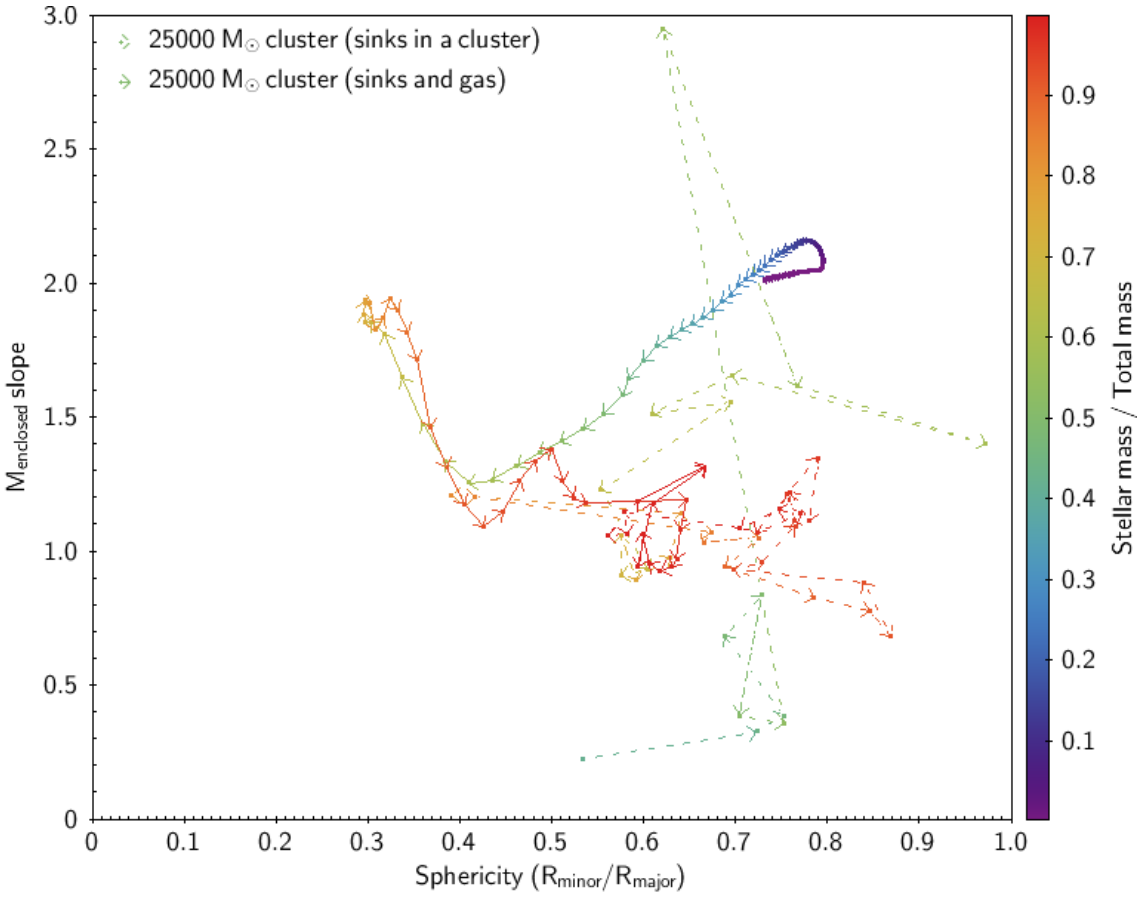

Figure 6.15: The cluster sphericity and enclosed mass slope are shown for the second most massive cluster for all timesteps of the simulation. The sphericity is calculated using the moment of inertia tensor. There are two cases plotted - one including only the sinks which had already formed, and another including both the sinks and any remaining gas particles due to be accreted. Data points at given timesteps are plotted as dots. They are connected with arrow-tracks pointing towards the next timestep in the evolution. The dots and lines are colour coded by the sink mass fraction at each given time. The plot shows that the cluster evolves along a complex path. The sphericity at early times decreases as the system approaches a filamentary phase, and later on increases as filaments collapse into the cluster. The enclosed mass slope systematically decreases for the conserved mass, showing that the cluster becomes more centrally condensed. The large scattering at the end of evolution is produced by low number statistics.

Here the diagonal components are calculated by summing up the particle masses multiplied by the other two position components added together in quadrature:

$$I_{xx} = \sum_{i=1}^{n} m_i(y_i^2 + z_i^2) \tag{6.2}$$

$$I_{yy} = \sum_{i=1}^{n} m_i(x_i^2 + z_i^2) \tag{6.3}$$

$$I_{zz} = \sum_{i=1}^{n} m_i(x_i^2 + y_i^2) \tag{6.4}$$

Each of the particle positions here, x_i, y_i and z_i, are relative to the centre of mass as calculated using all particles in the cluster.

The mixed tensor components are symmetric (I_{xy}=I_{yx}, I_{xz}=I_{zx}, I_{yz}=I_{zy}) and only need to be calculated for one side. These components are calculated by summing up the particles' positions multiplied by their masses:

$$I_{xy} = \sum_{i=1}^{n} m_i x_i y_i \tag{6.5}$$

$$I_{xz} = \sum_{i=1}^{n} m_i x_i z_i \tag{6.6}$$

$$I_{yz} = \sum_{i=1}^{n} m_i y_i z_i \tag{6.7}$$

Once all nine components of the moment of inertia tensor are calculated, the three eigenvalues of the matrix were found using the Jacobi method. The length of the minor axis is found from the minimum value of the three eigenvalues, while the major axis is found from the maximum. When these are known, the sphericity can be defined as a ratio of the minor to major axis:

$$Sphericity = l_{minor}/l_{major} \tag{6.8}$$

The enclosed mass slope was calculated by fitting a line to the cumulative radial mass profile for each cluster. Once the line is fitted, its slope is used here as the enclosed mass slope parameter.

Figure 6.15 shows the evolution of the enclosed mass slope as a function of sphericity for the second most massive cluster in the simulation (as this cluster has developed a smooth and spherical shape by the end of the simulation due to the quiescent merger history at the late times). There are two scenarios shown in this plot. One is with conserved mass (solid lines), for which the slope and sphericity were calculated using both the sinks and the gas which was going to be accreted, but hadn't yet. For the second (dashed line), only the sinks in the cluster were included. Each point in this plot is a calculation for a different time. The arrows connecting these points show the direction of evolution over time. Finally, both the points and lines are colour coded by the ratio of mass in sinks to the total system mass (sinks and gas remaining to be accreted).

The plot (Figure 6.15) shows that at late times the cluster sphericity is high, which means that the cluster becomes more spherically symmetric. It also shows a decrease in the enclosed mass slope, which means that the cluster gets more centrally condensed over time. The overall evolution appears to be quite irregular. At the beginning, the mass conserved track shows a high slope and sphericity. This is because the cloud in space is not spread in one particular direction. Later, the sphericity starts to decrease because the cloud collapses into the ridge. And finally, as the ridge collapses into the cluster, the sphericity increases again. The sinks-only track appears to be much noisier due to the low number of sinks formed at early times. At late times, as the sinks come to dominate the total mass, both tracks start to match more closely.

Figure 6.15 is only shown for the second most massive cluster. However, the plot is different for every different cluster in the simulation as sphericity and enclosed mass slope are sensitive to geometric changes over the time. In order to reduce the noise between two timesteps it is necessary to have either the larger resolution or a smaller timestep in the simulation.

6.7 Mass growth of stellar clusters

One of the key questions asked is whether clusters grow by accreting gas to the sinks they already contain or new sinks from outside of the cluster. To answer this, I measure the mass growth of sinks while they are in the cluster. Then by summing over cluster members, I obtain

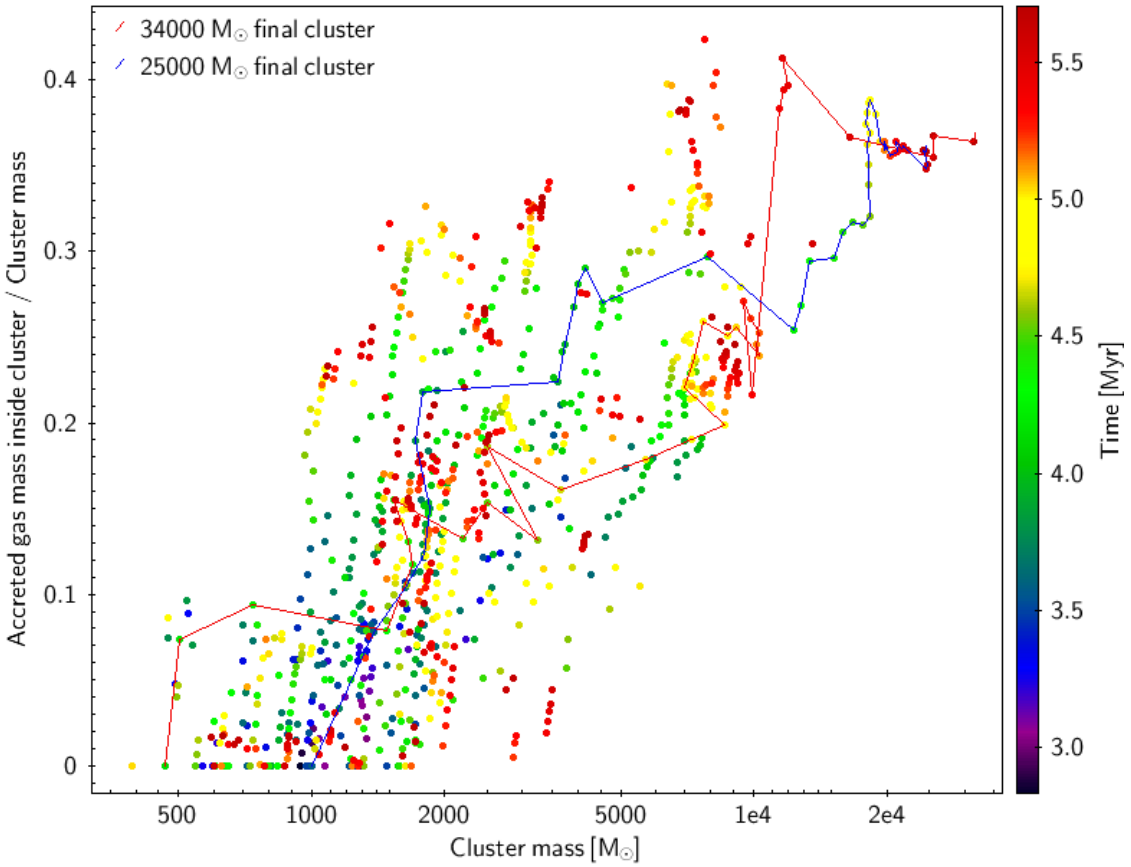

Figure 6.16: Cluster mass growth from gas accretion is compared with the total cluster mass. The accreted gas mass is calculated by finding how much mass is accreted to existing sinks within the cluster. Each cluster can appear in the plot multiple times but only once per timestep. The paths of the two most massive clusters are shown as red and blue lines. The diagram shows that more massive clusters also experience more significant gas accretion to cluster sinks. The cluster tracks tend to higher masses and larger accreted mass ratios. The accretion of gas particles to a cluster moves it to higher ratios, while the accretion of sinks moves it to lower ratios.

the overall growth of the cluster mass from accretion within the cluster. This mass growth is plotted as a function of the total cluster mass for all clusters at all time steps throughout the simulation in Figure 6.16. The red and blue lines show the evolution of the two most massive clusters.

The least massive clusters have the lowest ratios of mass accreted within the cluster to the total. This could be partially affected by the cluster definition: when a cluster is defined for the first time, it must contain at least six sinks. On the other hand, these six sinks may have collected a large proportion of their masses while being outside the cluster. As low mass clusters have very small sizes (i.e. half mass radii 0.1-0.2 pc) and low gravitational potentials, they are not able to collect a large amount of material from the environment. Hence the accretion inside the low mass clusters is also low and most of their mass comes from sink formation and accretion before the clusters assembled. This is only because sinks obtained their mass while unclustered. The accreted mass inside the cluster is therefore zero when the cluster is defined for the first time.

Conversely, high mass clusters accrete up to 40 % of their total mass onto sinks which are already in the cluster. These massive clusters are also larger in their sizes and have deeper global gravitational potentials. As a result, they are capable of channelling large quantities of surrounding gas from the environment towards the cluster centre, driving continuous accretion. This means that gas accretion to clustered sinks mostly occurs in high mass clusters.

Clusters can be seen evolving from the bottom left to the upper right part of Figure 6.16. The continuous accretion of gas draws smooth "trails" almost vertically upwards, visible at early to intermediate simulation times. On the other hand, the accretion of sinks moves the ratios downwards. The merging of two clusters leads to the addition of pre-existing sinks, producing large horizontal jumps to a new ratio. This is an average inherited from the pre-merger clusters.

6.8 Stellar age spreads

Stellar ages and age spreads in clusters are two of the key properties, detectable by observations and predictable by simulations. SPH simulations allow us to easily obtain the star formation times and so stellar ages.

Firstly to illustrate the presence of possible stellar age spreads I used three subsets of ac-

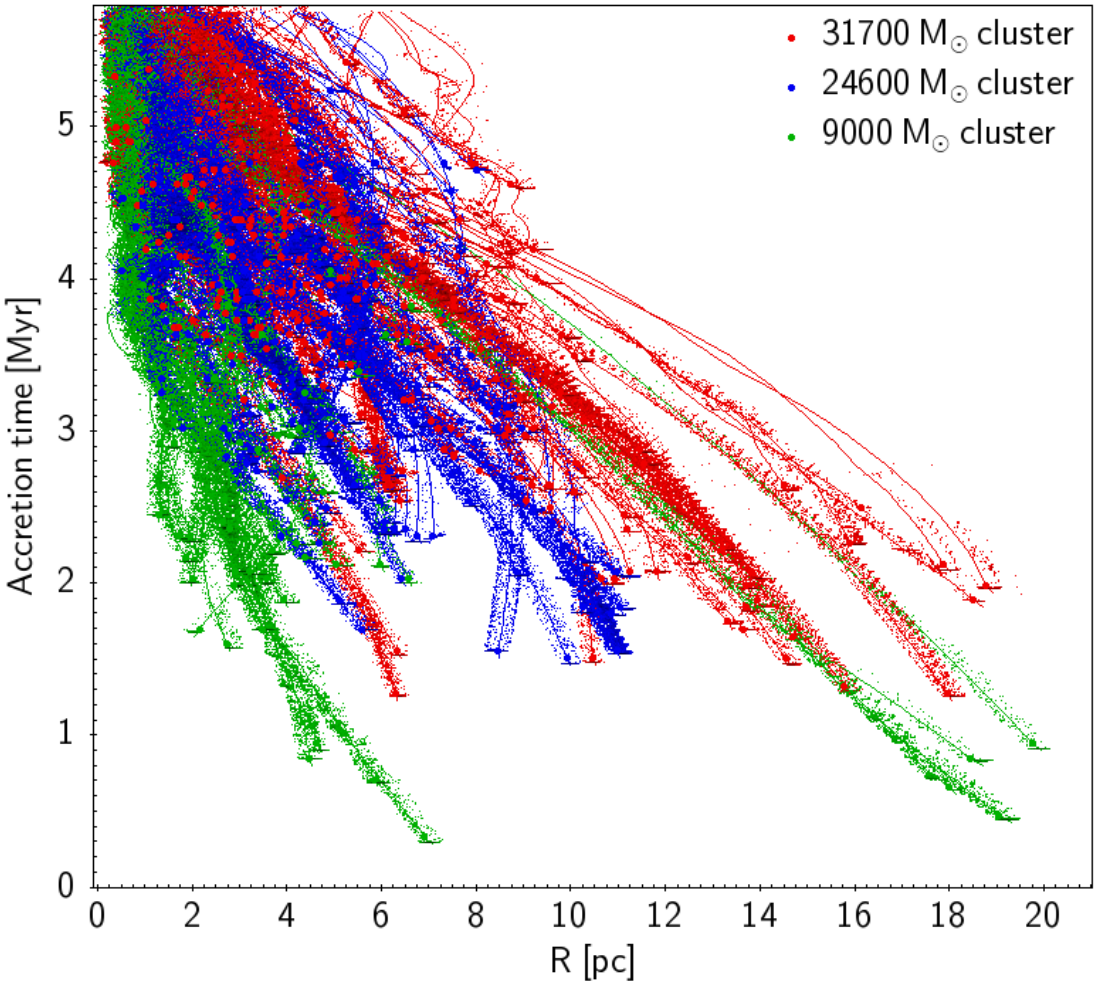

Figure 6.17: The accretion paths of individual sinks are shown for the three most massive clusters in the simulation. Sink formation events are plotted as large dots, the paths of sinks' motions as coloured lines, and accretion events as small dots. The plot shows all the sinks moving towards the clusters' centres of mass. Most sinks do not move alone but in groups and subclusters, indicating a hierarchical merging scenario. The sinks continue to accrete gas particles along their paths as they move, continuing to grow in mass all the time. This leads to significant sink age spreads inside the clusters.

creted particles, which contribute to the formation of the three most massive clusters accordingly. The accretion time of these particles is plotted as a function of distance from the cluster centre of mass (Figure 6.17) when the particle was accreted. All three clusters are plotted in different colours. The sinks' movement paths are also plotted as continuous lines in order to see where non-accreting sinks were moving. As the accreted particles were accreted not exactly at the position of the sink but between 0.1 and 0.25 pc from it, accreted particles can be seen as scattered dots around sink movement paths. Sink formation events are plotted as solid dots at the beginning of each sink path.

Figure 6.17 shows the collapse of all three clusters as their sinks fall towards the cluster centre of mass. The accretion appears to be ongoing after the sinks form. Some sinks form as early as at 1 Myr, while others form only just before the simulation's end. This produces potential age spreads of several Myr. However, real stellar age spreads might be different as the simulation in this thesis is limited to the minimum sink mass of 11 $M_{\odot}$. The sinks are also grouped into smaller sub-clusters at larger radii. These sub-clusters have smaller age spreads, as the sinks formed locally at almost the same time. However, once the sub-clusters merge, the resulting cluster has a larger age dispersion due to the mixing of the different populations.

While clusters in Figure 6.17 have age spreads of several Myr, the real age spreads can be affected by the minimum sink mass of 11 $M_{\odot}$. As individual sinks do not represent individual stars, it is unclear if accreted gas goes onto existing stars or forms new ones.

6.8.1 Cluster mean star formation age

Before going deeper into stellar age spreads, it is necessary to determine the mean star formation ages in clusters. Each sink at each time has its own star formation age. Here the star formation age is defined as the difference between the simulation time and the mean star formation time. The mean star formation time is itself determined by averaging the accretion times for all gas particles contributing to the growth of that sink. As the sinks continue to accrete, their mean star formation times increase with simulation time. As a result, continuous accretion onto sinks can decrease their star formation ages. This is in a good agreement with Tout et al. (1999), who estimated that accretion can reduce the apparent ages in young forming stars. Due to this age reduction effect from accretion, mean star formation ages are more likely to represent real stellar ages compared to than simple sink ages. Simulation data shows that sink mean star formation ages are about two-thirds of the sink ages. The cluster

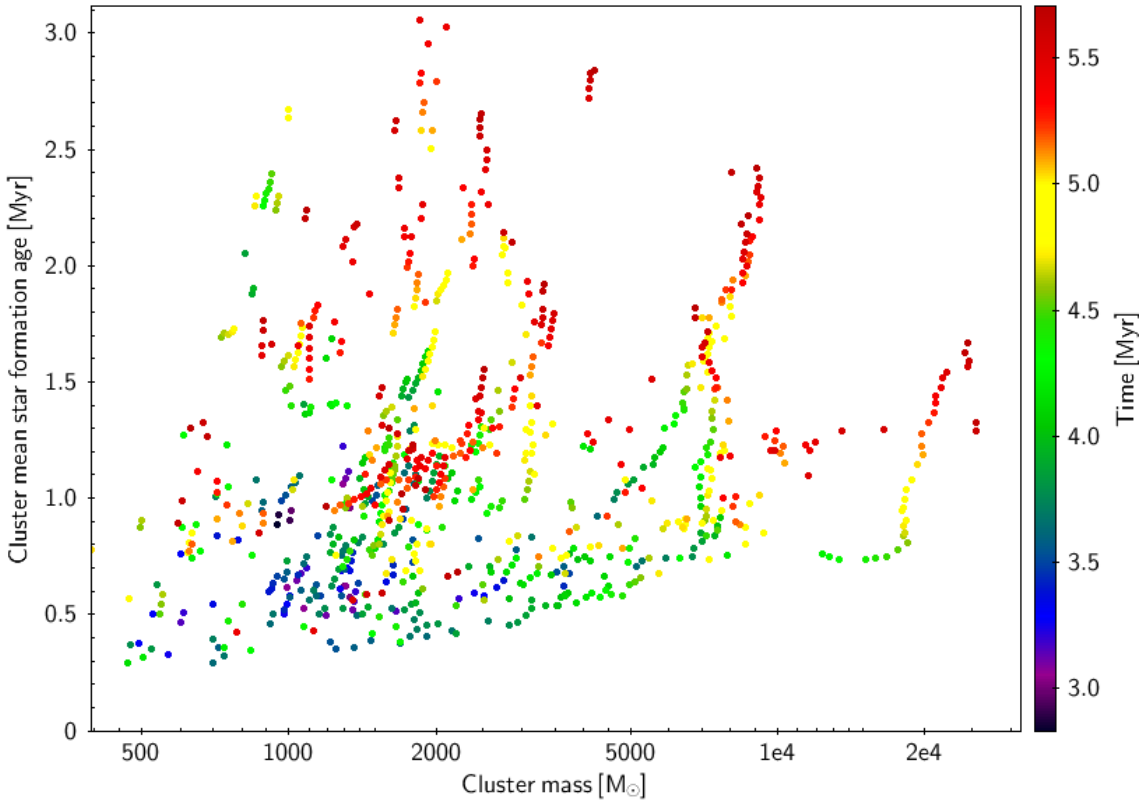

Figure 6.18: The cluster mean star formation age is shown as a function of cluster mass. Data is used for all simulation timesteps and thus each cluster can have multiple points in the diagram. Each point is colour coded by the time when the mean star formation age and cluster mass were measured. The plot shows individual clusters leaving tracks in the diagram. The clusters show only small growth in the mean star formation age at early times. As accretion continues the mean accretion time remains close to the simulation time, and the star formation age remains nearly constant. Most clusters reach a point where the tracks turn vertically upwards. At these points the accretion was reduced and the mean accretion time was left almost unchanged, leading the star formation age to increase.

mean star formation age is an average of the mean star formation ages of all the cluster sinks.

Figure 6.18 shows the cluster mean star formation age as a function of cluster mass over all simulation times where the clusters were defined. The colour shows the simulation time. The diagram clearly shows that the clusters evolve towards higher masses and also towards higher mean star formation ages. The individual clusters leave clearly distinguishable tracks in this diagram. At early times clusters show quite significant growth in their masses but low growth in mean star formation age. During this phase gas accretion dominates to the point that the mean star formation ages are almost constant. While the early accreted gas comes from smaller distances and later accreted gas from larger scales, the main factor which defines the cluster tracks in Figure 6.18 is how much gas has been already accreted at the given time. The phase during which accretion is significant applied mostly to clusters with mean star formation ages below 1 Myr. The mean star formation ages start to increase faster at later times, but it appears that their mass growth is also reduced. This could happen if the cluster sinks deplete most of the surrounding gas, leaving nothing else to fuel further accretion. Alternatively, the cluster sinks could move out of their natal clouds if low density incoming pre-shock gas continues to push high density gas in the direction of the flow. In this case, the sinks would not move with the high density clouds, and would appear to be coming out of them. A third possibility could be that the cluster's effective accretion volume is reduced as the sinks are packed into a high stellar density gas-free cluster core. If sinks are closer than 0.1 pc, their inner accretion radii begin to overlap – the volume becomes fully sink dominated and there is no space for free gas particles to exist without being immediately accreted. In order to answer which scenario or several of them dominates further in depth investigation is needed, which I leave as a future step.

6.8.2 Star formation age dispersion in clusters

Finally, the star formation age dispersion is the property most likely to represent stellar age spreads in clusters. In order to calculate the star formation age dispersion, I use all the particles accreted to cluster sinks and calculate a dispersion in their accretion times. Figure 6.19 shows that the star formation age dispersion increased over time in a manner similar to the mean star formation age in the clusters. The lower mass clusters mostly have small star formation age dispersions below 0.5 Myr. On the other hand high mass clusters never have such small age dispersions. This is because more massive clusters gained their mass from accretion which

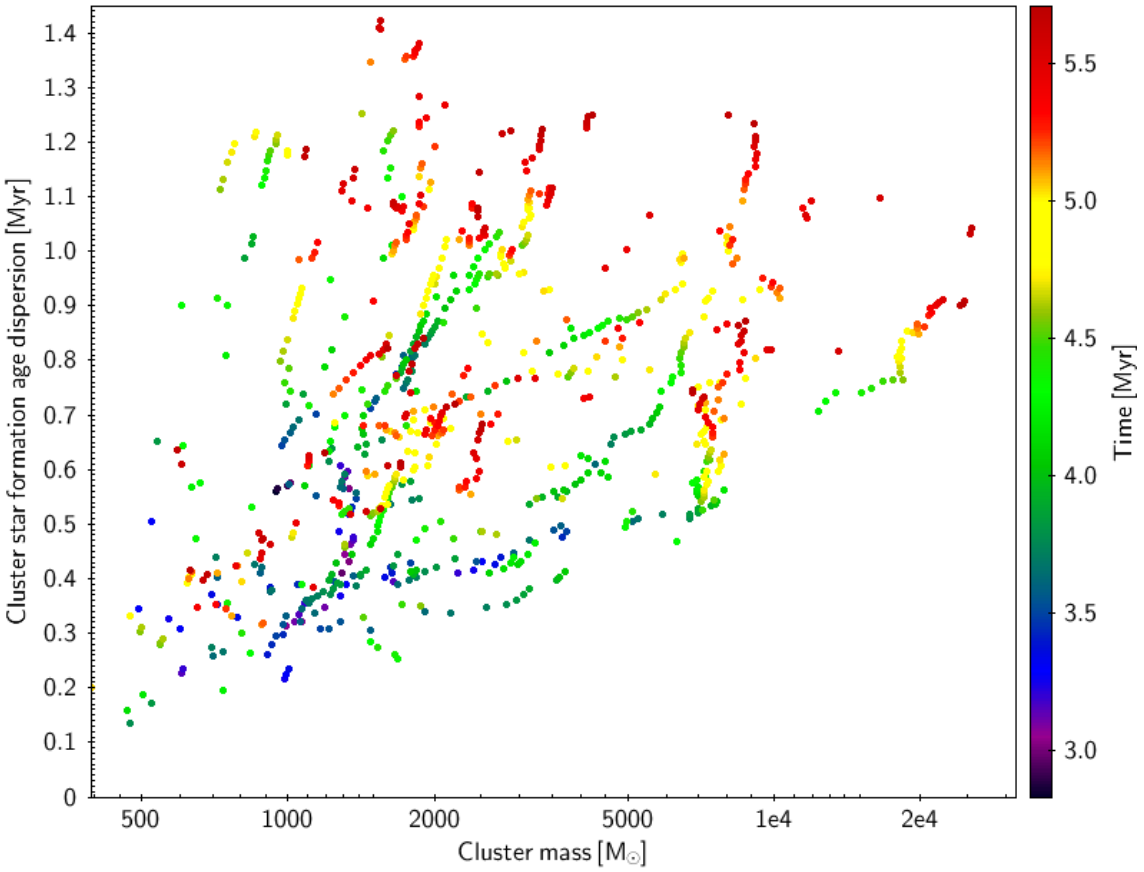

Figure 6.19: The clusters' star formation age dispersion is shown as a function of cluster mass. Individual clusters are colour coded by the simulation time when the star formation age dispersion and cluster mass were measured, similarly to what is shown in Figure 6.18. Individual cluster tracks show that low mass clusters have smaller star formation age dispersions than high mass clusters. It is also easy to see that the mean star formation age dispersion continues to increase with time. The star formation age dispersion in high mass clusters is also likely to be amplified by the mergers experience during their evolution. Mergers bring in material from a large variety of environments which have different star formation times.

took place over a long period of time, and also cluster mergers. This leads to an increase in the dispersion as in the final clusters the material has been gathered from different environments and continuously accreted over longer periods of time. There are also several clusters of 1000 - 2000 $M_{\odot}$ which have star formation age dispersions as large as 1.4 Myr. Some sinks from these clusters have formed earlier, but they appear to have low accretion rates over the entire simulation. As a result, these clusters continue to slowly accrete throughout the simulation, producing a large star formation age dispersion.

Mean star formation age and star formation age dispersion in clusters of sinks can be put in comparison with observed young cluster ages and stellar age dispersions accordingly. However, it is important to mention that these two quantities are limited by their definition. The first point is that minimum sink masses are 11 $M_{\odot}$ which could lead to slightly different ages and age dispersions depending is accretion onto sinks would mean the accretion on already existing stars or formation of new stars. This can be addressed as a future step with higher resolution simulations in order to determine resolution effects on star formation ages and age dispersions. The second point is to investigate how robust is the Tout et al. (1999) model, which suggests that ongoing accretion reduces star formation ages and that it is a good choice to simply average over all accreted particles.

6.9 Summary

In this chapter I investigated the formation of stellar clusters. I started by viewing maps of the main star forming region in the simulation of Bonnell et al. (2013), where I applied the gravitational potential-based cluster finding algorithm. The maps show that the clusters form in the main star forming region (Figure 6.2) but do not necessarily align with highest density clouds. A gradient of star formation ages can be seen along the main star forming ridge (Figure 6.3). This is likely to be a result of the shock, which approached one side of the star forming region earlier than the other. Figure 6.4 shows the evolution of the cluster over time when including either all the gas or just that which is accreted to the cluster. This shows that the gas contributing to clusters comes from well-defined regions forming parts of the highest density filaments. While the filaments collapse under self-gravity, the region is also compressed by the spiral shock. The initial cluster-forming clouds are several tens of parsecs across (Figure 6.5). Clouds forming different clusters also intersect with one another, but the boundaries between them are well-defined. It was also possible to trace how cluster forming sinks moved before

they came into the cluster (Figure 6.6). This shows that the first sinks formed individually in isolated locations and moved into the cluster during the larger scale gravitational collapse of the region. During this collapse phase, sinks accreted gas while moving along their paths.

I then investigated the physical properties of clusters and their evolution over time. Firstly, a comparison between sink densities at late times and the initial protosink densities (Figure 6.7) shows that high density and clustered sinks have larger initial protosink densities than isolated low final density sinks. The cluster density profiles show that clusters can extend outwards for several parsecs before the profile reaches neighbouring clusters (Figure 6.8). Cluster masses and their evolution over time were illustrated in the mass merger tree diagram (Figure 6.9), showing how cluster masses increase over time and how subclusters merge into larger clusters. This shows that more massive clusters have longer lifetimes and experience more mergers. At all times the clusters collapse as their half-mass radii continue to decrease (Figure 6.10). Lower mass clusters also possess smaller half-mass radii than high mass clusters at all times. The mass-radius relation (Figure 6.11) shows that more massive clusters have larger sizes. More massive clusters also show larger specific angular momenta (Figure 6.12) as they collapse from larger scales than low mass clusters, naturally inheriting large specific angular momenta. The clusters' angular momenta are directed randomly and do not show strong correlation with the direction of the shock (Figure 6.13). The velocity profiles within clusters show the scattering of velocities to be larger in the cluster centres and lower in the outskirts (Figure 6.14). Most of the gas particles which are infalling to the cluster centre are accreted while underway, as sink densities increase towards the inner regions. As cluster forming clouds firstly collapse to filaments before they reach the cluster phase, the sphericities (Figure 6.15) of collapsing clouds decrease during filament formation and then increase when the filament collapses to a cluster. The slope of the enclosed mass profile shows that clusters eventually become centrally condensed as the simulation progresses.

The mass in low mass clusters is mostly dominated by the accretion of surrounding sinks while high mass clusters with their massive gravitational potentials channel gas from the surrounding environment towards the cluster centre, driving accretion onto sinks (Figure 6.16).

Clusters show large stellar age spreads (Figure 6.17). This is a result of ongoing accretion while sinks move along their paths, as well as merging when subclusters have formed in different environments with different star formation times. The stellar age dispersions (Figure

6.19) show that more massive clusters have large age spreads while less massive clusters can have both large and small age spreads. Cluster age dispersions also increase over time as new accretion and sink formation events take place.

7

Formation of OB associations

OB associations are large loose objects, containing young OB stars which are located not in compact clusters, but in large volumes with sizes ranging between several tens pc to over 100 pc (Murdin 2001). OB associations have been known since Ambartsumian (1949, 1955) introduced them. According to Lada & Lada 2003 most of O and early B stars form in clusters and OB associations. According to Gieles & Portegies Zwart (2011) clusters are gravitationally bound while associations are not. Gieles & Portegies Zwart (2011) also distinguish between clusters and associations based on cluster age ratio with its crossing time, i.e. if $\mathrm{Age}/t_{\mathrm{cross}} > 1$ then the object is a cluster, otherwise an association. Bastian (2013) finds that only $\sim$10 % of stars form in such clusters, while the rest form in association as well as in the distributed mode. Unfortunately Gieles & Portegies Zwart (2011) ratio of $\mathrm{Age}/t_{\mathrm{cross}}$ is complicated to determine for young embedded clusters (due to their small ages), which is essential in understanding the early formation of associations.

The reason, of how stars in OB associations become so loose is not well understood. As I discussed in the Introduction chapter, there are several theories created in order to explain the

origin of OB associations. Clark et al. (2005) propose that OB associations may have formed from gravitationally unbound clouds, with star formation occurring only on small scales. Oort (1955) and Elmegreen & Lada (1977) discuss that feedback from formed stars could have helped young clusters to become unbound, after the loss of gas, and expand to larger scales. While Fernández et al. (2008) uses spiral arm studies with backwards integration to explain formation of OB associations.

There are currently no numerical simulations which trace the details of individual OB association formation. Most of the star formation simulations use idealised initial conditions, with no galactic context included and forming only one central cluster (such as Bate et al. 2003; Smith et al. 2009; Bonnell et al. 2011). There are also no studies that trace the evolution of groups and clusters of formed sink particles. As typical simulations are of bound cluster formation (Bate et al. 2003; Smith et al. 2009; Bonnell et al. 2011), OB associations are unbound, hence they cannot form from bound conditions unless feedback or something helps. Even if some OB association candidates were forming, they could be missed just because in depth studies of cluster tracing over time has not been studied in enough depth. During my work on cluster tracing from Bonnell et al. (2013) simulations, I noticed a group of sinks, which could be a potential candidate of small OB association. In this chapter I investigate the formation of this association in terms of size, mass density, and energies.

7.1 The association

The cluster finder together with clusters of sinks also found some interesting objects appearing in the simulation. One of these could be a possible association. Figure 7.1 shows what looks to be a failed cluster formation scenario, which could be the origin of an OB association. The figure shows the movement of the sinks over all time steps in x - z positions relative to the centre of mass of the simulation. Before sink formation, protosink (protosink is the gas particle which is converted to the sink during the sink formation event) paths are shown as thin grey paths, while after sink formation, paths are coloured by simulation time.

The first sinks start forming around a time of 2 - 3 Myr in relatively isolated regions after the spiral shock compressed gas gravitationally collapses and forms first sinks. At around 3.5 - 4 Myr the entire group collapses into a compact cluster-like object (Figure 7.2), as the region becomes gravitationally bound. However, at later times the association starts to expand. Most

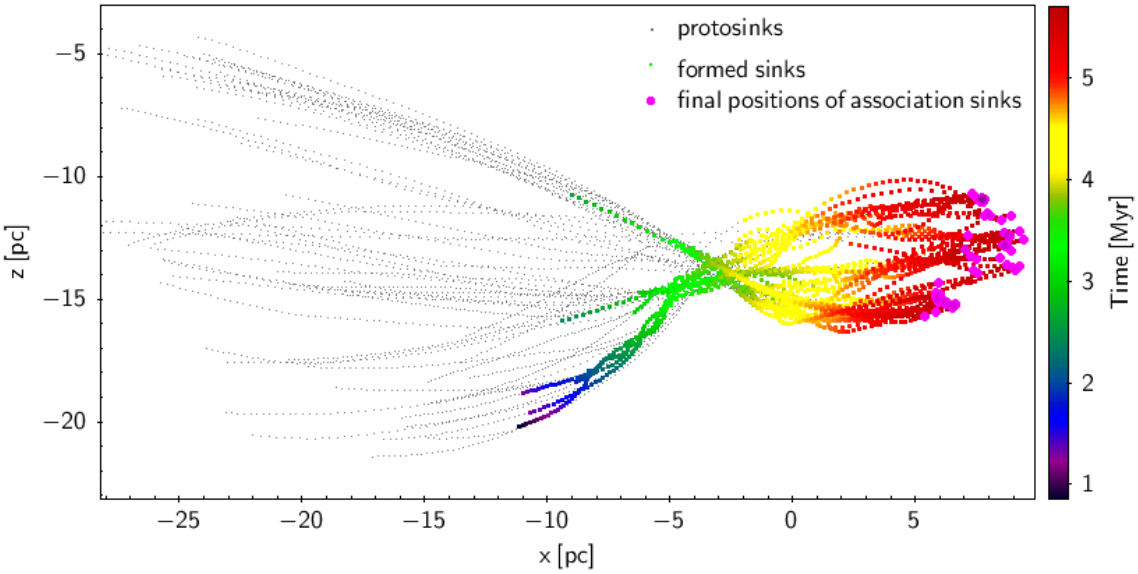

Figure 7.1: The association candidate or failed cluster formation is shown in the spatial map. The map is created by using particle positions in the x-z projection. Small grey dots show positions of protosinks and coloured dots show positions of formed sinks, colour coded by a given time. The system collapses before 4 Myr with first sinks forming at 1-2 Myr. After 4 Myr the system starts to expand. Around 5 Myr the object reaches its maximum size and it slightly reduces in the last 0.6 Myr. The expansion phase is not present in any other forming cluster in this simulation. The object could be the potential candidate of the forming OB association.

of the sinks are already formed at around 4 Myr when the object starts to expand. During the last Myr of the simulation, the object expands up to 5 - 10 pc in size. Sinks appear also to be grouped into 3-4 smaller groups during the last stages of the evolution of the association. It is likely that local gravitational collapse in these compact groups is faster than the global collapse of the object. Different sinks also pass through the maximum compactness point (where sinks occupies the highest concentration, i.e. at $[x = -3$ pc, $z = -14]$ pc in Figure 7.2) at slightly different times: there is around 0.5 Myr time difference between when the first sinks enter the maximum compactness region and the last sinks leave it.

One of the possible explanations for the expansion phase could be that tidal effects from neighbour sinks and clusters are stripping the association apart and triggering the expansion phase. If the pulling tidal force is comparable with the self-gravity force, the whole object can start to expand, and the centrally condensed stable cluster could not form.

7.2 Region morphology

In order to see if there are any particular features of this association, I plot in Figure 7.3 the positions and velocities of all sinks in the region where the association is found at the end of

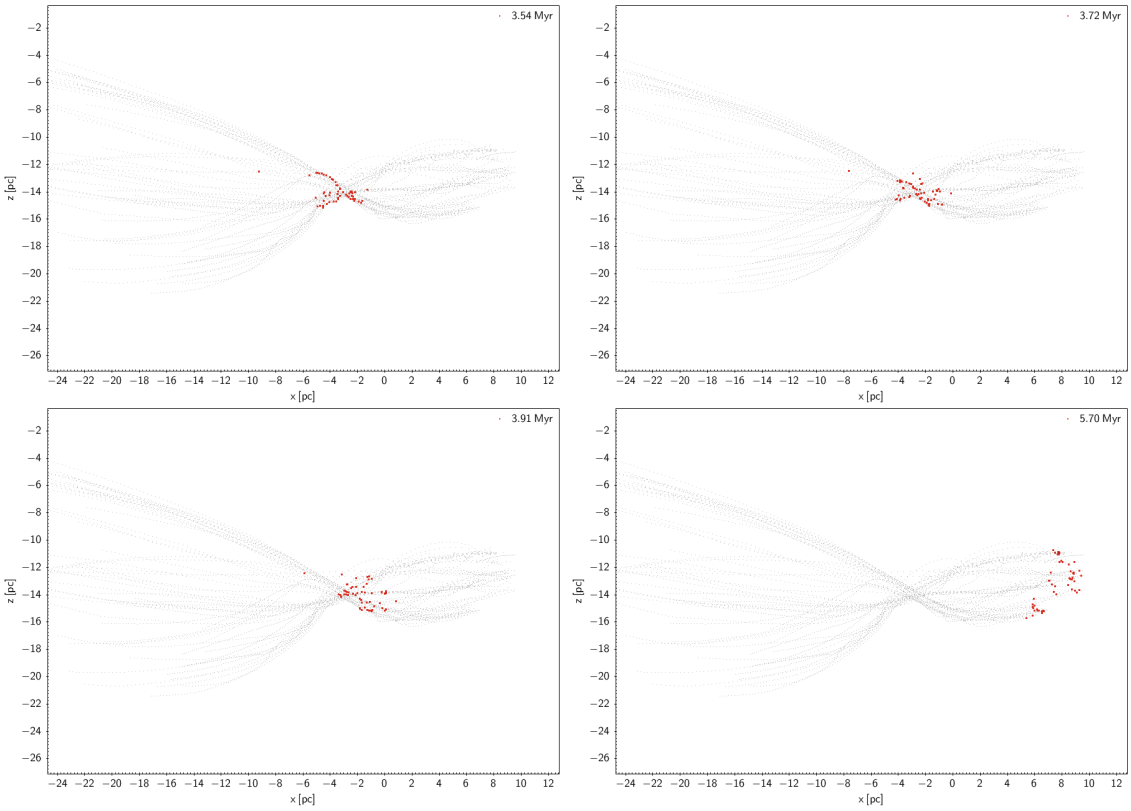

Figure 7.2: Evolution with expansion is shown for the association candidate at four different timesteps of the simulation. Movement paths for sinks and protosinks are shown each panel as grey dots. Red solid dots show positions of sinks at a given time. The top-left panel shows sink positions just before the maximum compactness, top-right at the maximum compactness, bottom-left just after maximum compactness and bottom-right at the end of the simulation. As the map shows, sinks pass through the maximum compactness point and continue to move along their paths when the association expands.

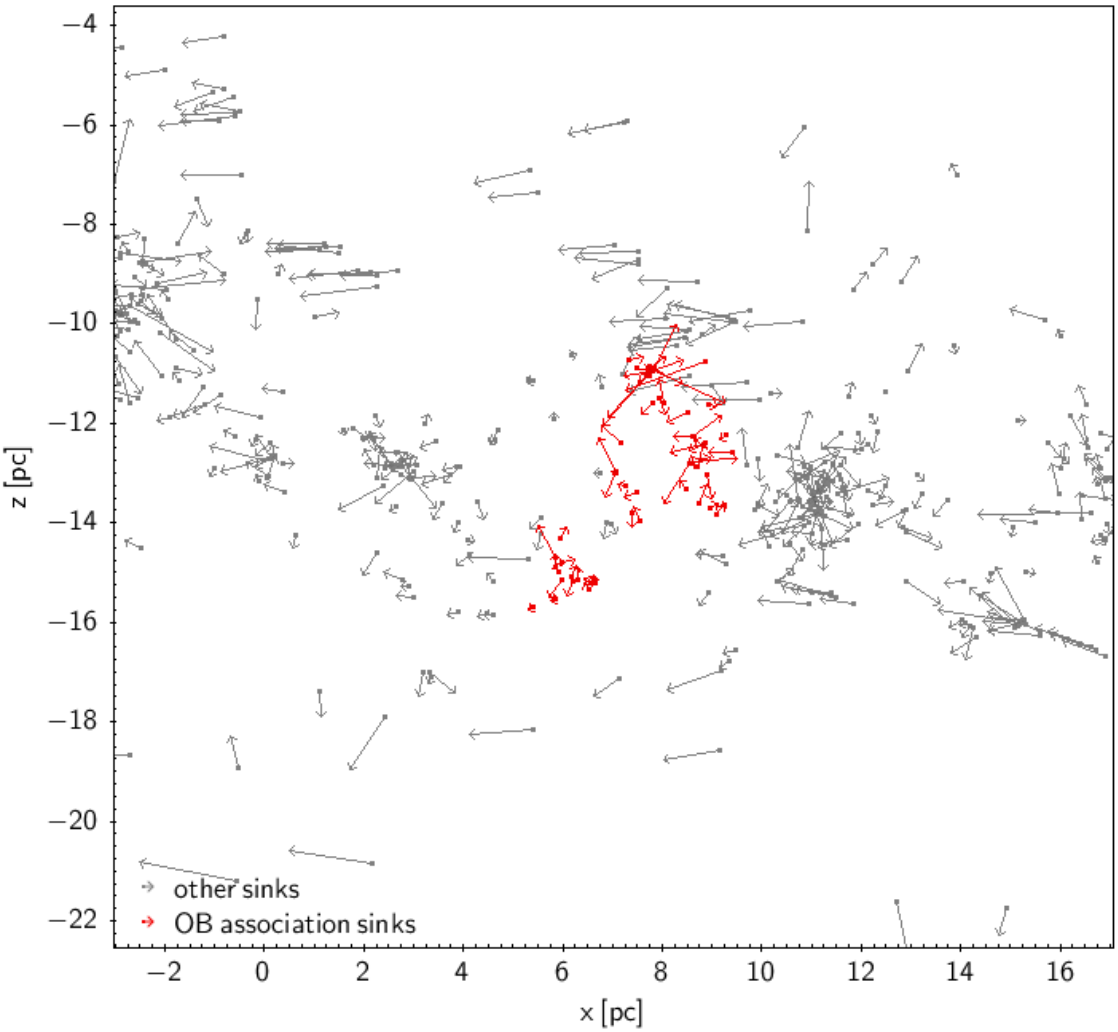

Figure 7.3: Distribution of the association members and their velocity vectors are shown at the end of the simulation (5.7 Myr). Association sinks are plotted as red dots, and other sinks as grey dots. The association is surrounded by other clusters and groups of sinks in the region. A cluster with a similar mass to the association is present just to the right of the association. Sinks which belong to the association are distributed in three compact subclusters. Sink velocities do not show visible systematic collapse or expansion of the system and are quite random. Subclusters and clusters in the environment show slightly larger velocities as sinks move in the local gravitational potential.

the simulation. The dots show positions of the sinks, while arrows show the velocities of sinks relative to the centre of mass of the association. Red colours in the diagram show positions and velocities for association sinks, while other sinks, which do not belong to the association, are marked in grey.

The region appears to be quite hierarchical, with many clusters and subclusters. There is one cluster visible just to the right of the association at [$x = 11$ pc, $z = -13$ pc]. There are several subclusters to the left of the association and the second most massive cluster in the simulation is just outside the left border of Figure 7.3. The distribution of association sinks itself appears to be loose, spreading to 3 - 5 pc. The central region of the association appears to be almost empty. Most of the association sinks are in 3 subclusters, with two of them visible at the upper part of the association and one at the bottom part. Velocities of sinks in the association does not seem to suggest any systematic trend to the collapse or expansion of the whole object and are quite random. Several sinks appear to be moving quite fast in the subcluster visible at [$x = 8$ pc, $z = -11$ pc] in Figure 7.3. At the end of the simulation, when Figure 7.3 is calculated, the object expansion appears to be stopped (Figure 7.2 lower right panel) as the object reached a maximum size.

7.3 Environment

In order to better understand the expansion phase in the association, I investigate the properties of the surrounding environment. I then compare the evolutionary properties of the association to other clusters in the area. I plot the region maps with highlighted OB and other cluster particles (Figure 7.4).

Figure 7.4 shows different viewing projections, with x-y in the left and x-z in the right hand side panels. The top panels show the region at the beginning of the simulation, the middle panels at 3.9 Myr, and the bottom panels at the end of the simulation. Grey dots in all plots show positions of all environment gas particles. Red small dots show gas particles remaining to be accreted in the association. Orange large points show the positions of formed association sinks. In a similar way I also plot the nearby 8300 $M_\odot$ cluster sink (cyan) and gas (deep blue) particles yet to be accreted. The second most massive cluster (25000 $M_\odot$) is also shown in terms of sinks (light pink) and gas (green) particles yet to be accreted. Scales in this plot at different times are set to be slightly different in order to show the large scale

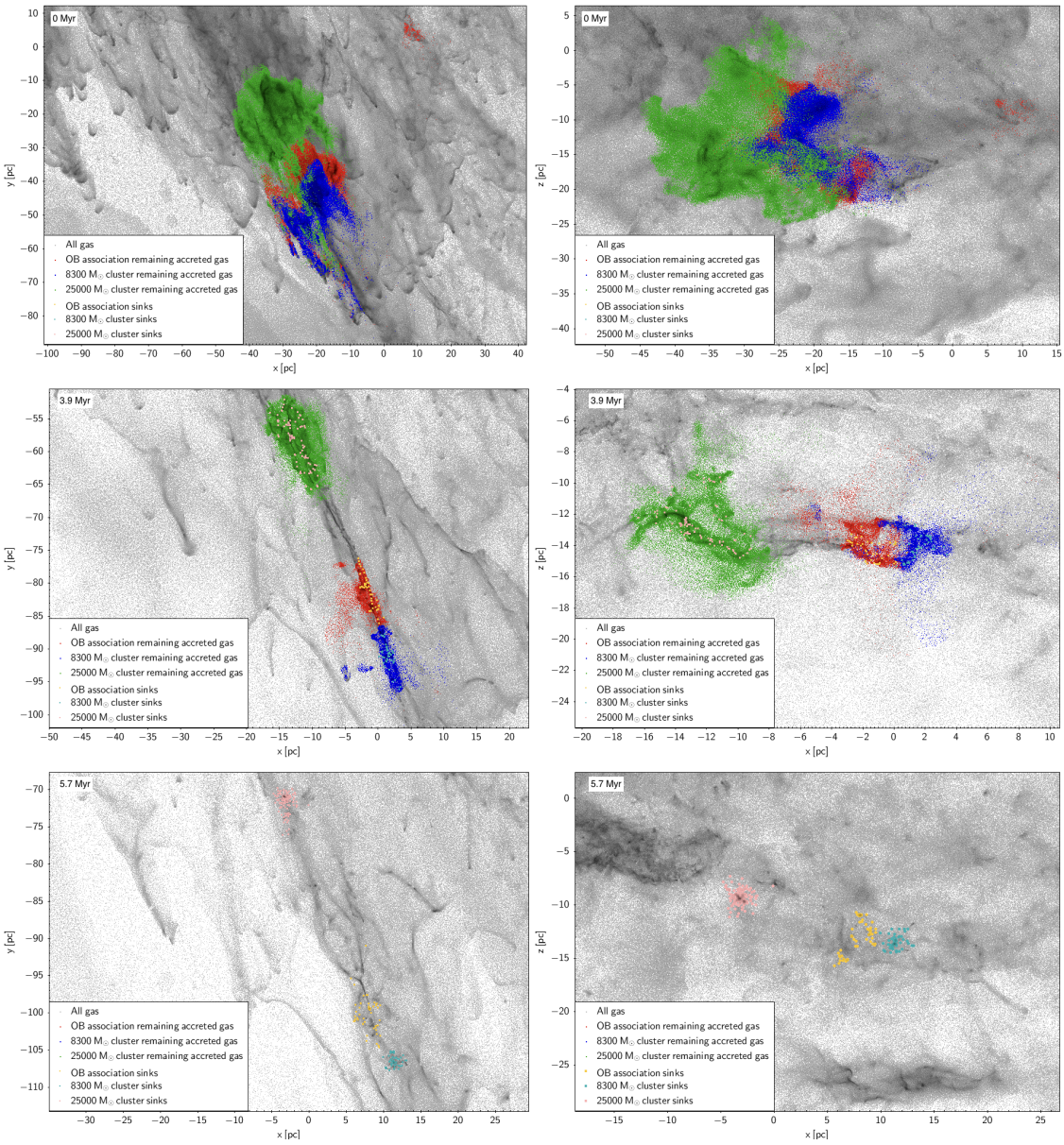

Figure 7.4: The maps showing the region of the association in two different projections and three different evolutionary stages: early, intermediate and late. The association and two other clusters remaining to be accreted gas and sink particles are plotted with separate colours. Grey particles represent environment gas particles. The plot shows that during the early times all three systems form in a similar way. However, the association shows that at the latest times it expands while other clusters reach their compact states.

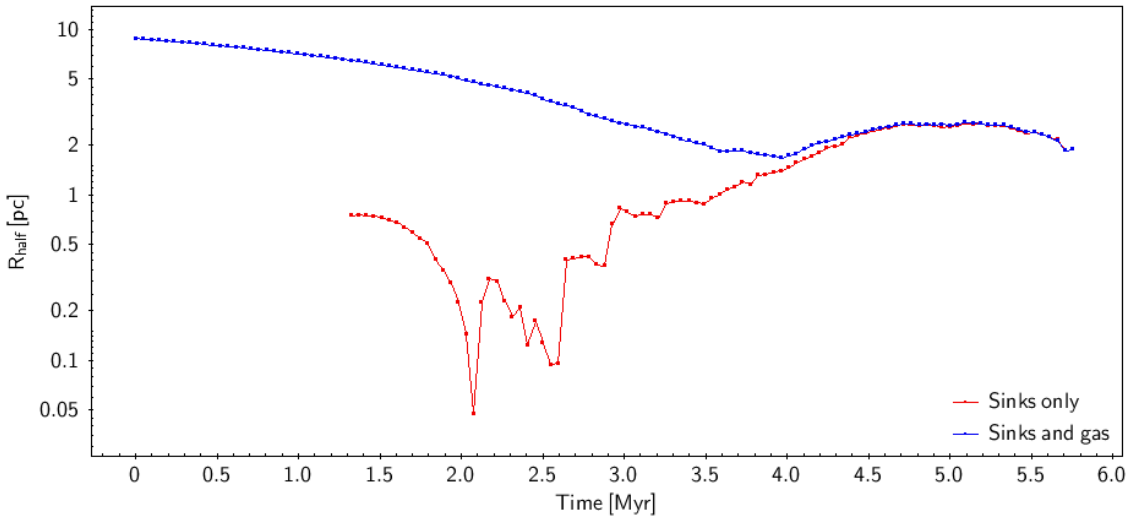

Figure 7.5: Evolution of half-mass radius of the association is shown for two subsets when using total mass for the first one (blue) and stellar mass only for the second one (red). Both half-mass radii show the expansion phase. The conserved mass case shows collapse of the cloud at early times and expansion starting from 4 Myr. The sinks only case is slightly different, showing expansion as early as starting from 3 Myr.

distribution of the cloud at the beginning of the simulation and small scale distribution of sinks at small scales at the end of the simulation.

The maps show that all three objects are collapsing during the evolution. The association appears to be almost indistinguishable from the other clusters. The only difference is the fast expansion phase from 3.9 Myr to the end of the simulation. During that phase, the association does not collapse into a centrally condensed cluster but instead expands. The most interesting are the middle panels at 3.9 Myr. A strange ring-loop is visible in x-z projection (middle-right panel in Figure 7.4). The left side of the ring is made from association particles, while the right side of the ring contains the 8300 $M_\odot$ cluster particles. This is not visible in the middle-left panel in Figure 7.4, as the ring is viewed edge-on. The ring-loop is most likely a tidally driven temporary structure, where the left side is being pulled out and expanding, and the right side collapsing into the cluster. Similar lens-shaped ring loops are also visible in gas particles at the bottom-left panel of Figure 7.4, which appear in inter-cluster regions. If that's the case, it could be common that if there is one cluster forming near another, that one cluster could tidally interrupt the collapse of the nearby cluster and turn it into association.

7.4 Half-mass radii

The half-mass radii give a good overview of the system. In Figure 7.5 I plot the evolution of half-mass radius for the association. The red line shows the half-mass radius calculated from the sinks already formed in the association. The blue line is calculated by using the full mass (sinks and gas) which comprise the final system. This ensures that the mass is conserved at all timesteps for the blue line, while the red line uses only stellar mass.

At the beginning of the simulation, there are no sinks yet formed, so the half-mass radius for purely stellar mass can't be defined, and only the conserved mass blue track is visible between 0 and 1.3 Myr (Figure 7.5). Even when the first two sinks form, the half mass radius is not defined. There need to be at least three sinks formed in the system and one sink can't be more massive than the rest of the mass in other members of the system. At 1.3 Myr association sinks finally satisfy the half-mass radius definition for stellar mass, which remains defined all the way to the end of the simulation.

Between 1.3 and 3 Myr, the half-mass radius for sinks is fluctuating (red line in Figure 7.5). The half-mass radius here always remains below 1 pc and twice reaches as low as 0.05 - 0.1 pc. These oscillations occur as a compact group of just several sinks formed during this time, and sinks are oscillating in the potential well of that cluster. After 3 Myr, the stellar half-mass radius no longer reduces and continuously expands until 5 Myr.

The conserved mass half-mass radius of the association between 0 and 4 Myr decreases from 10 pc down to 2.5 pc. This shows that the association collapses globally during this time. The first subclusters are forming as early as 1.5 Myr during the local collapse phase of the region. The half-mass radius decreases by a factor of nearly 4 over these 4 Myr. This is significantly less than seen earlier for the standard cluster half-mass radius reduction with a factor of 10 (as discussed in the previous chapter). The missing part of the collapse in the association is the final phase where instead the whole association starts to expand. Due to the expansion between 4 and 5 Myr, the association half-mass radius increases from 2.5 to 3.5 pc. Around 4 Myr, the stellar half-mass radius becomes nearly the same as the conserved mass radius due to the last sink formation and accretion taking place. Both radii start to decrease slightly again from 5 Myr to the end of the simulation, highlighting the complexities of the evolution.

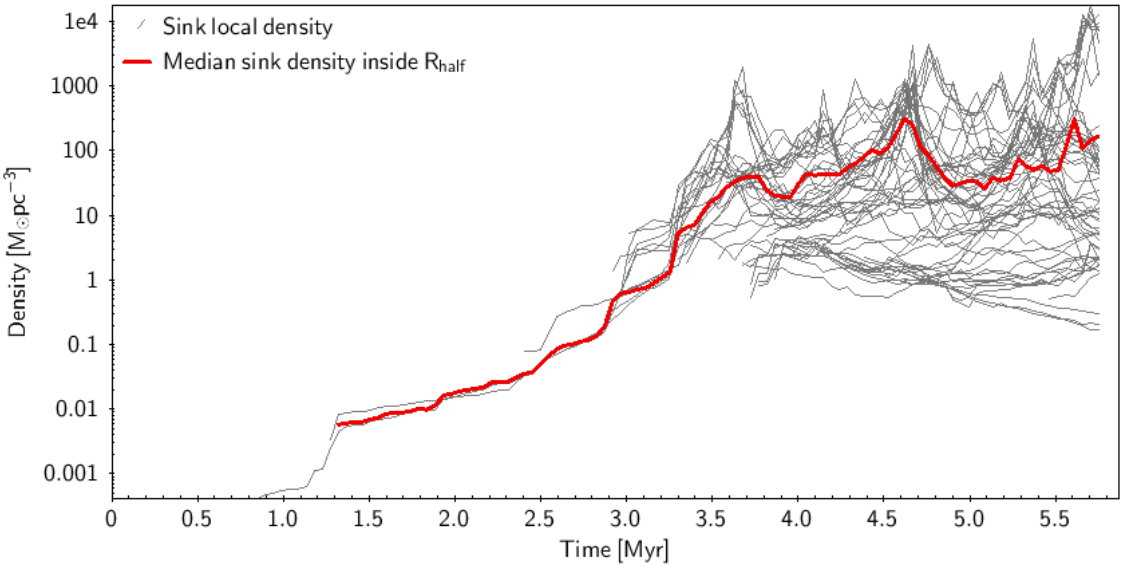

Figure 7.6: Evolution of association member sink local densities. Grey tracks show local densities of individual sinks from the association, while the red track shows the median density, calculated by using sinks inside the half mass radius. The plot shows that individual sink and median densities increase continuously before 4 Myr. After this time, median density continues to increase but slower. Some sinks at late times remain at high densities while others have decreasing densities as low as 1 - 10 $M_\odot$ pc^{-3}. The decreasing densities represent the expansion phase. However, sink densities in three subclusters remain large.

The evolution of the half-mass radius of the association shows that initial collapse is followed by a re-expansion after 4 Myr. Even if these two properties are interesting, they do not provide the reason for the starting of the expansion phase. Multiple physical processes could be the reason for the expansion, and one of them, in the absence of feedback, can be the tidal disruption.

7.5 Densities

The first physical property to trace over time would be the sink local density. Figure 7.6 shows the evolution of sink local densities for all association members over the simulation. Each grey line shows the evolution of an individual sink from its formation to the end of the simulation. Sinks are plotted from the time of their formation. The red line shows the evolution of the median density, calculated by using local densities from sinks which are within half-mass radius of the association.

Only a few sinks form earlier than 3.5 Myr. Between 3.5 and 4 Myr, there is an intensive burst of star formation, when most of the sinks, which belong to the association, are formed. This also happens when the maximum compactness of the association is reached. There are

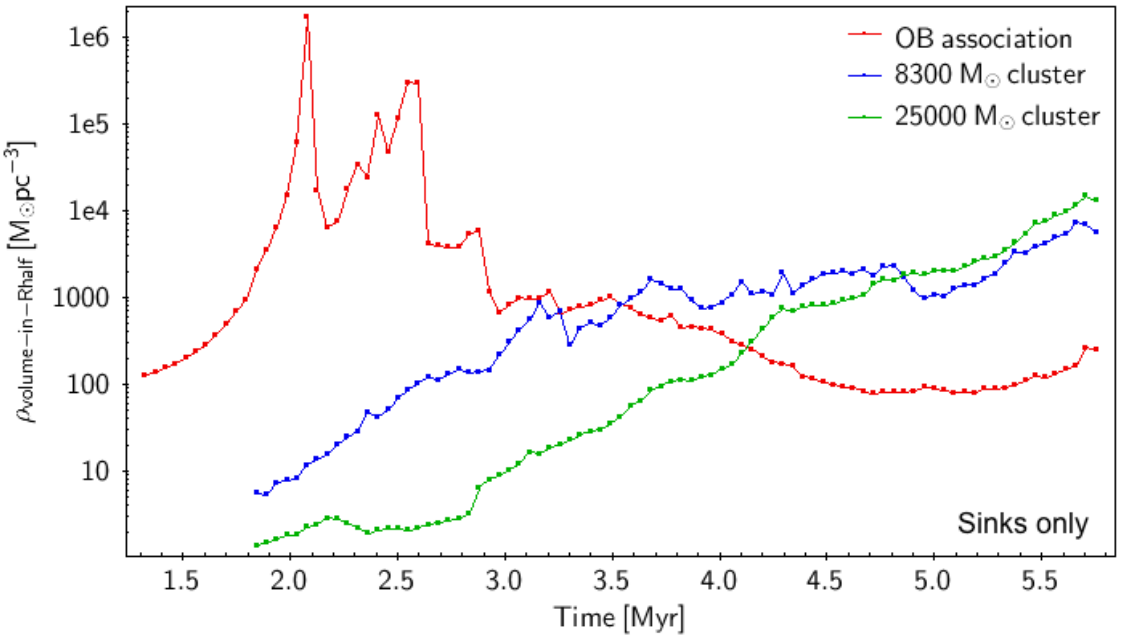

Figure 7.7: Evolution is shown for volume densities inside half-mass radii for the association and two other clusters. Half-mass radii and densities are calculated by using only formed sinks, which belong to the corresponding system. Volume densities for both clusters continue to increase. During the early stages the association has high volume densities but from 3.5 Myr volume densities start to decrease showing the expansion phase.

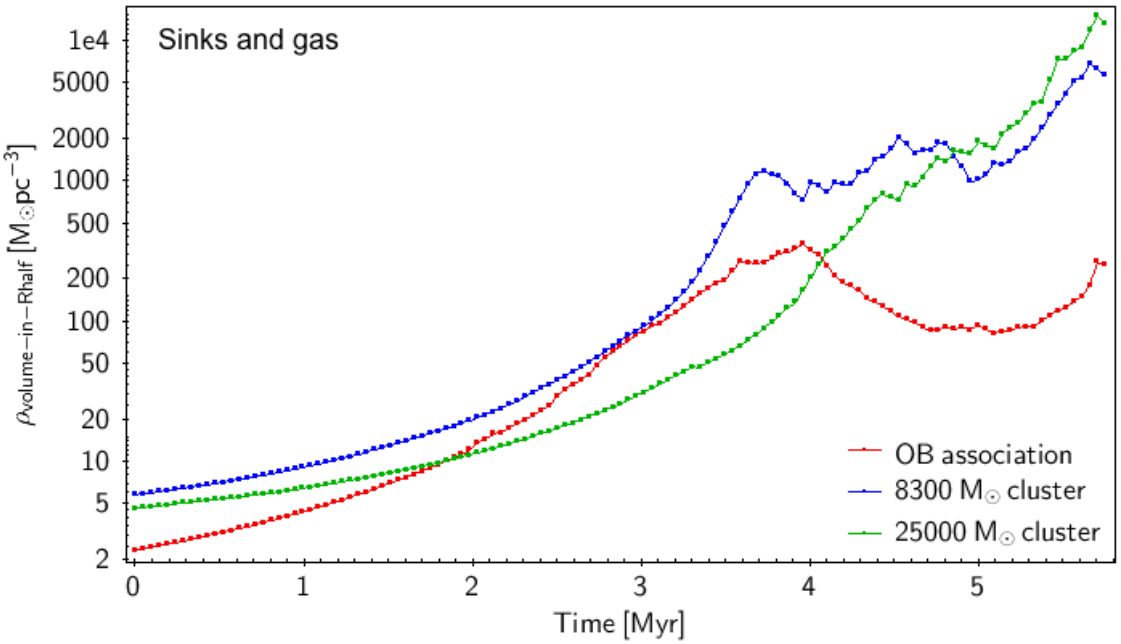

Figure 7.8: Evolution is shown for volume densities inside half-mass radii for the association and two other clusters. Half-mass radii and densities are calculated by using sinks and gas remaining to be accreted, which contributes to the forming system. The plot shows that densities are increasing for the two clusters in the simulation at all times. The density in the association continues to increase up to 4 Myr, which is slightly later than volume densities calculated by using sinks only (Figure 7.7).

several sinks at 3.7 Myr which reach local densities up to 1000 $M_{\odot}pc^{-3}$. At later times, sink densities do not increase very rapidly, as the whole association starts to expand. Some of the sinks decrease their density, which goes down to several $M_{\odot}pc^{-3}$ at the end of the simulation. The whole object expands, but there the subclusters, visible in Figure 7.3 form as local regions collapse, while the whole object expands. This is why there are visible multiple spikes between 100 and several 1000 $M_{\odot}pc^{-3}$ densities. Spikes form as these sinks oscillate (i.e. moving back and forth) in their subcluster potential well. These oscillations only occur for sinks, with densities above 100 $M_{\odot}pc^{-3}$. This shows that self-gravity becomes dominating at these density regimes.

In Figures 7.7 and 7.8 are shown volume densities from half-mass radii calculated for the association and two other clusters. In Figure 7.7 only sinks are used, while Figure 7.8 also includes the gas particles remaining to be accreted. The association sink volume densities show a decrease between 2.5 Myr and 5.0 Myr while the two other cluster densities systematically increase at all times. The association volume density is as high as 10^3 - 10^6 $M_{\odot}pc^{-3}$ before 3 Myr as there is a compact subcluster formed at this time. From 3 Myr to 5 Myr, the sink volume density of the association decreases from 1000 $M_{\odot}pc^{-3}$ down to 100 $M_{\odot}pc^{-3}$ as the expansion phase takes place. The two other cluster's sink volume densities are increasing all the time from 2 Myr to 5.7 Myr.

Even though the densities of the association decrease rapidly, they do not reach observed values of 0.1 $M_{\odot}pc^{-3}$ in Milky Way OB associations. Such densities are not resolved in this simulation due to the sink low mass limit (11 $M_{\odot}$). It could require longer time scales in order to allow the OB association to expand further to reach 0.1 $M_{\odot}pc^{-3}$. As a result it could be correct to call this object a "failed cluster" rather than a "true OB association". However, the formation mechanism of this object can be as the real OB association. Thus I continue to call this object the association in the rest of this chapter.

7.6 Tidal force

Tidal force on cluster members can occur as a result of gravitational interactions between cluster members and the surrounding environment. However, it is not straightforward to correctly calculate tidal forces on the cluster members. Here I will describe the simple vectorial way of calculating tidal forces on cluster particles.

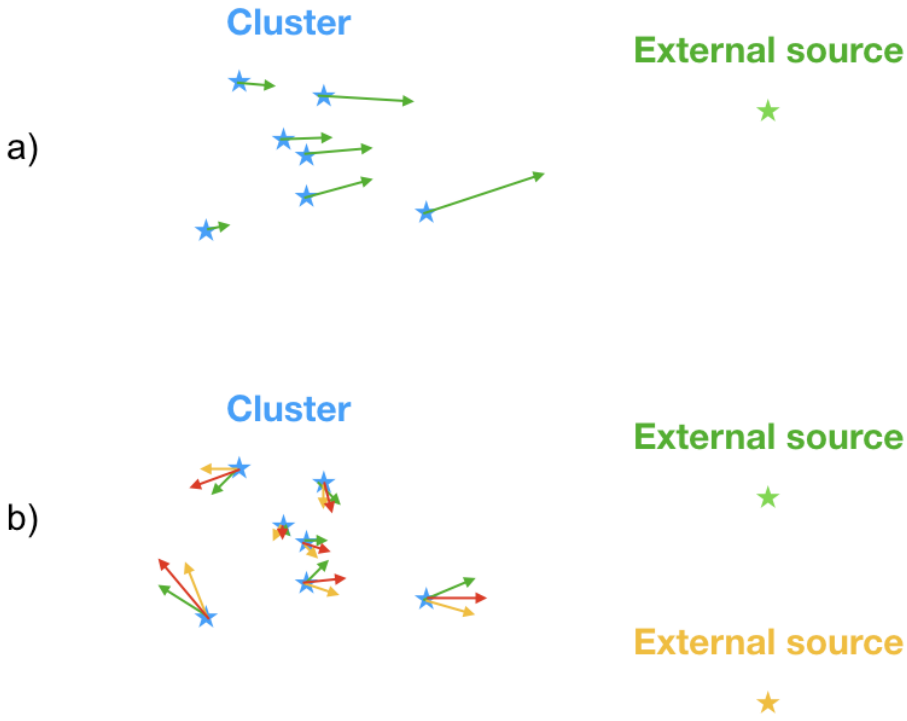

Figure 7.9: The sketch shows how tidal forces can be defined for clusters. Firstly gravity force on each cluster member is calculated separately from the external source. The mean force of all members is then subtracted from all external gravity forces calculated for each cluster member. Finally these calculations are repeated over all external sources and added in a vectorial way to get final tidal force vectors for each sink in the cluster. Forces in the front and opposite side of the cluster facing external source are expansive, and at 90 degrees, compressive. This leads that cluster to experience "spagetificaltion" if there are external gravity sources in a particular direction. The sketch allows us to understand tidal force on particle systems and calculate tidal forces for all sinks in the current example of the association, and investigate if tidal effects are responsible for the expansion phase.

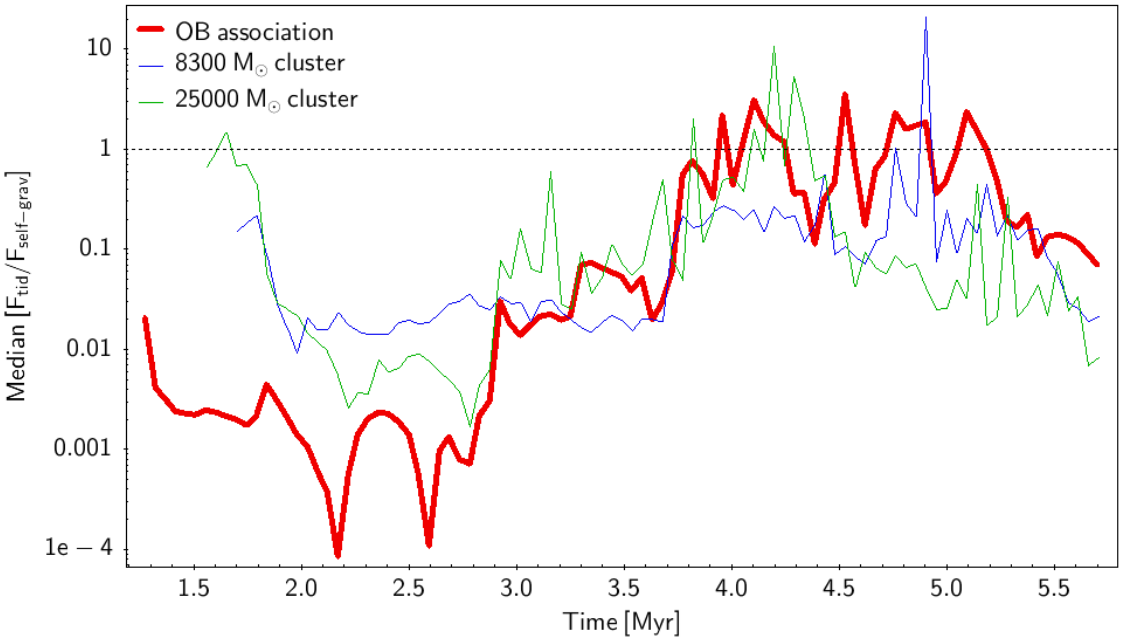

Figure 7.10: Evolution of the median ratio is shown between tidal force and internal self-gravity force for the association and two other clusters by using sinks only. Ratios begin after 1 Myr as before there are not enough sinks formed in order to calculate these ratios. The plot shows that tidal force for the association exceeds self-gravity force most of the time between 4 and 5 Myr. While other clusters also show force ratios above 1, they last for a short period of time. As the association remains under strong tidal forces for around 1 Myr, it is likely that tidal forces trigger the expansion phase.

Firstly the gravity force vectors from each of the cluster members to the external source (another sink which does not belong to the cluster) are calculated ((a) case in Figure 7.9). These vectors are pointing towards the external source. Then the mean force is calculated as the zero-force of the cluster. This mean force is then subtracted from each cluster member's external gravity force in order to calculate the tidal force felt by each cluster member (in Figure 7.9 tidal forces from the green source are shown as green arrows (b)). As a result, tidal forces on stars, which are at close or distant points in the cluster, will be pointing away from the cluster centre. And the points, which are at the 90 degrees sides of the cluster, will have a compressing tidal force. As a result, a cluster will be stretched and get a slightly extended shape. If there are multiple external sources, their tidal forces can be calculated independently by calculating external gravity force first and subtracting the mean force over all members. In Figure 7.9 (b) yellow arrows show tidal force vectors, caused by second (yellow) external source. The final tidal force on each cluster member is found by summing all tidal vectors for each external source (i.e. red arrows show the averaged tidal force from two external sources in Figure 7.9 (b)).

I used this tidal force definition in order to calculate tidal forces and compare them with the

internal self-gravity force for the association as well as for two neighbour clusters (Figure 7.10). The ratio, of self-gravity and tidal forces, is calculated on each sink particle. The magnitudes of self-gravity and tidal forces vectors are used, so the ratio at each sink is never negative. In order to combine the forces ratio to account the effect on the whole object (association or cluster), I use the median of all object sinks force ratios.

The plot shows that for the association, as well as for the two clusters, ratios are below one at early times before 3.5 Myr. After 4 Myr, the force ratio for the association (red line in Figure 7.10) is oscillating around one. There are also several timesteps, where the 8300 $M_\odot$ and 25000 $M_\odot$ clusters have tidal forces slightly larger than self-gravity. For the 8300 $M_\odot$ cluster this happens at 4.9 Myr, while for the 25000 $M_\odot$ cluster at 4.3 Myr. However, tidal forces on these clusters are larger than the self-gravity force for only about 0.1 - 0.3 Myr, while for the association this happened for more than 1 Myr. In the case of these two clusters, the tidal effects were present for a short period of time and didn't cause the tidal disruption. For the association the tidal force acting over 1 Myr has a sufficiently long enough time to move the association sinks outwards, and thus the whole system experienced significant tidal disruption.

7.7 Energies

Energies are the key properties describing the state of the cluster. There are three primary energies - gravitational, kinetic and tidal. The gravitational energy is calculated by summing over all cluster member pairs. We can also use a spherical gravitational energy approach, where the whole cluster mass is placed in the cluster centre of mass and individual member distances are used to the centre of mass rather than between pairs. Spherical gravity also allows us to avoid close binaries, which have most of the gravitational energy. In contrast, it is not the best option for filamentary clusters. While association is not spherical, the direct summation would be dominated by compact subclusters and binaries and therefore not highlight how these subclusters are bound to each other. The spherical approach is better for describing of how subclusters are bound to each other. As a result, I use the spherical approach here.

The kinetic energy of the cluster is simply a summation of individual sink kinetic energies, calculated by using sink velocities relative to the cluster centre of mass velocity. Comparing the kinetic and gravitational energy tells us if the cluster or association is bound.

We can also calculate the tidal energy for each cluster member. This is a dot product

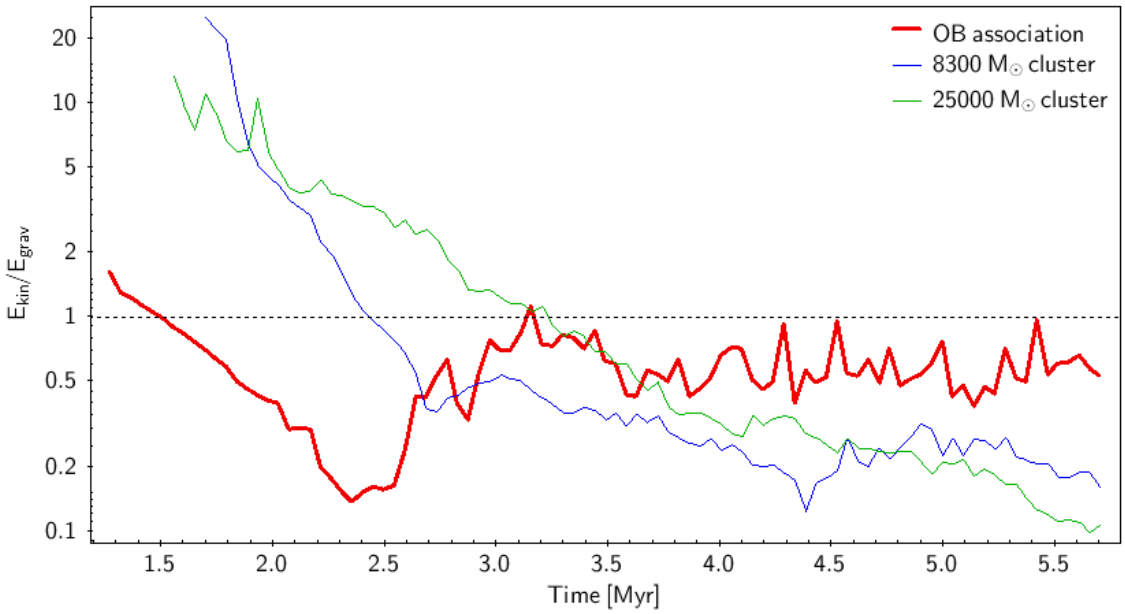

Figure 7.11: Evolution of boundedness states, which includes kinetic and gravitational energies, is shown for formed sinks in the association and two other clusters. Gravitational energy was calculated by using the spherical approach with the centre of mass of the cluster rather than the direct summation over sink pairs. The dashed line shows binding ratios of one, i.e. systems which are above the line are gravitationally unbound while systems below the line are bound. At early times the two clusters are gravitationally unbound. They become bound at 2.5 - 3.5 Myr of the simulation time. The association remains bound from 1.5 Myr all the time till the end of the simulation. However, the association is less bound than two other clusters after 3.5 Myr. As the association appears to be bound, kinetic energy alone is not high enough to explain the expansion phase.

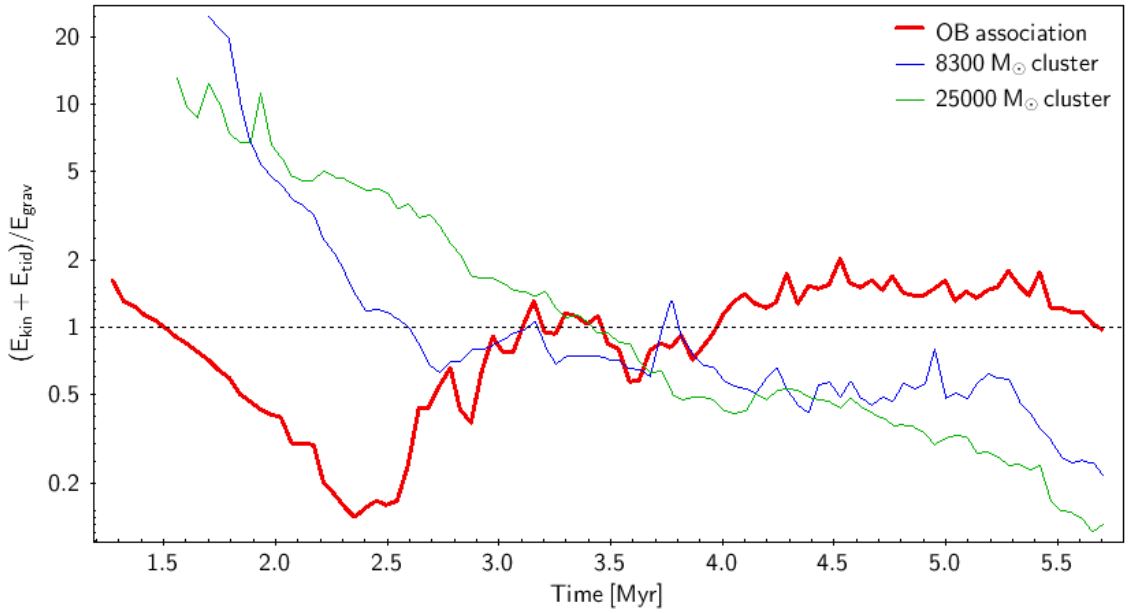

Figure 7.12: Evolution of boundedness states, which includes kinetic, gravitational and tidal energies, is shown for formed sinks in the association and two other clusters. The plot is the same as in Figure 7.11 with the exception that tidal energy is added to the calculations of binding ratios. While the two clusters become bound and show nearly the same evolution of binding ratios as in Figure 7.11, the association becomes unbound at 4 Myr and remains unbound until the end of the simulation. As at this time the expansion phase is happening, tidal energy is likely to be responsible for the expansion phase.

between the tidal force vector and centre of mass radius vector, i.e.

$$E_{\text{tid}} = |\mathbf{R}_{\text{CoM}} \cdot \mathbf{F}_{\text{tid}}| \tag{7.1}$$

The force here is calculated on each sink by using the method described in the previous section. The tidal energy of the whole cluster is just a summation over the tidal energies of individual cluster members. In order to describe the full tidal energy for the cluster, the equation can be rewritten as:

$$E_{\text{tid}} = \sum_{i}^{\text{int}} \left| \mathbf{R}_{i,\text{CoM}} \cdot \mathbf{F}_{i,\text{tid}} \right| = \sum_{i}^{\text{int}} \left| \mathbf{R}_{i,\text{CoM}} \cdot \sum_{j}^{\text{ext}} (G \frac{m_i m_j}{|R_{ij}|^2} \frac{\mathbf{R}_{ij}}{|R_{ij}|} - \mathbf{F}_{j,\text{ext-mean}}) \right| \tag{7.2}$$

The first summation, with i indices, is running over the internal particles. The summation over j is summing over the external particles. The last term in Equation (7.2) $\mathbf{F}_{j,\text{ext-mean}}$ is the mean gravity force from external source j calculated for the cluster.

Another way to calculate the tidal energy for individual internal and external particles can be expressed in the following way:

$$E_{\rm tid} = G \sum_{i}^{\rm int} \sum_{j}^{\rm ext} \frac{m_i m_j}{|R_{ij}|} \frac{|R_{i,\rm CoM}|}{|R_{ij}|} \tag{7.3}$$

The multiplier $\frac{|R_{i,\rm CoM}|}{|R_{ij}|}$ here is the scaling factor, which tells how close cluster particle i is to the centre of mass of the cluster, rather than to the external particle j. However, equations (7.2) and (7.3) can become dominated by close pairs (or binaries) due to R_{ij}.

The third way uses spherical approach for the tidal energy of the cluster in a similar way as the gravitational energy:

$$E_{\rm tid} = G \sum_{j}^{\rm ext} \frac{M_{\rm clust} m_j}{|R_{j,\rm CoM}|} \frac{R_{\rm clust-half}}{|R_{j,\rm CoM}|} \tag{7.4}$$

Here $R_{\rm clust-half}$ is the cluster half-mass radius and $M_{\rm clust}$ is the cluster total mass. This calculation assumes that the cluster is spherical and that tidal forces from particle j affect the cluster with its characteristic size of $R_{\rm clust-half}$. Tidal energy calculated this way no longer suffers from close binaries. As a result, the $E_{\rm tid}$ evolution, calculated in the spherical way, is less noisy over time and thus I use it together with the $E_{\rm grav}$ calculated in the spherical way.

In all three equations tidal energy is calculated by assuming that tidal forces are expansive. Tidal forces can be compressive. In further analysis I use only the expansive component of the tidal energy.

The ratio between compressive and expansive energies defines the binding of the cluster. In the case of gravitational ($E_{\rm grav}$), kinetic ($E_{\rm kin}$) and tidal ($E_{\rm tid}$) energies, this ratio can be written as follows:

$$\text{Binding ratio} = \frac{E_{\rm kin} + E_{\rm tid}}{E_{\rm grav}} \tag{7.5}$$

If the tidal energy is not used, then $E_{\rm tid}$=0.

In Figures 7.11 and 7.12, I plot binding ratios as a function of time for the association and two other clusters. The association is marked as red, the 8300 $M_\odot$ cluster as blue, and the 25000 $M_\odot$ cluster as green lines. The difference between Figures 7.11 and 7.12 is that Figure 7.11 shows binding ratios calculated by just using kinetic and gravitational energies, while in Figure 7.12 to the kinetic energy is added the tidal energy of the cluster (calculated in the

spherical way).

Figures 7.11 and 7.12 show that binding ratio tracks start from the point at which first association sinks form (at 1.3 Myr). The association always appears to be bound when using just kinetic energy. However, it is less bound than the other two clusters at later times (after 3.7 Myr), where expansion begins. The association also does not show any signs of significant decrease in binding ratios, while the two other clusters show a decrease. When tidal energy is added to the kinetic (Figure 7.12), the binding ratio of the association increases significantly and makes the association unbound. The association remains unbound between 4 and 5.5 Myr. Other clusters do not show significant increasing in the binding ratio. This means that due to tidal effects, the association becomes unbound and starts to expand, while the two clusters keep similar small binding ratios. As tidal energy has such significant impact, gravitational collapse is halted, and the cluster fails to form. The association forms instead.

7.8 Summary

In this chapter I investigated a rare object forming self-consistently in simulations, which is likely to be a candidate for an OB association, and thus reveal mechanism of how OB associations could be forming. The object is collapsing in space during the first 4 Myr of its evolution. From 4 to 5 Myr of the simulation time, the object expands about 2-3 times in its size and remains nearly the same size for the remaining 0.6 Myr. Maps with gas particles at multiple timesteps show that the association is forming nearby another cluster, which successfully forms by the end of the simulation. At 3.9 Myr the cluster and the association form an interesting ring shaped object from their gas particles remaining to be accreted. The association appears as three small subclusters, spread within 3-4 pc volume at the end of the simulation. Individual sink velocities are random and slightly larger in subclusters. However velocities do not show significant systematic movement.

The expansion phase is clearly visible in terms of half-mass radii calculated in both cases - sinks only and sinks with remaining to be accreted gas particles. Sink local densities show that individual sink densities increase before the expansion phase. Around 3.5 - 4 Myr the association reaches maximum compactness and a large number of sinks form. Some sinks from sub-clusters show large local densities but others show low local densities. Comparison of volume densities between the association and two other clusters shows significant differences.

This occurs in terms of a decreasing association volume density over the last 2 Myr while the other clusters volume densities increase.

The formation of this association is most likely to be affected by tidal forces. I discussed how tidal forces can be calculated at each cluster member from external source. Calculations for the association and two comparison clusters show that median tidal force for association exceed self-gravity force for the duration of 1 Myr while the clusters show only short time intervals (i.e. around 0.2 Myr). Furthermore, the association is less gravitationally bound than the two comparison clusters at late times when using just kinetic and gravitational energies in boundedness calculations. The association becomes unbound if tidal energy is added to the kinetic energy when calculating binding ratios while other two clusters remain bound.

8

Conclusions and future work

Here I discuss my final conclusions of this thesis. I summarise all chapters to review new findings on star and stellar cluster formation, collapse triggering mechanisms and formation of OB associations.

8.1 Star formation

Star formation is the major problem in astronomy, investigating how material is turned from gas to stars. It is known that star formation occurs in molecular clouds, where high density clumps collapse thanks to self-gravity.

In this thesis I looked into the details of how high density clouds are compressed to the high density at which star formation is triggered. This occurs at the edge of galactic spiral arm, where low density inter-arm material is collides with high density arm material, creating the spiral shock on galactic scale. Analysis of Bonnell et al. (2013) simulations shows that the pre-shock gas comes with around 30 km/s velocity, relative to the post-shock gas in a Milky

Way like galaxy. As regions are compressed, they become gravitationally unstable and start to collapse. As a result, the main ridge of high density gas in the simulation becomes a massive star forming region with dozens of clusters.

As star formation in smoothed particle hydrodynamics (SPH) simulations is treated through sink particles, sink formation events are the crucial moments when stars are forming. As a result, there form sinks with different masses, where low mass sinks are bound locally and gain most of their final mass through sink formation, while high mass sinks are bound on larger scales and accreted their large mass from these scales.

Tracing of accreted gas particles shows that star forming gas comes from both high and low densities. Investigation of depletion and star formation times shows that star formation in high density regimes is dominated by self-gravity driven collapse of cores and clumps. Low density material can't be driven on reasonable timescales by self-gravity to reach their sinks and are assisted by the galactic shock instead. Star formation shows significant continuous accretion over several Myr, which could be reduced in the presence of feedback from stars.

8.2 Formation of stellar clusters

Since Lada & Lada (2003) proposed that most of the stars in the Milky Way should have formed in stellar clusters or OB associations, cluster formation became the major problem in terms of understanding star formation. I used the same Bonnell et al. (2013) Gravity simulation to investigate stellar cluster formation and evolution.

In order to find clusters, I wrote and discussed a cluster finding algorithm, which uses a gravitational potential based definition. This way, clusters are found in locations where are deep potential wells, formed by large groups of sink particles. The cluster finder also traces clusters over multiple timesteps of the simulation and allows us to reconstruct cluster merger tree as well as determining cluster lifetimes.

Clusters in the Bonnell et al. (2013) Gravity simulation form in the main star formation region. However, clusters do not necessarily overlap with the highest gas density locations. Individual sinks, which form early, move in the cluster gravitational potential towards the cluster centre and continue to accrete gas particles along their paths. This helps to increase stellar age spreads in clusters. Merging subclusters, which formed in different environments with different star formation times, also increase stellar age spreads.

Various cluster physical properties were also traced over time. Cluster density profiles show that the radial density decreases exponentially outwards with the power law index of -3.2. Cluster mass merger tree shows that cluster masses increase over time and most massive clusters benefit from merging more efficiently than less massive clusters. Massive clusters also show longer lifetimes, determined by tracing clusters over multiple time steps. Mass-radius relation shows that more massive clusters are also larger in their sizes. Clusters also have their angular momenta. Specific angular momentum is higher for massive clusters than for low mass clusters, as these clusters have formed from larger scale collapse than low mass clusters, bringing larger angular momentum from large scales. Massive clusters have massive deep gravitational potential, capable to accrete environment gas and gain more gas mass accretion directly inside clusters than low mass clusters.

8.3 Formation of OB associations

OB associations are known as loose objects, and have no proper explanation of their formation mechanisms. In the same simulation, which I used to investigate star and cluster formation, is present a unique object, which at early times collapses like a regular cluster but later expands to larger scales. Results show that the expansion phase can be explained by tidal forces from the surrounding environment. Tidal energy added to the kinetic energy makes the OB association unbound, while two comparison clusters remain bound.

8.4 Future plans

The opportunity to work with numerical simulations has highlighted very interesting details about star formation and clustering in the galactic environment. But it has also brought multiple new directions to work on in the future.

8.4.1 High-resolution simulations

Galactic scale simulations, such as Bonnell et al. (2013) do not resolve individual stars. In order to resolve stars and possibly protoplanetary discs, higher resolution simulations are needed. Higher resolution for a given region can be achieved by separating the region and splitting each simulation particle into a number of smaller particles. The basics of both processes have been implemented but requires future work. The separation method is using accreted particles in the cluster of interest, and finds other contributing environment particles as

well. The splitting method uses randomly distributed children particles within parent particle kernel with kernel function weights. Velocities were also randomly distributed for children particles based on velocity dispersion in the region. More future work requires better comparison with other particle splitting methods.

Resolution tests allowed us to resolve initial mass function in highest resolution simulation peaking at 1 $M_{\odot}$ and reaching sink masses down to 0.3 $M_{\odot}$. The slope of this mass function is -1.0. Highest resolution simulation also resolved accretion disc around one sink. Other resolution effects includes better resolved shocks and larger number of sinks forming in simulations at a given time. In future work dependencies between accretion radii, particle masses and resulting sink formation and accretion could be discussed. Comparison between different resolution simulations should show the best way of designing simulations which would resolve individual stars and inherit initial conditions from spiral arm simulations.

8.4.2 Magnetic field role in star and cluster formation

Magnetic fields are likely to effect star formation due to the magnetic freezing effect and thus are important in understanding early phase of star formation. Several test simulations were set which can be used in future to investigate magnetic field and resolution effects on star formation. First results shown that magnetic field magnetically freezes the collapsing clump, delaying the overall star formation process.

Further investigation is needed in order to understand how sink formation and accretion is dependent on the magnetic field strength and how effects scale with resolution.

8.4.3 Feedback from stars and SNe

Ionising feedback from formed stars can heat up gas in the local region and cause the gas to expand. Stellar winds can inject the momentum into surrounding gas. This feedback from massive stars can push away surrounding material and reduce accretion after 1 - 2 Myr. It was shown that feedback clears cluster environment and leaves it less bound and less massive over longer times (Dale et al. 2007; Dale & Bonnell 2008; Dale et al. 2012, 2014, 2015). How this works with clusters forming in Galactic environment remains unclear. Implementations of feedback could be used in cluster formation SPH simulations discussed through this thesis (i.e. feedback methods from Dale et al. 2007; Dale & Bonnell 2008; Dale et al. 2012, 2014, 2015). SN feedback should come out slightly later - starting from 2-3 Myr, when O stars with

the intensive feedback have cleared most of the environment. However, SN events are much more dramatic and they may have greater effects on larger scales, including neighbouring clouds. Lucas et al. (in prep.) implementations of SNe feedback in sphNG can be adopted in my cluster simulations. This should allow us to investigate effects of three types of feedback, i.e. ionisation, stellar winds and SNe, as well as combined effects between them.

8.4.4 Combining magnetic fields, feedback and resolution

While most of simulations are designed to target just one effect (i.e. magnetic fields, radiation or SN feedback, i.e. Soler et al. 2013; Dale et al. 2005, 2007; Dale & Bonnell 2008; Bate et al. 2014), real star forming clouds undergo all these effects at the same time. The question here is how do these effects add up. Each effect can be dominant at a particular evolutionary stage, so they may not necessarily add up in a linear way. For example if there are strong magnetic fields present in the simulation, stars might be forming less massive before feedback starts clearing the environment, leading to a weaker effect from feedback. In order to answer these questions, simulations could be set with the same parameters (in order to be cross-comparable) and just one, another and multiple effects enabled on each run.

8.4.5 Synthetic observations

Synthetic observations have recently been developed, allowing us to calculate more realistic maps of star forming regions (i.e. Koepferl et al. 2016a,b,c). These maps can be calculated for clusters forming in the galactic environment. Extracted properties (such as PDFs, star formation rates, etc.) can be compared with the ones known from observations. As this synthetic observations technique was used for Dale simulated clusters (i.e. from SPH simulations), the same technique can be re-used for my highest resolution simulations, which includes galactic cloud formation.

8.4.6 Relations between 2D and 3D

In addition to synthetic observations, a large number of projected maps can be made for clusters and clouds. The question here is how much observations is missing due to projected view, where multiple clusters from completely different regions could be overlapping on each other along the line of sight. When two clusters overlay along the line of sight, stars from both clusters appear in one direction as they would be in a single cluster, meaning that 2D cluster

finding algorithms may find different results than would be obtained in 3D. Another thing is how much cluster definition varies on the same cluster when it is viewed from different directions.

The same problem exists for blending multiple clouds along the line of sight. In such cases column densities of two overlapping clouds could add up and lead the observer to misinterpret the result.

8.4.7 Angular momentum and origin of discs

Cluster simulations show that cluster net rotational energy is only 1 - 20 % of total kinetic energy and that cluster angular momentum vectors are oriented to random directions. How this picture changes when scaled down in order to resolve individual star protoplanetary discs, and are the rotation vectors of discs and distribution of disc to star mass totally random for different cluster stars, are key questions here.

8.4.8 Gaia

In upcoming years Gaia should bring unprecedented 3D mapping of field stars and clusters in the solar neighbourhood. This should narrow the gap between simulations and observations. For the first time it should be possible to better compare position and velocity distributions between simulated and real clusters.

Bibliography

Ambartsumian, V. A. 1949, Astron. Zh., 26, 3

——. 1955, The Observatory, 75, 72

André, P., Di Francesco, J., Ward-Thompson, D., Inutsuka, S.-I., Pudritz, R. E., & Pineda, J. E. 2014, Protostars and Planets VI, 27, 1312.6232

André, P. et al. 2010, A& A, 518, L102, 1005.2618

Barnes, J., & Hut, P. 1986, Nature, 324, 446

Bastian, N. 2013, in Astronomical Society of the Pacific Conference Series, Vol. 470, 370 Years of Astronomy in Utrecht, ed. G. Pugliese, A. de Koter, & M. Wijburg, 287, 1208.3403

Bate, M. R. 2012, MNRAS, 419, 3115, 1110.1092

Bate, M. R., Bonnell, I. A., & Bromm, V. 2003, MNRAS, 339, 577, astro-ph/0212380

Bate, M. R., Bonnell, I. A., & Price, N. M. 1995, MNRAS, 277, 362, astro-ph/9510149

Bate, M. R., Tricco, T. S., & Price, D. J. 2014, MNRAS, 437, 77, 1310.1092

——. 2017, MNRAS, 465, 2714

Benz, W. 1990, in Numerical Modelling of Nonlinear Stellar Pulsations Problems and Prospects, ed. J. R. Buchler, 269

Benz, W., Bowers, R. L., Cameron, A. G. W., & Press, W. H. . 1990, ApJ, 348, 647

Bertelli Motta, C., Clark, P. C., Glover, S. C. O., Klessen, R. S., & Pasquali, A. 2016, MNRAS, 462, 4171, 1608.01306

Binney, J., & Tremaine, S. 1987, Galactic dynamics

——. 2008, Galactic Dynamics: Second Edition (Princeton University Press)

Bisbas, T. G., Tanaka, K. E. I., Tan, J. C., Wu, B., & Nakamura, F. 2017, ApJ, 850, 23, 1706.07006

Blitz, L., & Shu, F. H. 1980, ApJ, 238, 148

Bolatto, A. D., Wolfire, M., & Leroy, A. K. 2013, ARA& A, 51, 207, 1301.3498

Bonnell, I. A., Bate, M. R., & Vine, S. G. 2003, MNRAS, 343, 413, astro-ph/0305082

Bonnell, I. A., Dobbs, C. L., Robitaille, T. P., & Pringle, J. E. 2006, MNRAS, 365, 37, astro-ph/0509809

Bonnell, I. A., Dobbs, C. L., & Smith, R. J. 2013, MNRAS, 430, 1790, 1301.1041

Bonnell, I. A., Smith, R. J., Clark, P. C., & Bate, M. R. 2011, MNRAS, 410, 2339, 1009.1152

Brand, J., & Blitz, L. 1993, A& A, 275, 67

Bresolin, F. 1996, in Astronomical Society of the Pacific Conference Series, Vol. 98, From Stars to Galaxies: the Impact of Stellar Physics on Galaxy Evolution, ed. C. Leitherer, U. Fritze-von-Alvensleben, & J. Huchra, 394

Caldwell, J. A. R., & Ostriker, J. P. 1981, ApJ, 251, 61

Churchwell, E. et al. 2009, PASP, 121, 213

Cignoni, M. et al. 2015, ApJ, 811, 76, 1505.04799

Clark, P. C., & Bonnell, I. A. 2006, MNRAS, 368, 1787, astro-ph/0603578

Clark, P. C., Bonnell, I. A., Zinnecker, H., & Bate, M. R. 2005, MNRAS, 359, 809, astro-ph/0503141

Clark, P. C., Glover, S. C. O., & Klessen, R. S. 2012a, MNRAS, 420, 745, 1109.3861

Clark, P. C., Glover, S. C. O., Klessen, R. S., & Bonnell, I. A. 2012b, MNRAS, 424, 2599, 1204.5570

Clemens, D. P. 1985, ApJ, 295, 422

Cox, D. P., & Gómez, G. C. 2002, ApJS, 142, 261, astro-ph/0207635

Crutcher, R. M. 2012, ARA& A, 50, 29

Crutcher, R. M., Wandelt, B., Heiles, C., Falgarone, E., & Troland, T. H. 2010, ApJ, 725, 466

Dale, J. E. 2017, MNRAS, 467, 1067, 1701.03653

Dale, J. E., & Bonnell, I. A. 2008, MNRAS, 391, 2, 0808.1510

——. 2012, MNRAS, 422, 1352, 1202.1417

Dale, J. E., Bonnell, I. A., Clarke, C. J., & Bate, M. R. 2005, MNRAS, 358, 291, astro-ph/0501160

Dale, J. E., Ercolano, B., & Bonnell, I. A. 2012, MNRAS, 424, 377, 1205.0360

——. 2015, MNRAS, 451, 987, 1504.05896

Dale, J. E., Ercolano, B., & Clarke, C. J. 2007, MNRAS, 382, 1759, 0705.3396

Dale, J. E., Ngoumou, J., Ercolano, B., & Bonnell, I. A. 2014, MNRAS, 442, 694, 1404.6102

Dame, T. M. 2013, in American Astronomical Society Meeting Abstracts, Vol. 222, American Astronomical Society Meeting Abstracts, 400.01

Dame, T. M., & Thaddeus, P. 2011, ApJ Letters, 734, L24, 1105.2523

Dobbs, C., & Baba, J. 2014, PASA, 31, e035, 1407.5062

Dobbs, C. L., & Bonnell, I. A. 2007, MNRAS, 374, 1115, astro-ph/0610720

Dobbs, C. L., Bonnell, I. A., & Pringle, J. E. 2006, MNRAS, 371, 1663, astro-ph/0602103

Dobbs, C. L., Glover, S. C. O., Clark, P. C., & Klessen, R. S. 2008, MNRAS, 389, 1097, 0806.4312

Dobbs, C. L., & Pringle, J. E. 2013, MNRAS, 432, 653, 1303.4995

Dobbs, C. L., Pringle, J. E., & Burkert, A. 2012, MNRAS, 425, 2157, 1206.4904

Dobbs, C. L., Pringle, J. E., & Duarte-Cabral, A. 2015, MNRAS, 446, 3608, 1411.0840

Dubois, Y., & Teyssier, R. 2008, A& A, 477, 79, 0707.3376

Elmegreen, B. G. 1979, ApJ, 232, 729

Elmegreen, B. G. 2011, in EAS Publications Series, Vol. 51, EAS Publications Series, ed. C. Charbonnel & T. Montmerle, 45–58, 1101.3112

Elmegreen, B. G., & Lada, C. J. 1977, ApJ, 214, 725

Evrard, A. E. 1988, MNRAS, 235, 911

Falceta-Gonçalves, D., Bonnell, I., Kowal, G., Lépine, J. R. D., & Braga, C. A. S. 2015, MNRAS, 446, 973, 1410.2774

Federrath, C. 2016, MNRAS, 457, 375, 1510.05654

Fernández, D., Figueras, F., & Torra, J. 2008, A& A, 480, 735, 0801.0605

Fűrész, G., Hartmann, L. W., Megeath, S. T., Szentgyorgyi, A. H., & Hamden, E. T. 2008, ApJ, 676, 1109, 0711.0391

Field, G. B., Goldsmith, D. W., & Habing, H. J. 1969, ApJ Letters, 155, L149

Forgan, D., Rice, K., Stamatellos, D., & Whitworth, A. 2009, MNRAS, 394, 882, 0812.0304

Fresneau, A., Vaughan, A. E., & Argyle, R. W. 2005, AJ, 130, 2701

Gatto, A. et al. 2017, MNRAS, 466, 1903, 1606.05346

Getman, K. V., Feigelson, E. D., & Kuhn, M. A. 2014, ApJ, 787, 109, 1403.2742

Gieles, M., & Portegies Zwart, S. F. 2011, MNRAS, 410, L6, 1010.1720

Gingold, R. A., & Monaghan, J. J. 1977, MNRAS, 181, 375

Girichidis, P. et al. 2016, MNRAS, 456, 3432, 1508.06646

Glover, S. C. O., & Mac Low, M.-M. 2007a, ApJS, 169, 239, astro-ph/0605120

——. 2007b, ApJ, 659, 1317, astro-ph/0605121

Gómez, G. C., & Vázquez-Semadeni, E. 2014, ApJ, 791, 124, 1308.6298

Greene, T. P., & Meyer, M. R. 1995, ApJ, 450, 233

Gressel, O., Elstner, D., Ziegler, U., & Rüdiger, G. 2008, A& A, 486, L35, 0805.2616

Gutermuth, R. A., Megeath, S. T., Myers, P. C., Allen, L. E., Pipher, J. L., & Fazio, G. G. 2009, ApJS, 184, 18, 0906.0201

Hacar, A., Alves, J., Forbrich, J., Meingast, S., Kubiak, K., & Großschedl, J. 2016, A& A, 589, A80, 1602.01854

Hacar, A., Tafalla, M., & Alves, J. 2017, ArXiv e-prints, 1703.07029

Hartigan, J. A. 1975, John Wiley. New York

Heiles, C., Goodman, A. A., McKee, C. F., & Zweibel, E. G. 1993, in Protostars and Planets III, ed. E. H. Levy & J. I. Lunine, 279–326

Heitsch, F., Slyz, A. D., Devriendt, J. E. G., Hartmann, L. W., & Burkert, A. 2006, ApJ, 648, 1052, astro-ph/0605435

Heyer, M., Krawczyk, C., Duval, J., & Jackson, J. M. 2009, ApJ, 699, 1092, 0809.1397

Hill, A. S., Joung, M. R., Mac Low, M.-M., Benjamin, R. A., Haffner, L. M., Klingenberg, C., & Waagan, K. 2012, ApJ, 750, 104, 1202.0552

Hiltner, W. A. 1949, Science, 109, 165

Jain, A. K., Murty, M. N., & Flynn, P. J. 1999, ACM Computing Surveys, 31, 264

Kalberla, P. M. W., & Kerp, J. 2009, ARA& A, 47, 27

Kamaya, H., & Nishi, R. 2000, ApJ, 543, 257

Kirk, H., Klassen, M., Pudritz, R., & Pillsworth, S. 2015, ApJ, 802, 75, 1501.05999

Koepferl, C. M., Robitaille, T. P., & Dale, J. E. 2016a, ArXiv e-prints, 1606.08435

——. 2016b, ArXiv e-prints, 1606.08845

Koepferl, C. M., Robitaille, T. P., Dale, J. E., & Biscani, F. 2016c, ArXiv e-prints, 1603.02270

Koyama, H., & Inutsuka, S.-I. 2000, ApJ, 532, 980, astro-ph/9912509

Koyama, H., & Inutsuka, S.-i. 2002, ApJ Letters, 564, L97, astro-ph/0112420

Kraus, A. L., & Hillenbrand, L. A. 2008, ApJ Letters, 686, L111, 0809.0893

Krumholz, M. R., & Bonnell, I. A. 2007, ArXiv e-prints, 0712.0828

Krumholz, M. R., Klein, R. I., & McKee, C. F. 2011, ApJ, 740, 74, 1104.2038

Kuhn, M. A. et al. 2014, ApJ, 787, 107, 1403.4252

Kuhn, M. A., Feigelson, E. D., Getman, K. V., Sills, A., Bate, M. R., & Borissova, J. 2015a, ApJ, 812, 131, 1507.05653

Kuhn, M. A., Getman, K. V., & Feigelson, E. D. 2015b, ApJ, 802, 60, 1501.05300

Lada, C. J., & Lada, E. A. 2003, ARA& A, 41, 57, astro-ph/0301540

Larson, R. B. 1981, MNRAS, 194, 809

Lewis, B. T., & Bate, M. R. 2017, MNRAS, 467, 3324, 1701.08741

Li, P. S., McKee, C. F., & Klein, R. I. 2015, MNRAS, 452, 2500, 1506.08228

Lin, C. C., & Shu, F. H. 1964, ApJ, 140, 646

Louvet, F. et al. 2014, A& A, 570, A15, 1404.4843

Lucy, L. B. 1977, AJ, 82, 1013

MacLachlan, J. M., Bonnell, I. A., Wood, K., & Dale, J. E. 2015, A& A, 573, A112, 1412.6918

Magnier, E. A. et al. 1993, A& A, 278, 36

Majewski, S. R. 2008, in IAU Symposium, Vol. 248, A Giant Step: from Milli- to Micro-arcsecond Astrometry, ed. W. J. Jin, I. Platais, & M. A. C. Perryman, 450–457, 0801.4927

Maloney, P., & Black, J. H. 1988, ApJ, 325, 389

Megeath, S. T. et al. 2016, AJ, 151, 5, 1511.01202

Mel'Nik, A. M., & Efremov, Y. N. 1995, Astronomy Letters, 21, 10

Micic, M., Glover, S. C. O., Banerjee, R., & Klessen, R. S. 2013, MNRAS, 432, 626, 1303.4751

Moeckel, N., Holland, C., Clarke, C. J., & Bonnell, I. A. 2012, MNRAS, 425, 450, 1205.1677

Monaghan, J. J. 1992, ARA& A, 30, 543

——. 2002, MNRAS, 335, 843, astro-ph/0204118

Monaghan, J. J., & Gingold, R. A. 1983, Journal of Computational Physics, 52, 374

Monaghan, J. J., & Lattanzio, J. C. 1985, A& A, 149, 135

Murdin, P. 2001, Encyclopedia of astronomy and astrophysics

Narayanan, D., Krumholz, M. R., Ostriker, E. C., & Hernquist, L. 2012, MNRAS, 421, 3127, 1110.3791

Offner, S. S. R., Klein, R. I., & McKee, C. F. 2008, ApJ, 686, 1174, 0806.1045

Oort, J. H. 1955, in IAU Symposium, Vol. 2, Gas Dynamics of Cosmic Clouds, 147

Ostriker, E. C., & Shetty, R. 2011, ApJ, 731, 41, 1102.1446

Palla, F., & Stahler, S. W. 1999, ApJ, 525, 772

Pascale, E. et al. 2012, in PROCSPIE, Vol. 8444, Ground-based and Airborne Telescopes IV, 844415

Peretto, N. et al. 2013, A& A, 555, A112, 1307.2590

Pfalzner, S., Kirk, H., Sills, A., Urquhart, J. S., Kauffmann, J., Kuhn, M. A., Bhandare, A., & Menten, K. M. 2016, A& A, 586, A68, 1512.00334

Pietrzyński, G., Gieren, W., Fouqué, P., & Pont, F. 2001, A& A, 371, 497, astro-ph/0103374

Pietrzyński, G., Ulaczyk, K., Gieren, W., Bresolin, F., & Kudritzki, R. P. 2005, A& A, 440, 783

Planck Collaboration et al. 2011, A& A, 536, A1, 1101.2022

Porras, A., Christopher, M., Allen, L., Di Francesco, J., Megeath, S. T., & Myers, P. C. 2003, AJ, 126, 1916, astro-ph/0307510

Press, W. H. 1986, in Lecture Notes in Physics, Berlin Springer Verlag, Vol. 267, The Use of Supercomputers in Stellar Dynamics, ed. P. Hut & S. L. W. McMillan, 184

Price, D. J. 2004, PhD thesis, Institute of Astronomy, Madingley Rd, Cambridge, CB2 0HA, UK <EMAIL>dprice@cantab.net</EMAIL>

Price, D. J., Bate, M. R., & Dobbs, C. L. 2009, in Revista Mexicana de Astronomia y Astrofisica, vol. 27, Vol. 36, Revista Mexicana de Astronomia y Astrofisica Conference Series, 128–136, 0804.4647

Price, D. J., & Monaghan, J. J. 2004a, MNRAS, 348, 123, astro-ph/0310789

——. 2004b, MNRAS, 348, 139, astro-ph/0310790

Rathborne, J. M. et al. 2015, ApJ, 802, 125, 1501.07368

Reid, M. J. et al. 2014, ApJ, 783, 130, 1401.5377

Russeil, D., Zavagno, A., Mège, P., Poulin, Y., Molinari, S., & Cambresy, L. 2017, A& A, 601, L5

Saral, G., Hora, J. L., Willis, S. E., Koenig, X. P., Gutermuth, R. A., & Saygac, A. T. 2015, ApJ, 813, 25, 1509.05749

Shetty, R., Vogel, S. N., Ostriker, E. C., & Teuben, P. J. 2007, ApJ, 665, 1138, 0705.3240

Shu, F. H., Adams, F. C., & Lizano, S. 1987, ARA& A, 25, 23

Simonson, III, S. C. 1976, A& A, 46, 261

Sitnik, T. G. 2003, Astronomy Letters, 29, 311

Smith, R. J., Glover, S. C. O., & Klessen, R. S. 2014, MNRAS, 445, 2900, 1407.6716

Smith, R. J., Longmore, S., & Bonnell, I. 2009, MNRAS, 400, 1775, 0908.3910

Sofue, Y. 2012, PASJ, 64, 75, 1110.4431

Sofue, Y., Honma, M., & Omodaka, T. 2009, PASJ, 61, 227, 0811.0859

Soler, J. D. et al. 2016, A& A, 596, A93, 1605.09371

Soler, J. D., & Hennebelle, P. 2017, ArXiv e-prints, 1705.00477

Soler, J. D., Hennebelle, P., Martin, P. G., Miville-Deschênes, M.-A., Netterfield, C. B., & Fissel, L. M. 2013, ApJ, 774, 128, 1303.1830

Soni, N., & Ganatra, A. 2012, International Journal of Advanced Research in Computer Science and Software Engineering, 2, 63

Stahler, S. W., & Palla, F. 2005, The Formation of Stars, 865

Tilanus, R. P. J., & Allen, R. J. 1990, in NASA Conference Publication, Vol. 3084, NASA Conference Publication, ed. D. J. Hollenbach & H. A. Thronson, Jr.

Tout, C. A., Livio, M., & Bonnell, I. A. 1999, MNRAS, 310, 360, astro-ph/9907439

Urquhart, J. S., Figura, C. C., Moore, T. J. T., Hoare, M. G., Lumsden, S. L., Mottram, J. C., Thompson, M. A., & Oudmaijer, R. D. 2014, MNRAS, 437, 1791, 1310.4758

Vázquez-Semadeni, E., Gómez, G. C., Jappsen, A. K., Ballesteros-Paredes, J., González, R. F., & Klessen, R. S. 2007, ApJ, 657, 870, astro-ph/0608375

Vázquez-Semadeni, E., González-Samaniego, A., & Colín, P. 2017, MNRAS, 467, 1313, 1611.00088

Williams, J. P., Blitz, L., & McKee, C. F. 2000, Protostars and Planets IV, 97, astro-ph/9902246

Wolfire, M. G., Hollenbach, D., McKee, C. F., Tielens, A. G. G. M., & Bakes, E. L. O. 1995, ApJ, 443, 152

Yoshida, A., Kitamura, Y., Shimajiri, Y., & Kawabe, R. 2010, ApJ, 718, 1019

Zafar, M. H., & Ilyas, M. 2015, International Journal of Database Theory and Application, 8, 11

Zasov, A., & Kasparova, A. 2014, APSS, 353, 595, 1407.3356

Zhao, Y., & Karypis, G. 2005, Molecular Biotechnology, 31, 55